

DEVELOPMENT OF NON-INVASIVE RESPONSIVE AGENTS FOR
MAGNETIC RESONANCE IMAGING

by

Namini Nirodha Paranawithana



APPROVED BY SUPERVISORY COMMITTEE:

A. Dean Sherry, Chair

Garry E. Kiefer

John W. Sibert

Steven O. Nielsen

Gabriele Meloni

Copyright 2019

Namini Nirodha Paranawithana

All Rights Reserved

To
my mother, Chandra Kumari Kaluwawe,
for inspiring me with her invincible courage, and diligent personality to reach these goals
but most of all, for teaching me that a good scientist is the
one who preserves humanity above all,
and
my father, Russel Paranawithana,
for convincing me education is wealth, integrity is strength for respected human beings.
above all, for your collective nature, perseverance and unconditional love.

DEVELOPMENT OF NON-INVASIVE RESPONSIVE AGENTS
FOR MAGNETIC RESONANCE IMAGING

by

NAMINI NIRODHA PARANAWITHANA, MS

DISSERTATION

Presented to the Faculty of
The University of Texas at Dallas
in Partial Fulfillment
of the Requirements
for the Degree of

DOCTOR OF PHILOSOPHY IN
CHEMISTRY

THE UNIVERSITY OF TEXAS AT DALLAS

May 2019

ACKNOWLEDGMENTS

I would like to express my deepest gratitude to my advisor, Dr. A. Dean Sherry, for his guidance, continuous support, motivation, enthusiasm, and immense knowledge. His lifelong passion for science was an inspiration to all of us. Without his support and encouragement this study would not have been completed. I would like to extend my gratitude to my dissertation committee, Dr. John Sibert and Dr. Steven Nielsen, for their valuable suggestions and advice during my research. I am very grateful to Dr. Gabriele Meloni and Dr. Garry E. Kiefer for all their expertise in research and their invaluable guidance. I would also like to thank Dr. Andre Martins for his valuable support and encouragement throughout my research and I am thankful to Dr. Piyu Zhao for sharing his NMR expertise and for all the support given to me in the lab. I would like to thank Dr. Veronica Jordan for helping me with imaging experiments and helpful insights regarding my research work. Special thanks to Dr. Paul Jurek at Macrocyclics for helping me with the potentiometric studies. Special thanks to Dr. Sara Charyil, Dr. James Ratnayake, Dr. Zoltan Kovacs, Dr. Khaled Naser at The University of Texas at Southwestern Medical Center as well as Dr. Hien Q. Nguyen and Dr. Alexios Papadimitrators at UTD for their assistance in all the laboratory experiments. I thank all the faculty members and staff members in the Department of Chemistry for always being ready to extend a helping hand. My sincere thanks to our group's program assistant, Deb McGill, for always being there for me when I needed help and for her kindness and compassion during difficult times.

Finally, I would like to extend my sincerest thanks to my parents for their unconditional support and encouragement throughout this journey. Without their hard work, patience and perseverance, I couldn't have reached this milestone. Thank you to all other extended family who believed in

me, that kept me on my toes and fueled my enthusiasm in science. Thank you for being there for me always and in return only expecting to hear my success story. I would like to take this opportunity to thank all the lab members at UT Dallas and UT Southwestern for all their help and especially for making an enjoyable work environment. I would like to thank all my friends for their constant friendship, kindness, support and most of all for being my family away from home.

December 2018

DEVELOPMENT OF NON-INVASIVE RESPONSIVE AGENTS FOR MAGNETIC RESONANCE IMAGING

Namini Nirodha Paranawithana, PhD
The University of Texas at Dallas, 2019

Supervising Professor: A. Dean Sherry

Molecular imaging involves visualizing bioactive molecules or biological parameters *in vivo* at the molecular level in a live organism. In Magnetic Resonance Imaging (MRI), inorganic complexes with paramagnetic ions, are commonly used to enhance the intrinsic image contrast of the soft tissues—contrast agents (CAs). Gd-based MR probes paved their way towards medical imaging and clinical application. CAs could change their r_1 relaxivity in response to the local environment are known as “smart” probes. This dissertation reports the development and optimization of “smart” Magnetic Resonance Imaging agents to detect *in-vivo* copper ion levels and extracellular pH—two important extracellular biomarkers.

Copper is the third most abundant transition metal in the body and a required dietary nutrient. Although the relationship between copper dynamics and its physiological or pathological roles have been extensively studied, information about its extracellular behavior in biologically relevant conditions remains insufficiently understood due to the lack of real-time non-invasive copper detecting techniques. Chapter 2 presents the design and organic synthesis of novel copper-responsive MR sensors. These sensors included a copper-selective bis(benzoic acid)methylamine

recognition motif (GdL). We studied the physicochemical properties of the newly developed agents and devised a comprehensive study to understand the possible coordination of GdL1 with copper and HAS. GdL1 shows high selectivity to copper ions and exhibits an increase in relaxivity by 47% upon binding to 1 equivalent of Cu^{2+} . Interestingly, when fully bound to Cu^{2+} sensor presents a 270% increase in relaxivity(r_1) in the presence of a physiological concentration of human serum albumin. We performed *in vivo* imaging with healthy mice and visualized extracellular exchangeable copper in the liver for the first-time by MRI. These results will pave the way for unique opportunities to explore the role of copper in the progression of many neurological disorders, including Wilson's disease.

pH is a fundamental physiological parameter tightly regulated by endogenous buffers at the intracellular and extracellular level. Disruption of regulation of pH is associated with pathological conditions such as cancer, acidosis and kidney disease. GdDOTA-4AmP is a T_1 agent for MRI that has been applied non-invasively to image *in-vivo* tissue. This approach was limited by the use of a dual-contrast agent strategy and with lower elimination time of the agents *in vivo* due to possible deposition in the bones. In Chapter 3, we describe a set of novel Gd-based T_1 agents that present optimized pH-responsive MRI properties to GdDOTA-1AmP, GdDOTA-2AmP, and GdDOTA-3AmP. The GdDOTA-1AmP, exhibits a surprisingly large increase in r_1 relaxivity from 3.0 to 6.3 $\text{mM}^{-1}\text{s}^{-1}$ as the pH is reduced from 9 to 2.5. The origin of this unique pH sensitivity was traced to protonation of the single phosphonate side-chain, which, upon protonation, catalyzes exchange of protons between a Gd-bound water molecule and bulk water. T_1 -weighted images of phantoms showed that MR image intensity increased 12-fold between a physiological pH of 7.4

and pH 6. This demonstrates it is possible to design simple, small molecule MRI contrast agents that respond to pH using simple acid-base principles.

TABLE OF CONTENTS

| | |
|---|------|
| ACKNOWLEDGMENTS | v |
| ABSTRACT | vii |
| LIST OF FIGURES..... | xi |
| LIST OF SCHEMES..... | xvi |
| LIST OF TABLES..... | xvii |
| CHAPTER 1 INTRODUCTION..... | 1 |
| 1.1 Magnetic Resonance Imaging..... | 1 |
| 1.2 Molecular Imaging Probes in MRI..... | 5 |
| 1.3 Gadolinium-Based Responsive Probes..... | 5 |
| 1.4 Objective of this study | 9 |
| 1.5 References..... | 10 |
| CHAPTER 2 A RESPONSIVE MRI CONTRAST AGENT FOR DETECTION OF EXCESS COPPER(II) IN THE LIVER IN VIVO..... | 14 |
| 2.1 Abstract..... | 15 |
| 2.2 Introduction..... | 15 |
| 2.3 Experimental section..... | 18 |
| 2.4 Results and Discussion..... | 38 |
| 2.5 Conclusion..... | 66 |
| 2.6 References..... | 68 |
| CHAPTER 3 A NOVEL PH-SENSITIVE MRI CONTRAST AGENT BASED UPON GDDOTA-MONOAMIDE METHYLENE PHOSPHONATE..... | 74 |
| 3.1 Abstract..... | 75 |
| 3.2 Introduction..... | 75 |
| 3.3 Experimental section..... | 77 |
| 3.4 Results and Discussion..... | 95 |
| 3.5 Conclusions..... | 104 |
| 3.6 References..... | 106 |

| | |
|---------------------------|-----|
| FUTURE PRESPECTIVES | 112 |
| BIOGRAPHICAL SKETCH..... | 114 |
| CURRICULUM VITAE | |

LIST OF FIGURES

| | |
|---|----|
| 1.1 Factors that contribute to r_1 | 3 |
| 1.2 Schematic representation of two clinically-approved MRI contrast agents..... | 4 |
| 1.3 Selected Gd^{3+} -based responsive agents | 8 |
| 2.1 Gadolinium-DO3A based copper responsive (GdL) agents..... | 18 |
| 2.2 LC-MS of GdL1 Complex..... | 25 |
| 2.3 1H NMR spectrum of EuL1 showing square antiprism (SAP) and twisted square antiprism (TSAP) structure in an approximate 4:1 ratio (Top) 2D-COSY spectrum of 80 mM YbL1. (bottom) | 26 |
| 2.4 2D COSY spectrum of 80mM YbL1..... | 26 |
| 2.5 Cyclic voltammograms of GdL1 acquired in 0.1 M MOPS buffer (pH 7.4) at 25 °C. All potentials are referenced to the standard hydrogen electrode (SHE)..... | 33 |
| 2.6 ^{113}Cd NMR spectra of (A) 2mM HSA and 6mM $^{113}CdCl_2$ (B) 2mM HSA, 2mM Cu^{2+} , 4mM LaL1 and 6mM $^{113}CdCl_2$ (C) 2mM HAS, 4mM Cu^{2+} , 4mM LaL1 and 6mM $^{113}CdCl_2$ at 59.92 MHz, pD =7.4 in MOPS buffer..... | 35 |
| 2.7 The relaxivity (r_1) of GdL1 in the presence of various $M^{2+} \pm$ HSA. The white bars reflect r_1 after addition of 0.5 mM Mg^{2+} , Ca^{2+} , Fe^{3+} , Zn^{2+} or Cu^{2+} to 0.5mM solution of GdL1. The black bars reflect r_1 after subsequent addition of 0.6mM HSA to the GdL1- M^{2+} solutions. The r_1 values were determined in 0.1M MOPS buffer (pH 7.4) at 37°C and 20MHz..... | 40 |
| 2.8 Relaxivity response of 0.5 mM GdL1 to various metal ions in 0.1M MOPS buffer (pH 7.4) at 20 MHz and 37°C..... | 40 |
| 2.9 Job's plot for GdL1 and Cu^{2+} | 41 |
| 2.10 The r_1 relaxivity of GdL1-3 as a function of added Cu^{2+} ions. The concentration of GdL1-3 was 0.5 mM in 0.1M MOPS buffer (pH 7.4). The data were collected at 20 MHz and 37°C..... | 41 |
| 2.11 Experimental and fitted titration curves for change in fluorescence intensity upon titration with Cu^{2+} at 25°C for GdL1, GdL2, and GdL3..... | 43 |

| | |
|---|----|
| 2.12 The r_1 relaxivity of 0.5 mM GdL1 after addition of Mg^{2+} , Ca^{2+} , Fe^{3+} , Zn^{2+} or Cu^{2+} in 0.1M MOPS buffer (pH 7.4) and 600 μ M HSA at 37°C and 20MHz..... | 44 |
| 2.13 Relaxivity response of 0.5 mM GdL1-3 to 1 equivalents of Zn^{2+} and Cu^{2+} in 0.1M MOPS buffer (pH 7.4) with 600 μ M HSA at 37°C at a proton Larmor frequency of 20MHz..... | 45 |
| 2.14 Proton relaxation enhancement of GdL-Cu ²⁺ complexes with increasing concentration of HSA..... | 46 |
| 2.15 Chromatogram for of size exclusion chromatography..... | 47 |
| 2.16 Competition binding curves are showing that dansylglycine (drug site 2) (top left) is displaced by GdL1 while warfarin (drug site 1) (top right) is not. Bottom curves represent the competition titration with CuCl ₂ instead of GdL1..... | 49 |
| 2.17 Temperature dependence of the reduced longitudinal and transverse ¹⁷ O relaxation rates and reduced chemical shifts of the GdL1 (25.4 mM) and GdL2 (25.1 mM) in aqueous solution B ₀ = 9.4T..... | 50 |
| 2.18 Relaxivity measurements of 1.5 mM GdL1 and 4.5 mM Cu ²⁺ in 30 mM Phosphate buffer in 310 K at 20 MHz..... | 52 |
| 2.19 ¹ H NMR titration spectra of 20 mM LaL1 in the presence of various concentrations of Cu ²⁺ at 37°C in D ₂ O..... | 53 |
| 2.20 X-Band EPR Spectra of 250 μ M Cu ²⁺ with 250 μ M LaL1 in 250 μ M HSA in 10mM MOPS buffer at pH 7.2 (2,500–3,500 G, 9.3 GHz, 30K)..... | 54 |
| 2.21 XANES spectra for GdL1 in the presence of Cu ²⁺ and HSA..... | 56 |
| 2.22 EXAFS experimental oscillations (black lines) and corresponding calculated best fits (red lines) and corresponding EXAFS Fourier transforms determined for GdL1-Cu(II) (A), HAS-Cu(II) (B) and GdL1-Cu(II)-HAS (C)..... | 60 |
| 2.23 MM ⁺ minimized structures of (A) Domain structure of albumin (PDB ID code 1AO6): domain I and II are colored green (residues 1–373), domain III in yellow (residues 380–571), long chain fatty acid sites (FA), Sudlow’s drug binding sites, Cu ²⁺ binding NTS site and zinc binding site A (MBS/Site A) are also shown. (B)GdL1-Cu ²⁺ complex (C) HSA-Cu ²⁺ complex (CCDC-809109) ⁵² (D) HSA-Cu ²⁺ - GdL1 distorted square pyramidal complex (E) HSA-Cu ²⁺ - GdL1 distorted octahedral complex consistent with all NMR, XAS and EXAFS data. | 61 |
| 2.24 T ₁ - Weighted phantom MR images. Repetition time (TR) = 2500.0 ms; echo time (TE) = 10.0 ms; Data Matrix = 256 x 256. Images and T ₁ values were obtained at 400 MHz (9.4T)..... | 62 |

| | |
|--|-----|
| 2.25 (A) <i>In vivo</i> MRI images of wild type mouse liver (n=3) pre- and post-injection of GdL ₁ (0.1mmol/kg) without (top) or with (bottom) pretreatment with ATN-224 (5mg/kg in 50ul). All images were obtained at 4.7 T. (B) The average MRI signal intensity of mouse liver 6 min after injection of GdL ₁ in control mice <i>versus</i> mice pretreated with ATN-224. The columns on the right show the same measurements for animal injected with Gadavist™ rather than GdL ₁ . The data were compared using a two-tailed student t-test. *p < 0.05 (n=3); error bars reflect ± SD. (C) Total Cu and Gd (μg/g tissue) in various tissues collected from the mice with or without pretreatment of ATN-224, 6 min after the injection of GdL ₁ . Tissue copper levels relative to tissue wet weight were determined by ICP-MS. The data were compared using a two-tailed student t-test. *p < 0.05 (n=3); error bars reflect ± SD..... | 64 |
| 3.1 Gadolinium-amidephosphonate based pH responsive agents..... | 75 |
| 3.2 HPLC Profile of DOTA-1AmP..... | 87 |
| 3.3 LC-MS Profile of DOTA-3AMP..... | 88 |
| 3.4 HPLC Profile of Gd-DOTA-1AmP..... | 89 |
| 3.5 LC-MS Profile of Gd-DOTA-1AmP..... | 90 |
| 3.6 LC-MS Profile of Gd-DOTA-3AmP..... | 92 |
| 3.7 Fitted relaxivity curve as a sigmoidal function (Solid line) and data Points (Triangles)..... | 92 |
| 3.8 Effect of solution pH on the relaxivity of GdDOTA-1AmP (squares), GdDOTA- 2AmP (circles), GdDOTA- 3AmP (triangles) and GdDOTA- 4AmP (pentagons) recorded at 37 °C and 20 MHz with 0.5 mM of agent..... | 97 |
| 3.9 Effect of solution pH on the relaxivity of Gd-DOTA-1AMP (Squares) and Gd-DOTA-1AMP in the presence of 135 mM NaCl, 5 mM KCl, and 2.5 mM CaCl ₂ (Circles). Measurements were recorded at 37 °C and 20 MHz with 0.5 mM Gd-DOTA-1AMP..... | 98 |
| 3.10 ¹ H NMR spectrum of EuDOTA-1AmP (80 mM) showing square antiprism (SAP) and twisted square antiprism (TSAP) structure at pD ~ 6.5 in D ₂ O at 400 MHz..... | 99 |
| 3.11 Decay curves of luminescence of 20 mM Eu-DOTA-1AMP in H ₂ O (left) and D ₂ O (right). λ _{ex} = 394 nm, λ _{em} = 595 nm..... | 100 |
| 3.12 Longitudinal relaxivity pH profile of Gd-DOTA-1AMP (37 °C, 20 MHz, 0.5 mM) (Dashed line) laid over the speciation diagram of Gd-DOTA-1AMP..... | 101 |

| | |
|---|-----|
| 3.13 Schematic representation prototropic effect described, viewed down the Gd-OH ₂ axis, of how the phosphonates in GdLH ⁻ transfer protons between the coordinated water molecule and the bulk solvent..... | 101 |
| 3.14 T ₁ - Weighted phantom MR images. Images and T ₁ values were obtained at 400 MHz (9.4T) | 102 |

LIST OF SCHEMES

| | |
|---------------------------------|----|
| 2.1 Synthesis of L_1 | 20 |
| 2.2 Synthesis of L_1 | 21 |
| 2.3 Synthesis of L_2 | 23 |
| 3.1 Synthesis of DOTA-1AmP..... | 80 |
| 3.2 Synthesis of AmP-Br..... | 82 |
| 3.3 Synthesis of DOTA-2AmP..... | 83 |
| 3.4 Synthesis of DOTA-3AmP..... | 84 |

LIST OF TABLES

| | |
|--|-----|
| 2.1 Relaxivity and K_d values for GdL1-3 in 0.1M MOPS buffer (pH 7.4) at 37°C..... | 46 |
| 2.2 Best-fit parameters Relaxivity and K_d value for GdL1-3 in 0.1 M MOPS buffer (pH 7.4) at 37°C..... | 42 |
| 2.3 Lanthanum metal ion concentration in high-molecular-weight fraction and low-molecular-weight fraction..... | 48 |
| 2.4 Best-fit parameters obtained for GdL1 and GdL2 from analysis of ^{17}O NMR data..... | 51 |
| 2.5 Structural and coordination parameters obtained from fitting Cu K-edge EXAFS..... | 58 |
| 3.1 Measured q value at different pH at 25 °C..... | 100 |
| 3.2 Best-fit parameters obtained for Gd-DOTA-1AmP from analysis of ^{17}O NMR data..... | 101 |
| 3.3 Protonation constant of Gd-DOTA-1AmP in 1.0M KCl..... | 102 |
| 3.4 Stability constant and protonation constant of Gd-DOTA-1AmP in 1.0M KCl..... | 103 |

CHAPTER 1

INTRODUCTION

1.1 Magnetic Resonance Imaging

Molecular imaging can be defined as visualization of biological processes and *in-vivo* characterization at the molecular level.¹ Various molecular imaging techniques are currently being used clinically for analyzing biological processes from the cellular level to whole organisms. They include optical imaging (OI), positron emission tomography (PET), single photon emission computed tomography (SPECT), and magnetic resonance imaging (MRI). MRI is powerful non-invasive technique that captures three dimensional analytical images mostly of tissue water and fat. MRI was discovered in 1970² and is now widely used for disease detection, diagnosis and treatment monitoring.³ MRI tissue contrast originates largely from differences in proton concentration, relaxation behavior, and tissue perfusion/diffusion characteristics. Hence, image contrast reports on the physical behavior of water and fat molecules in each tissue. MRI can also be used to image other NMR-active nuclei such as ^{19}F , ^{13}C , ^{31}P and ^{129}Xe .⁴⁻⁶

A typical MRI signal is dominated by tissue water and is highly dependent on the T_1 and T_2 relaxation characteristics of water. Contrast agents are widely used in MRI to amplify differences in tissue contrast. Paramagnetic contrast agents derived from Mn^{2+} , Mn^{3+} , Fe^{3+} , Cu^{2+} or Gd^{3+} efficiently alter the relaxation characteristics of water protons. Among these, Gd^{3+} has emerged as the most widely used paramagnetic ion for altering contrast because it has 7 unpaired electrons ($S = 7/2$), fast water exchange, and a relatively long electron spin relaxation time.³ The efficiency of contrast enhancement is given by a parameter called relaxivity (r_1), defined as the longitudinal

paramagnetic relaxation rate observed for a 1 mM aqueous solution of contrast media. r_1 is reported in units of $\text{mM}^{-1}\text{s}^{-1}$ and is field and temperature dependent (Equation 1.1).⁷⁻⁹

$$\frac{1}{T1(\text{obs})} = \frac{1}{T1(\text{d})} + \frac{1}{T1(\text{p})}$$

$$\frac{1}{T1(\text{obs})} = \frac{1}{T1(\text{d})} + r_1[\text{CA}]$$

$$r_1 = r_1^{IS} + r_1^{OS} \quad \textbf{Equation 1.1}$$

$T_{1(\text{obs})}$ is the T_1 of bulk water measured in the presence of a paramagnetic compound. $T_{1\text{d}}$ is the T_1 of water without a paramagnetic compound and $T_{1\text{p}}$ is the paramagnetic contribution. r_1 represents relaxivity of the contrast agent and $[\text{CA}]$ represents the concentration of Gd^{3+} in solution. The relaxivity contains both inner sphere (IS) and outer sphere (OS) terms. The inner sphere term describes the relaxation effect originating from the closest hydrogen nuclei of water molecules interacting directly with the paramagnetic ion. The outer sphere term describes the effect of the interactions between the paramagnetic ion and closely diffusing water molecules without interacting with the complex.⁷⁻⁹

The r_1 relaxivity of a contrast agent is determined by many factors. Figure 1.1 shows the multiple factors affecting the proton relaxivity values of Gd^{3+} -based small-molecules contrast agents. The relationship between variables contributing to the inner sphere are described by the Solomon-

Bloembergen-Morgan equation.¹⁰⁻¹² The number of inner-sphere water molecules (q), the rotational tumbling time of the complex (τ_R), and the residence lifetime of inner-sphere water molecules (τ_m) are the main factors that can affect r_1 . A large number of inner-sphere water molecules and a longer tumbling time (τ_R) both contribute to higher r_1 values. The relationship between τ_m and r_1 is optimal when τ_m is about 10ns. The Freed model describes the contribution of the outer-sphere variables (a and τ_D) on overall relaxivity but this contribution is not as dominant as inner-sphere relaxation.¹³

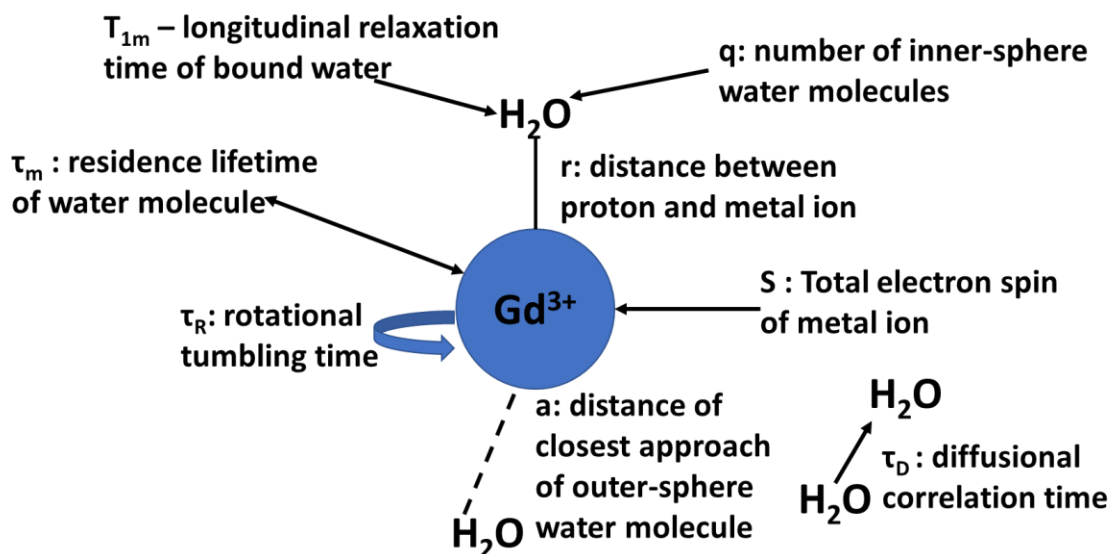


Figure 1.1. Factors that contribute to r_1

Magnevist ($GdDTPA$), an octadentate complex formed by diethylenetriaminepentaacetic acid (DTPA) and the Gd^{3+} ion was the first reported Gd -based contrast agent (Figure 1.2).¹⁴ Generally, Gd^{3+} ions forms complexes with nine inner-sphere coordination sites so, in this case, DTPA has eight donor atoms, five from the carboxylates and three from tertiary amines. The final

coordination site remains available for a water molecule. The coordinated water molecule exchanges with the surrounding bulk water transferring the paramagnetic effect from the Gd(III) ion to the bulk water.¹⁵ Many commercially available MRI CAs (Figure 1.2), including Magnevist have only one bound water molecule. The inner-sphere relaxivity of a Gd-complex is proportional to the hydration number (q). Yet, increase in hydration number could cause the dissociation of gadolinium from the complex, inducing toxicity during in-vivo application.^{16,17} Further, the efficiency of contrast agent can be optimized by manipulating other parameters such as the water exchange rate (k_{ex}) and rotational correlational time (τ_R).

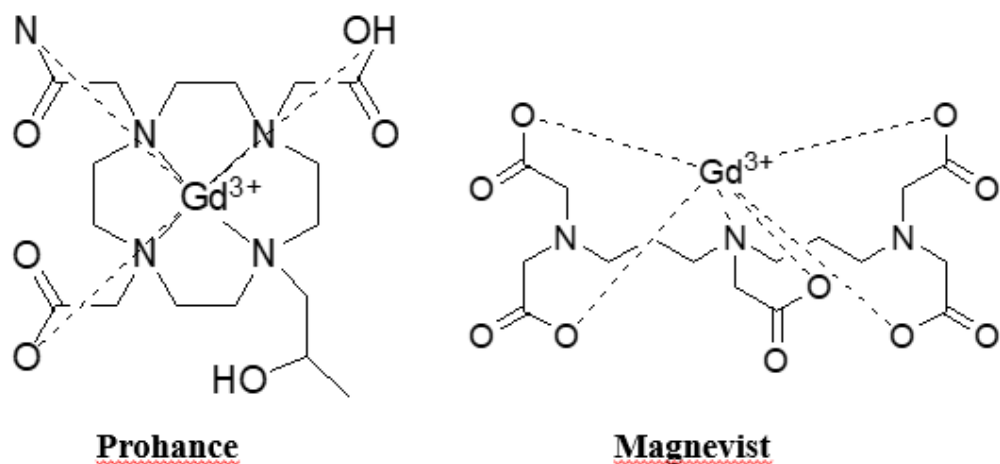


Figure 1.2. Schematic representation of two clinically-approved MRI contrast agents.

1.2. Molecular Imaging Probes in MRI

Magnetic resonance imaging has been used to obtain anatomical and functional images of tissues for long time. But recent applications of MRI focused on imaging information at molecular level by visualizing biochemical and physiological parameters underlying the disease condition. This requires molecular imaging probes that are responsive to a specific biological or physiological parameter. These probes are known as smart, activatable or responsive contrast agents.¹⁸ These smart CAs can increase or decrease the MRI signal intensity in response to a given analyte. The design of responsive probes is primarily based on three systems: gadolinium-based T_1 agents, paramagnetic chemical saturation transfer agents (PARACEST) and T_2 agents. The details of later agents will not be discussed and focus of this introduction will be Gd-based responsive MRI contrast agents.

1.3. Gadolinium-based Responsive Probes

The responsive Gd^{3+} -complexes are designed to report a change in a cellular event by MRI. Various disease conditions including cancer, ischemia, infection and inflammation can alter extracellular pH, pO_2 , the tissue redox state, metal concentrations, enzyme activities and other indices so an ability to visualize these dynamic changes in microenvironment could be helpful in monitoring disease progression or a therapeutic response. The design of such agents must consider all factors that govern the r_1 .¹⁹⁻²² Most smart CAs display a change in hydration number (q) in response to a particular analyte. In addition, some smart CAs use modulation of the exchange rate (k_{ex}) of the water molecules with the surrounding water and rotational correlation time (τ_R) of the agent to optimize the relaxivity.²³ The coupling of CAs to a macromolecule or a protein increases

the rotation correlation time, and this increases the longitudinal relaxivity (r_1) and results in image contrast enhancement or image brightening. This can be done by direct binding to the protein or targeting a receptor that internalizes the sensor into cells.

Tom Meade pioneered the development of the first smart agent, a bio-activatable sensor of β -galactosidase activity.²⁴ This was based on a galacto-pyranose-substituted DOTA structure in which the sugar coordinates to the Gd^{3+} ion and excludes the inner-sphere water molecule. Upon activation the sugar is removed by β -galactosidase and this opens the coordination sphere to a water molecule. Although this results in a small increase in relaxivity during the activation step, the change was too small for *in vivo* applications.²⁵ Since that early study, there have been approaches proposed to amplify this effect and make it useful *in vivo*.^{26,27} Recently, a β -galactopyranose containing Gd^{3+} complex (Gd -(DOTA-FPG) (H_2O)) was reported that can be activated by β -galactosidase (Figure 1.3). The relaxivity values increase significantly by the enzymatic cleavage of the Gd complex in the presence of β -galactosidase and human serum albumin (HSA). The application of this complex *in vivo* reports that the signal intensities of tumors with β -galactosidase gene expression are significantly higher than those tumors without β -galactosidase gene expression.²⁸

Later, many other smart probes have been reported for detection of enzyme activity,²⁹ pH,³⁰ glucose,³¹ lactate,³² pO_2 ³³ and metal ions such as Zn^{2+} ,^{34,35} Cu^{2+} ,³⁶ and Ca^{2+} .³⁷ These probes typically increase the hydration number upon activation (on-state) which results in a positive gain in r_1 in the on-state with near zero r_1 in the off-state ($q=0$). An example of this is given by the

first reported Ca^{2+} responsive agent (GdL) consisting of two DO3A derivatives connected by a BAPTA (1,2,1,2-bis(o-aminophenoxy) ethane-N,N,N,N-tetraacetic acid) moiety (Figure 1.3).³⁷ In the absence of Ca^{2+} , both acetate groups from iminodiacetate coordinate to the Gd^{3+} -ion to yield an r_1 of $3.26 \text{ mM}^{-1}\text{s}^{-1}$. In the presence of one equivalent of Ca^{2+} , the acetate groups in iminodiacetate binds with Ca^{2+} thereby allowing full access of water to the inner-sphere of the Gd^{3+} ion. This results in an increase in r_1 by 77% to $5.76 \text{ mM}^{-1}\text{s}^{-1}$ when bound to calcium. For such agents to work as a Ca^{2+} sensor using MRI for detection, the extracellular Ca^{2+} concentration would need to be in the same range as the agent concentration (millimolar).

GdDOTA-diBPEN, a first-generation Zn^{2+} -responsive MR contrast agent reported by our group,³⁴ has two appended BPEN ligands each having a high affinity for Zn^{2+} ions (Figure 1.3). This agent binds with human serum albumin (HSA) in the presence of Zn^{2+} ions a high relaxivity (r_1) with formation of ternary complex. Further, this agent was applied to detect the release of Zn^{2+} ions from pancreatic β -cells *in vivo* by MRI.³⁸ Next generation of these agents were developed by optimizing the rate of water exchange (k_{ex}) between the single inner-sphere water molecule on the Gd^{3+} ion with bulk solvent.³⁵ These agents reported higher change in relaxivity and applied in *in vivo* studies with mice. They showed an enhancement in pancreas after the agent infused into a mouse for ~ 30 min followed by a bolus of 20% w/v glucose. Recently, we reported that Zn^{2+} ion secretion from β -cells would be detected as high intensity, focal “hot spots” in the pancreas tail only after glucose is given to stimulate insulin and Zn^{2+} secretion.³⁹

Furthermore, our group also reported a pH-sensitive probe, GdDOTA-4AmP with unique pH dependence of relaxivity that has been applied *in vivo* to image tissue pH.⁴⁰ This agent has been discussed in detail in chapter 3.

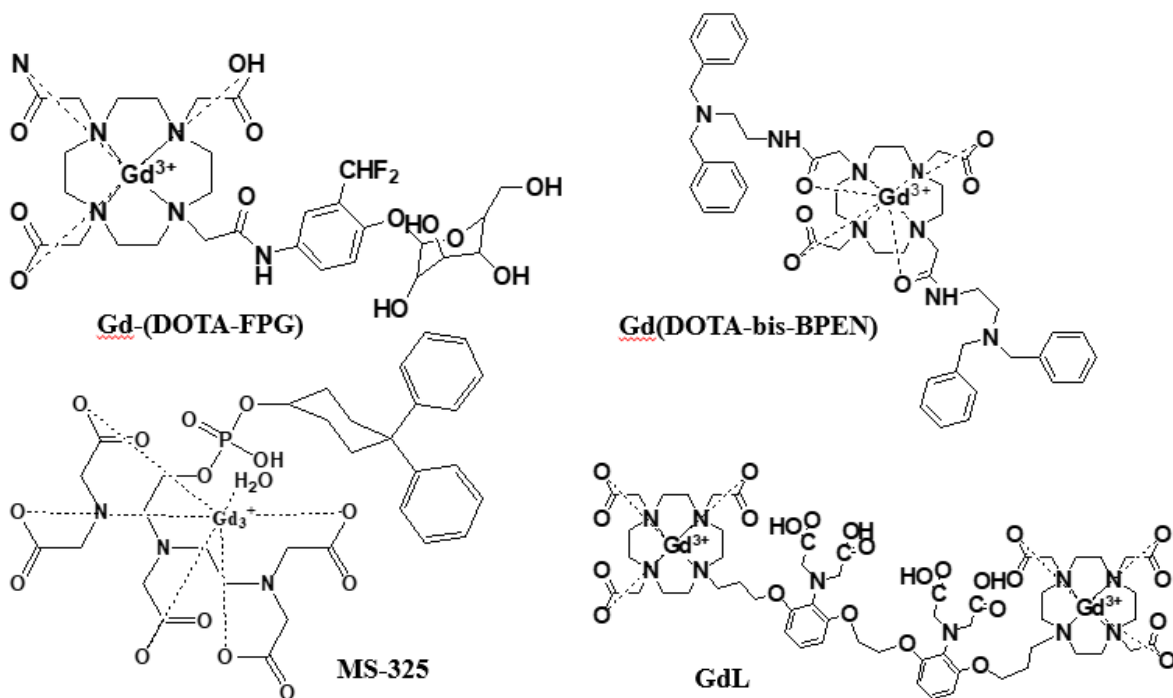


Figure 1.3. Selected Gd³⁺- based responsive agents

The clinically approved serum albumin probe, MS-325 (Ablavar) is an example of a protein targeted probe that was originally designed for imaging blood vessels (Figure 1.3).^{41,42} MS-325 reported reversible binding of Gd³⁺-complexes with serum albumin in plasma increasing the relaxivity.⁴³ Similarly, activatable probes that are based on enzyme activity of myeloperoxidase,⁴⁴ tyrosinase,⁴⁵ blood coagulation factor XII⁴⁶ and thrombin activatable fibrinolysis inhibitor (TAFI)⁴⁷ have been used in molecular MR imaging.

1.4. Objective of the Study

The research reported in this dissertation include two separate projects that describes the development and testing of two different “smart” contrast agents for MRI. In Chapter 2, a comprehensive study of design, synthesis and characterization of a Gd-based Cu^{2+} -responsive agent for detection of extracellular copper in liver is presented. Chapter 3 reports the development of optimized Gd-based pH sensors to detect extracellular pH.

REFERENCES

1. Weissleder, R.; Mahmood, U. Molecular Imaging. *Radiology* **2001**, *219* (2), 316–333.
2. P.C. Lauterbur. Magnetic Resonance. *Nature* **1973**, *242*, 190–191.
3. Caravan, P.; Ellison, J. J.; McMurry, T. J.; Lauffer, R. B. Gadolinium(III) Chelates as MRI Contrast Agents: Structure, Dynamics, and Applications. *Chem. Rev.* **1999**, *99* (9), 2293–2352.
4. Yu, J.; Kodibagkar, V. D.; Cui, W.; Mason, R. P. 19F: A Versatile Reporter for Non-Invasive Physiology and Pharmacology Using Magnetic Resonance. *Curr. Med. Chem.* **2005**, *12* (7), 819–848.
5. Kurhanewicz, J.; Bok, R.; Nelson, S. J.; Vigneron, D. B. Current and Potential Applications of Clinical ¹³C MR Spectroscopy. *J. Nucl. Med. Off. Publ. Soc. Nucl. Med.* **2008**, *49* (3), 341–344.
6. Schröder, L.; Lowery, T. J.; Hilty, C.; Wemmer, D. E.; Pines, A. Molecular Imaging Using a Targeted Magnetic Resonance Hyperpolarized Biosensor. *Science* **2006**, *314* (5798), 446–449.
7. León-Rodríguez, L. M. D.; Martins, A. F.; Pinho, M. C.; Rofsky, N. M.; Sherry, A. D. Basic MR Relaxation Mechanisms and Contrast Agent Design. *J. Magn. Reson. Imaging* *42* (3), 545–565.
8. Viswanathan, S.; Kovacs, Z.; Green, K. N.; Ratnakar, S. J.; Sherry, A. D. Alternatives to Gadolinium-Based Metal Chelates for Magnetic Resonance Imaging [†]. *Chem. Rev.* **2010**, *110* (5), 2960–3018.
9. Terreno, E.; Castelli, D. D.; Viale, A.; Aime, S. Challenges for Molecular Magnetic Resonance Imaging. *Chem. Rev.* **2010**, *110* (5), 3019–3042.
10. Bloembergen, N. Proton Relaxation Times in Paramagnetic Solutions. *J. Chem. Phys.* **1957**, *27* (2), 572–573.
11. Solomon, I. Relaxation Processes in a System of Two Spins. *Phys. Rev.* **1955**, *99* (2), 559–565.
12. Bottrill, M.; Kwok, L.; Long, N. J. Lanthanides in Magnetic Resonance Imaging. *Chem. Soc. Rev.* **2006**, *35* (6), 557–571.

13. Hwang, L.-P.; Freed, J. H. Dynamic Effects of Pair Correlation Functions on Spin Relaxation by Translational Diffusion in Liquids. *J. Chem. Phys.* **1975**, *63* (9), 4017-4019.
14. Weinmann, H.; Brasch, R.; Press, W.; Wesbey, G. Characteristics of Gadolinium-DTPA Complex: A Potential NMR Contrast Agent. *Am. J. Roentgenol.* **1984**, *142* (3), 619–624.
15. Lohrke, J.; Frenzel, T.; Endrikat, J.; Alves, F. C.; Grist, T. M.; Law, M.; Lee, J. M.; Leiner, T.; Li, K.-C.; Nikolaou, K.; et al. 25 Years of Contrast-Enhanced MRI: Developments, Current Challenges and Future Perspectives. *Adv. Ther.* **2016**, *33*, 1–28.
16. Idée, J.-M.; Port, M.; Raynal, I.; Schaefer, M.; Le Greneur, S.; Corot, C. *Fundam. Clin. Pharmacol.* **2006**, *20*, 563-76.
17. Sherry, A. D.; Caravan, P.; Lenkinski, R. E. *J. Magn. Reson. Imaging* 2009, *30*, 1240-1248.
18. Boros, E.; Gale, E.M.; Caravan, P., *Dalton. Trans.*, 2015, 4804-4818.
19. Major JL, Meade TJ. *Acc. Chem. Res.* **2009**, *42*, 893- 903.
20. De Leon-Rodriguez, L.M, Lubag, A.J.M; Malloy, C.R.; Martinez, G.V.; Gillies, R.J.; Sherry, A.D., *Acc. Chem. Res.* **2009**, *42*, 948-957.
21. Tu, C.; Osborne, E. A.; Louie, A.Y., *Ann. Biomed. Eng.* **2011**, *39*, 1335-1348.
22. Tsitovich, P.B.; Burns, P. J.; McKay, A.M.; Morrow, J.R., *J. Inorg. Biochem.* **2014**, *133*, 143-154.
23. Bonnel, C.S.; Tei, L.; Botta, M.; To the, E., Chemistry of Contrast agents in Medical Magnetic Resonance Imaging, Second Ed, Ed, Merbarch, A.E.; Helm, E.; Toth, E., John Wiley and Sons, Chichester, **2013**, 343-385.
24. Moats, R. A.; Fraser, S. E.; Meade, T. J. *Angew. Chem., Int. Ed. Engl.* **1997**, *36*, 726-728.
25. Louie, A.; Huber, M.M.; Arhens, E.T.S.; Rothbacher, U.; Moats, R.; Jacobs, R.E.; Fraser, S.E.; Meade, T.J., *Nat. Biotechnol.*, **2000**, *18*, 321-325.
26. Hanaoka, K.; Kikuchi, K.; Terai, T.; Komatsu, T.; Nagamo, T.; *Chem-Eur. J.*, **2008**, *14*, 987- 996.
27. Chang, Y.T.; Cheng, C.M.; Su, Y.Z.; Lee, W.T.; Hsu, J.S.; Liu, G.L.; Cheng, T.L.; Wang, Y.M., *Bioconjugate Chem*, **2007**, *18* 1716-1727.

28. Chang, M.; Cheng, C.; Su, Y.; Lee, W.; Hsu, J.; Liu, G.; Cheng, J.; Wang, Y., *Bioconjugate Chem.*, **2007**, 18, 1716-1727.
29. Yoo, B.; Pagel, M.D. *J. Am. Chem. Soc.* **2006**, 128, 14032-14033.
30. Woods, M.; Kiefer, G. E.; Bott, S.; Castillo-Muzquiz, A.; Eshelbrenner, C; Michaudet, L.; McMillan, K.; Mudigunda, S. D. K.; Ogrin, D.; Tircso, G.; Zhang, S.; Zhao, P.; Sherry, A. D. *J. Am. Chem. Soc.* **2004**, 126, 9248-9256.
31. Zhang, S.; Trokowski, R.; Sherry, A. D. *J. Am. Chem. Soc.* **2003**, 125, 15288-15289.
32. Aime, S.; Delli Castelli, D.; Fedeli, F.; Terreno, E. *J. Am. Chem. Soc.* **2002**, 124, 9364-9365
33. Aime, S.; Botta, M.; Gianolio, E.; Terreno, E. *Angew. Chem., Int. Ed.* **2000**, 39, 747-750.
34. Esqueda, A. C.; López, J. A.; Andreu-de-Riquer, G.; Alvarado-Monzón, J. C.; Ratnakar, J.; Lubag, A. J. M.; Sherry, A. D.; De León-Rodríguez, L. M. *J. Am. Chem. Soc.* **2009**, 131, 11387- 11391.
35. Yu, J.; Martins, A.F.; Preihs, C.; Clavijo-Jordan, V.; Chirayil, S.; Zhao, P.; Wu, Y.; Nasr, K.; Kiefer, G.E.; Sherry, A.D., *J. Am. Chem. Soc.*, **2015**, 137, 44, 14173–14179.
36. Que E. L.; Chang, C. J., *J Am Chem Soc*, **2006**, 128: 15942-15943.
37. Li, W., Fraser, S. E., Meade, T. J. A., *J Am Chem Soc*, **1999**, 121: 1413-1414.
38. Lubag, A. J. M.; De Leon-Rodriguez, L. M.; Burgess, S. C.; Sherry, A. D, *Proc. Natl. Acad. Sci. U. S. A.*, **2011**, 108, 18400–18405.
39. Martins, A.F.; Jordan, V.C.; Bochner, F.; Chirayil, S.; Paranawithana, N.; Zhang S.; Su-Tang Lo, S.; , Wen, X.; Zhao, P.; Neeman, M.; Sherry, A.D., *J. Am. Chem. Soc.* In Press.
40. Raghunand, N.; Howison, C.; Zhang, S.; Sherry, A.D.; Gillies, R.J., *Magnetic Resonance in Medicine*. 2003, 49, 249-257.
41. Rapp, J.H; Wolff, S.D; Quinn, S.F; Soto, J.A.; Meranze, S.G.; Muluk, S.; Blebea, J.; Johnson, S.P.; Rofsky, N.M.; Duerinckx, A.; Foster, G.S.; Kent, K.C.; Moneta, G.; Middlebrook, M.R.; Narra, M.R.; Toombs, B.D.; Pollak, J.; Yucel , E.K.; Shamsi, K.; Weisskoff , R. M., *Radiology*. **2005**, 236, 71-77.
42. Goyen, M.; Edelman, M.; Perreault, P.; O'Riordan, E.; Bertani, H.; Taylor, J.; Siragusa, D.; Sharafuddin, M.; Mohler, E.R.I.; Breger, R.; Yucel, E.K.; Shamsi, K.; Weisskoff, R. M., *Radiology*. **2005**, 236, 825-833.

43. Lauffer, R.B., *Magn. Reson. Med.* **1991**, 22, 339-342.
44. Chen, J.W.; Pham, W.; Weissleder, R.; Bogdanov, A.; *Magn Reson Med*, **2004**, 52, 1021–1028.

CHAPTER 2
A RESPONSIVE MRI CONTRAST AGENT FOR DETECTION OF EXCESS
COPPER (II) IN THE LIVER IN VIVO

Authors -Namini N. Paranawithana,¹ Andre F. Martins,¹ Veronica Clavijo-Jordan,² Piyu Zhao,¹
Sara Chirayil,² Gabriele Meloni¹ and A. Dean Sherry^{1,2}

¹The Department of Chemistry and Biochemistry, BE26

The University of Texas at Dallas

800 West Campbell Road

Richardson, Texas 75080-3021

²Advanced Imaging Research Center

The University of Texas Southwestern Medical Center

2201 Inwood Road

Dallas, Texas 75390-8568

This chapter is submitted as a preprint in ChemRxiv. (doi: 10.26434/chemrxiv.7359095) and for Journal of American Chemical Society.

NP, VCJ, PZ and GM carried out the experiments. NP, GM, AFM, VCJ and SC performed the data analysis. NP, GM, AFM and ADS conceived the project and drafted the manuscript. All authors read and approved the manuscript.

2.1. Abstract

The design, synthesis, and properties of a new gadolinium-based copper-responsive MRI contrast agents are presented in detail here. The sensor (GdL1) has high selectivity for copper ions and exhibits a 47% increase in r_1 relaxivity upon binding to 1 equivalent of Cu^{2+} in aqueous buffer. Interestingly, in the presence of physiological levels of human serum albumin (HSA), the r_1 relaxivity is amplified even further up to 270%. Additional spectroscopic and XAS studies show that Cu^{2+} is coordinated by two carboxylic acid groups and the single amine group on an appended side-chain of GdL1 and forms a ternary complex with HSA (GdL1- Cu^{2+} -HSA). T_1 -weighted *in vivo* imaging demonstrates that GdL1 can detect basal, endogenous labile copper (II) ions in living mice. This offers a unique opportunity to explore the role of copper ions in the development and progression of neurological diseases such as Wilson disease.

2.2. Introduction

Copper is the third most abundant transition metal in the body and a required dietary nutrient. The average healthy human has a total of ~110mg of tissue copper.¹⁻⁴ Copper is typically bound to specific proteins and enzymes where it plays fundamental catalytic and structural roles.⁵⁻⁷ Copper is also been associated with signaling events in the brain.⁸⁻¹⁰ In biology, copper is present in two oxidation states, the cuprous (Cu^+) and cupric (Cu^{2+}) ions.¹¹ Typically, total extracellular Cu^{2+} can vary widely from nM to μM while intracellular Cu^+ can vary from μM to mM.¹²⁻¹⁴ Due to its redox properties, copper homeostasis is tightly regulated in cells and disruption of homeostasis is associated with a number of neurodegenerative diseases including Alzheimer's, Parkinson's, prion diseases, familial amyotrophic lateral sclerosis, Menkes and Wilson's diseases.¹⁵⁻¹⁸ For instance,

genetic mutations of copper-transporting proteins ATP7A and ATP7B results in afflictions of systemic brain copper deficiency in Menkes disease and hyperaccumulation of hepatic copper ions in Wilson's disease, respectively.¹⁹⁻²² This leads to abnormal levels of copper ions from a few micromolar to several millimolar in concentration, contributing to detrimental neurological effects.²³ Although copper ion homeostasis and the impact of abnormal copper levels on physiology have been widely studied, details about the functional role of copper ions in various tissues *in vivo* remain insufficiently understood due to lack of real-time copper imaging techniques in live animals.^{24,25}

Magnetic resonance imaging (MRI) is a powerful medical diagnostic technique that allows noninvasive, three-dimensional visualization of tissue with high spatial and temporal resolution. MRI is largely based on detection of water and fat protons so image contrast among tissues reflects differences in proton content, cell density, and water perfusion and diffusion. Image contrast can be altered by use of paramagnetic inorganic complexes that shorten the $T_{1,2}$ relaxation times of water molecules in various compartments. These agents are commonly known as contrast agents (CAs). Among all paramagnetic complexes designed for use as CAs, the Gd^{3+} -based agents have proven to be the safest and most versatile agents for clinical use over the past ~30 years. The efficiency of an agent per unit concentration is commonly reported as R_1 (T_1^{-1}) or R_2 (T_2^{-1}) relaxivity.²⁶⁻²⁸ Notably, the design of contrast agents that alter the T_1 of water protons in response to a given analyte is of major importance. Many responsive probes have been reported including sensors for metal ions,²⁹ enzyme activity,³⁰ pH,³¹ pO_2 ,³² and temperature.³³ One of the first reports of a copper-activated MR sensor was based on a Gd-DO3A (1,4,7,10-tetraazacyclododecane-1,4,7,-triacetic acid) derivative having a iminodiacetate pendant arm for Cu^{2+} recognition. This

derivative displayed a 41% increase in r_1 relaxivity upon binding Cu^{2+} .³⁴ The same authors later reported a series of copper MR sensors containing various donor atoms (N,S,O) with greater selectivity for Cu^+ over Cu^{2+} .³⁵ These copper-responsive MRI agents displayed interferences with several biological components and competing cations and anions (Zn^{2+} , HCO_3^-) so their potential use *in vivo* was limited.^{34,36} Other approaches have included imaging copper directly by positron emission tomography (PET) or using an optical imaging technique. The positron emitter, ^{64}Cu , was successfully used to image greater uptake and accumulation of copper in livers of Wilson's disease mouse model.²⁴ Similarly, a near-infrared fluorescent sensor for Cu^+ ions has been shown capable of monitoring fluctuations in exchangeable copper stores in living cells and mice under basal conditions, as well as in situations of copper overload or deficiency.³⁷

Our group recently reported several MR zinc-sensors capable of detecting the release of intracellular stores of zinc into extracellular space in the prostate³⁸ and pancreas of live mice.³⁹ The zinc ions released by cells in these organs is immediately chelated by a zinc-responsive MR agent, and the resulting binary complex then forms a ternary complex with human serum albumin (HSA). This results in reduced molecular motion of the Gd-based sensor, and an increase r_1 .^{40,41} Copper is also known to bind to HSA and other less abundant proteins in plasma.⁴²⁻⁴⁶ Hence, we hypothesized that the key to an effective copper detection *in vivo* by MRI might be to design a Cu-responsive agent that also forms a ternary complex between Cu^{2+} ions, the sensor, and HSA, similar to the Zn-sensor designs.

Herein, we report a novel copper-responsive MRI contrast agent having a bis(benzoic acid)methylamine recognition motif (GdL1) and physicochemical properties of the GdL1- Cu^{2+} complex and the ternary complex formed with HSA. We also used multinuclear NMR and X-ray

absorption spectroscopy (XAS) and structural analogs to interrogate the Cu^{2+} binding site in this system. Finally, GdL1 was injected into mice to detect extracellular copper in the liver by MRI. A comparison of GdL1 (high Cu^{2+} affinity) with GdL2 and GdL3 (lower Cu^{2+} affinity) (Figure 2.1) indicated that only GdL1 detects extracellular copper in mouse livers.

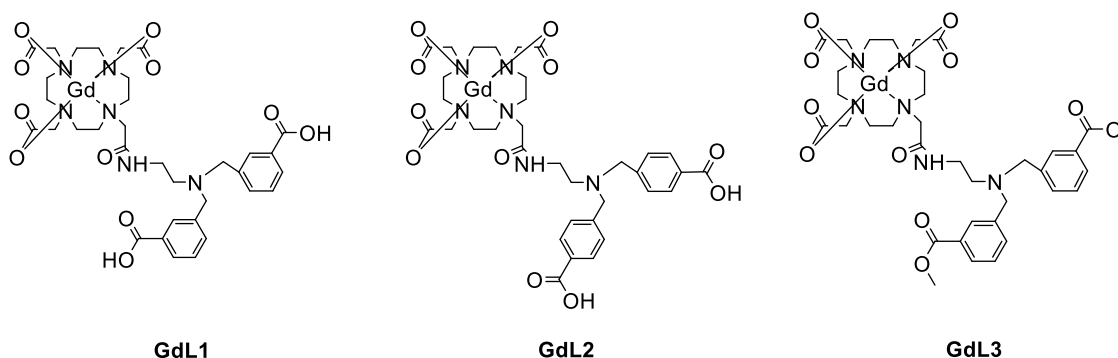


Figure 2.1. Gadolinium-DO3A based copper responsive (GdL) agents.

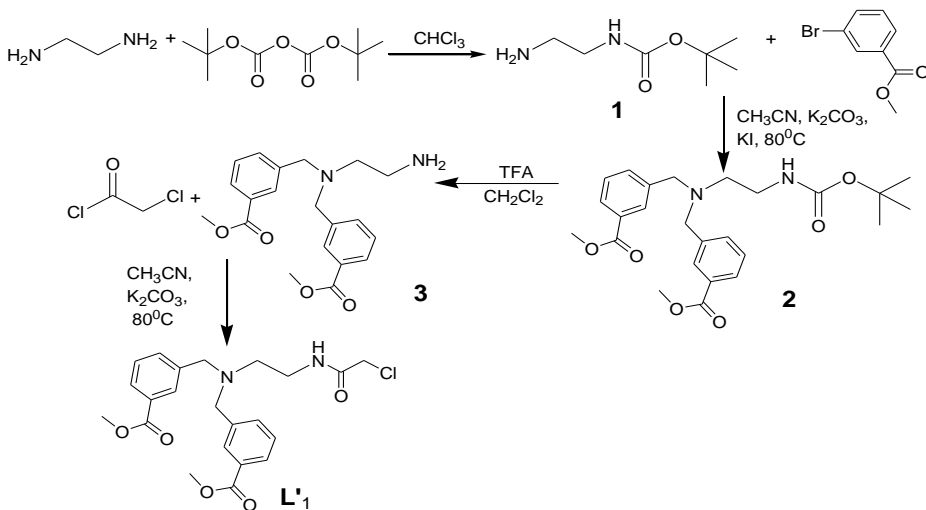
2.3 Experimental Section

2.3.1 Materials and Methods

DO3A-tBu₃ was synthesized according to the reported procedure in literature.⁴⁷ Chemicals were purchased from Sigma-Aldrich (St. Louis, MO), Strem (Newburyport, M), Acros Organics (Morris Plains, NJ), TCI America (Portland, OR), and Alfa Aesar (Ward Hill, MA). They were used as received unless otherwise noted. Human Serum Albumin (HSA, fatty acid and globulin free) was purchased from Sigma-Aldrich. Column chromatography was performed using Silica gel (200-400 mesh, 60A°), purchased from Sigma-Aldrich. Analytical Thin Layer Chromatography was performed using EMD Millipore precoated aluminum oxide or Whatman precoated Silica gel on a polyester plate. Analytical HPLC was performed on an Agilent

Technologies 1220 Infinity LC using a RESTEK Ultra C-18 IBD column (3 μm , 100 \times 4.6 mm). Preparative HPLC was performed on a Waters Delta Prep HPLC system equipped with a Water® 2996 photodiode array detector and a Phenomenex Kinetex® C18 column (5 μm , 21.2 mm x 250 mm) or an Atlantis Prep T3 OBD Column (5 μm , 30 mm x 250 mm). A Fisher Science Education pH-meter coupled with Thermo Scientific Orion Micro pH electrode was used for pH measurements. Milli-Q purified water was used for the preparation of all samples and preparative and analytical HPLC. ^1H and ^{13}C NMR spectra were obtained in deuterated solvents from Cambridge Isotope Laboratories (Cambridge, MA) on a Bruker AVANCE III 400 MHz NMR spectrometer for all synthetic intermediates, final products, ^{17}O temperature studies of all lanthanide complexes. A VirTis Freeze Dryer (Benchtop-k) was used to lyophilize the samples. Mass spectra were obtained using either HT Laboratories (San Diego, CA) instrument or a Waters Alliance e2695 Separations Module coupled with Xevo QToF MS using an Atlantis T3 Column (5 μm , 6 mm x 250 mm) at The Advanced Imaging Research Center (University of Texas Southwestern Medical Center, Dallas). Inductive coupled plasma mass spectrometry (ICP-MS) was performed for calculating metal concentrations using Agilent 7900. Standard solutions for ICP-MS containing Gd, Eu, La, and Yb were purchased from Inorganic Ventures (Christiansburg, VA). Florescence Measurements were collected in Horiba Fluoromax 4 (Albany, NY) spectrofluorometer. Electronic Paramagnetic Resonance spectroscopy was performed in Bruker EMX Spectrometer with ER 041 XG microwave bridge. Chemical structures and IUPAC names were obtained using Chemaxon MarvinSketch 17.11 and ChemdrawUltra 7.0.⁴⁸

2.3.2 Synthesis



Scheme 2.1. Synthesis of L'1.

methyl 3-(((2-((chloroacetyl)amino)ethyl)(3-(methoxycarbonyl)benzyl)amino)methyl)benzoate (L'1)

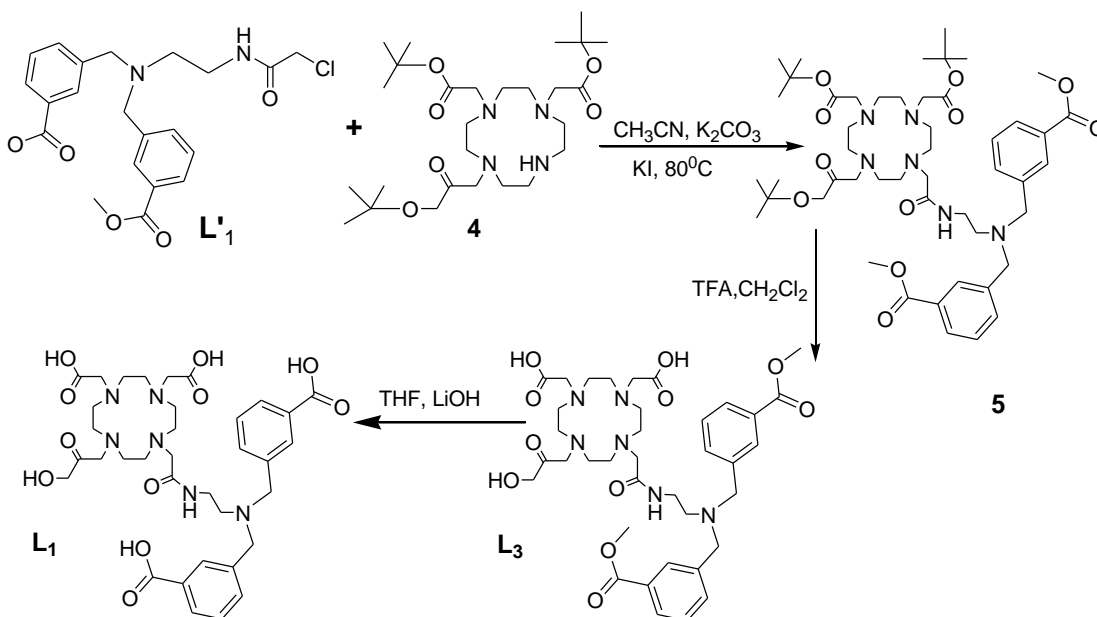
Synthetic procedure for compound **1** was reported previously.⁴⁹ Compound **1** (1.0 g, 6.25 mmol) was dissolved in acetonitrile (CH₃CN) 100 ml. 3-Bromomethyl benzoic acid (3.0 g, 13.8 mmol) was added with potassium carbonate (3.45 g, 25.0 mmol) and potassium iodide (0.5 g, 3.0 mmol), increased solvent volume up to 250 ml. The reaction mixture was refluxed at 80°C for 18 hrs. The resulted mixture was filtered, the solvent was removed in vacuo. The residue was dissolved in dichloromethane and purified with a SiO₂ column using dichloromethane and methanol (R_f = 0.65) to obtain compound **2**. Compound **2** (2.3 g, 5.0 mmol) was dissolved in CH₂Cl₂ (5 ml) and TFA (10.5 ml) and kept at room temperature for 16 hrs to obtain compound **3**. Compound **3** (1.6 g, 4.5 mmol) was dissolved in CH₃CN and chloroacetyl chloride (0.6 ml, 6.25 mmol) potassium carbonate (3.0 g, 22.0 mmol) was added. The mixture was refluxed for 72 hrs, followed by filtration and solvent was removed by rotary evaporation

to obtain the residue. The residue was dissolved and purified with SiO₂ by CH₂Cl₂ and CH₃OH (R_f = 0.75) to obtain L'₁.

¹H NMR (400 MHz, CDCl₃, TMS): δ 2.62 (2H, s, CH₂NCH₂CH₂N), 3.32 (2H, s, CH₂NCH₂CH₂N), 3.64 (4H, s, PhCH₂N), 3.86 (6H, s, CH₃OCOPh), 4.12 (2H, s, NCOCH₂Cl), 7.39 (8H, s, HPh)

¹³C NMR (400 MHz, CDCl₃, TMS): δ 37.05 (NCH₂CH₂N), 42.57 (NCOCH₂Cl), 51.99 (CH₃OCOPh), 53.83 (NCH₂CH₂NHCO), 58.14 (PhCH₂NCH₂), 128.55 (PhC), 166.84 (CH₃OCOPh)

MS (ESI-positive) m/z = 432.46 [M-H⁺] (calculated 432.20)



Scheme 2.2. Synthesis of L₁.

3-(((2-(((4,7-bis(carboxymethyl)-10-(3-hydroxy-2-oxopropyl)-1,4,7,10-tetraazacyclododecan-1-yl)acetyl)amino)ethyl)(3-carboxybenzyl)amino)methyl)benzoic acid (L₁)

The compound L'₁ (1.5 g, 3.5 mmol) was dissolved in CH₃CN (150 ml). The compound **4** (1.7 g, 3.3 mmol) together with K₂CO₃ (1.0 g, 7.25 mmol) and KI (0.5 g, 3.0 mmol) were added. The resultant solution was reflux for 48 hrs, and the solvent was removed by rotary evaporation. The residue was dissolved and purified in SiO₂ with CH₂Cl₂ and CH₃OH (R_f = 0.59) to obtain compound **5**. LiOH (0.91 g, 3.8 mmol) was added to compound **5** (2.4 g, 2.55 mmol) in THF (5 ml). The solvents were evaporated in vacuo to obtain L₃. Compound L₃ (2.0 g, 2.45 mmol) was dissolved in CH₂Cl₂ was dissolved in TFA (50 ml) and stirred for 6 hrs, and the solvent was evaporated to obtain L₁ (1.5 g, 2.0 mmol). The products L₃ and L₁ were purified with preparative HPLC.

For L₃,

¹H NMR (400 MHz, MeOD, TMS): δ 2.83 (24 H, m, br, macrocycle CH₂, 2H, s, br, NHCH₂CH₂CO, 2H, s, NHCH₂CH₂NH), 3.25 (2H, s, NHCH₂CO) , 3.91 (4H, s, NCH₂Ph) , 4.25 (6H, s, COOCH₃), 7.33 (8H, d, HPh)

¹³C NMR (400 MHz, MeOD, TMS): δ 34.12 (NHCH₂CH₂CO), 42.05(COOCH₃) 49.21 (macrocycle, CH₂), 51.83 (macrocycle, CH₂), 54.61 (NHCH₂CH₂CO), 57.10 (NHCH₂CO), 63.18 (NCH₂Ph), 129.44 (CHPh), 130. 62 (CHPh), 131.94 (CHPh), 135.76 (CHPh), 163.18 (PhCOOH), 173.16 (macrocycle, COOH)

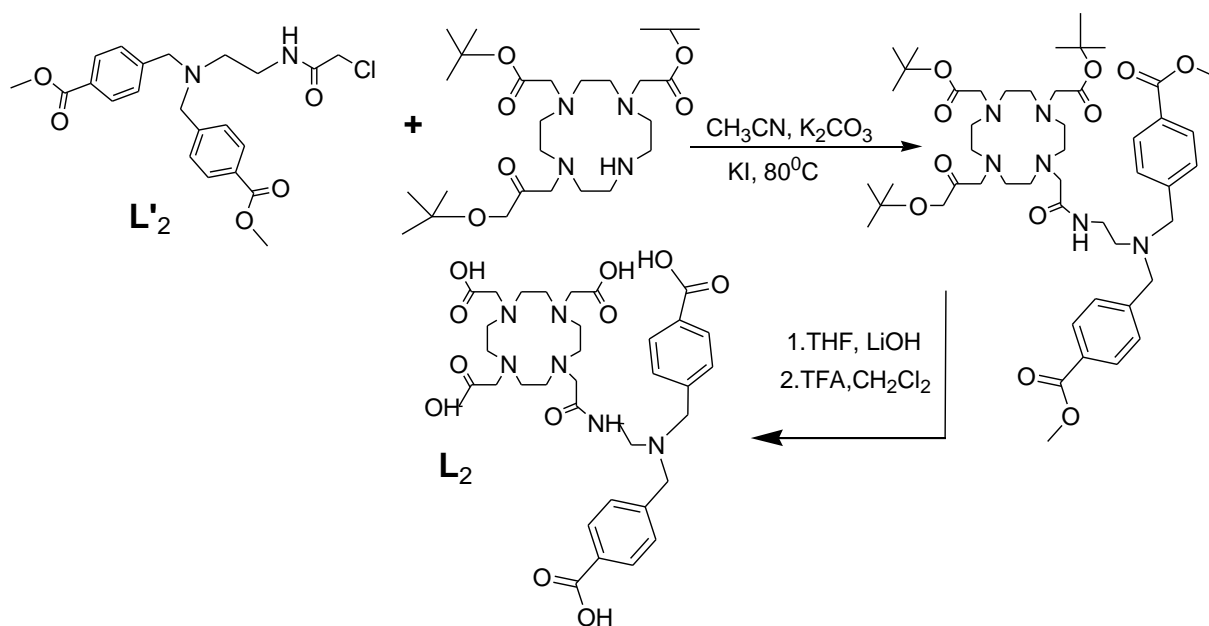
MS (ESI-positive) m/z = 743.30 [M-H⁺] (calculated 742.35)

For L1,

¹H NMR (400 MHz, D₂O, TMS): δ 2.55 (24 H, m, br, macrocycle CH_2 , 2H, s, br, $\text{NHCH}_2\text{CH}_2\text{CO}$, 2H, s, $\text{NHCH}_2\text{CH}_2\text{NH}$), 3.25 (2H, s, NHCH_2CO), 3.59 (4H, s, NCH_2Ph), 7.33 (8H, d, HPh)

¹³C NMR (400 MHz, D₂O, TMS): δ 36.54 ($\text{NHCH}_2\text{CH}_2\text{CO}$), 50.82 (macrocycle, CH_2), 53.41 ($\text{NHCH}_2\text{CH}_2\text{CO}$), 56.13 (NCH_2Ph), 129.15 (CHPh), 130.00 (CHPh), 132.67 (CHPh), 167.54 (PhCOOH), 171.26 (macrocycle, COOH)

MS (ESI-positive) m/z = 715.10 [M-H^+] (calculated 714.32)



Scheme 2.3. Synthesis of **L₂**.

4-(((2-(((4,7-bis(carboxymethyl)-10-(3-hydroxy-2-oxopropyl)-1,4,7,10-tetraazacyclododecan-1-yl)acetyl)amino)ethyl)(4-carboxybenzyl)amino)methyl)benzoic acid (L₂)

The compound L'₂ was synthesized by using 4-Bromomethyl benzoic acid and Compound 1 following the same procedure as for L'₁. The compound L'₂ (1.5 g, 3.5 mmol) was dissolved in CH₃CN and followed the same synthesis procedure as in L₁ to obtain compound L₂ (1.1g, 1.5 mmol).

For L₁,

¹H NMR (400 MHz, D₂O, TMS): δ 2.69 (24 H, m, br, macrocycle CH₂, 2H, s, br, NHCH₂CH₂CO, 2H, s, NHCH₂CH₂NH), 3.28 (2H, s, NHCH₂CO), 4.34 (4H, s, NCH₂Ph), 7.37 (8H, d, HPh)

¹³C NMR (400 MHz, D₂O, TMS): δ 36.54 (NHCH₂CH₂CO), 51.49 (macrocycle, CH₂), 51.88 (macrocycle, CH₂), 57.62 (NHCH₂CH₂CO), 58.00 (NHCH₂CO), 61.20 (NCH₂Ph), 128.89 (CHPh), 130.15 (CHPh), 132.53 (CHPh), 136.32 (CHPh), 163.18 (PhCOOH), 173.16 (macrocycle, COOH)

MS (ESI-positive) m/z = 715.0 [M-H⁺] (calculated 714.32)

2.3.3 General Procedure for preparation and characterization of lanthanide-ligand complexes

The ligand (L₁, L₂, and L₃) was dissolved in MilliQ grade water and mixed with a lanthanide chloride (Gd, La, Eu) in 5-10% excess stoichiometric amount. The solution pH was adjusted to 6.0-6.5 by addition of NaOH and stirred at room temperature for 18 hrs. Unreacted Gd³⁺ was Gd(OH)₃ by raising the pH to 9.0 with the addition of 1 M NaOH. The crude residue was purified with preparative HPLC to obtain the Complex and characterized by LC-MS.

MS GdL₃ (ESI-positive) m/z = 898.10 [M-H⁺] (calculated 897.05)

MS GdL₁ and GdL₂ (ESI-positive) m/z = 869.74 [M-H⁺] (calculated 869.01)

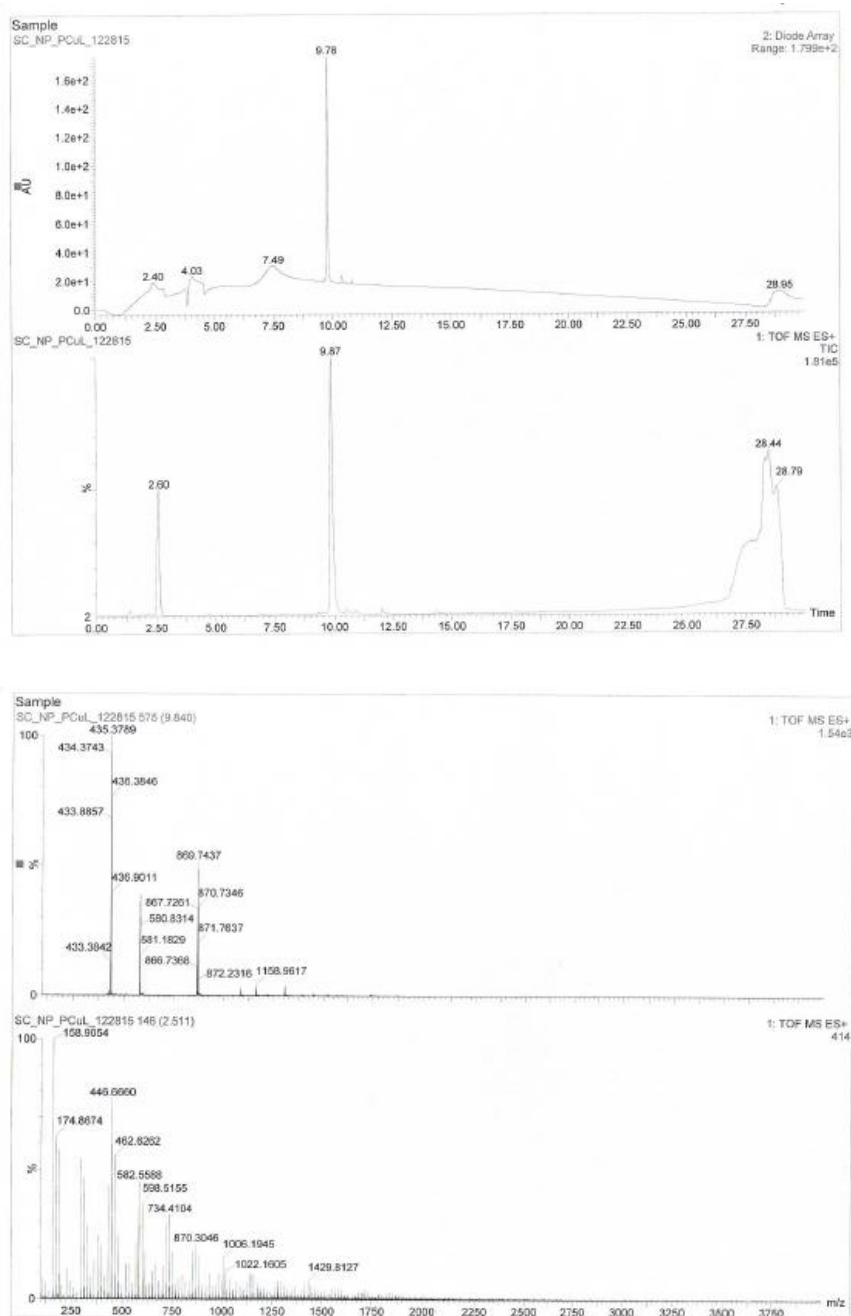


Figure 2.2. LC-MS of GdL1 Complex

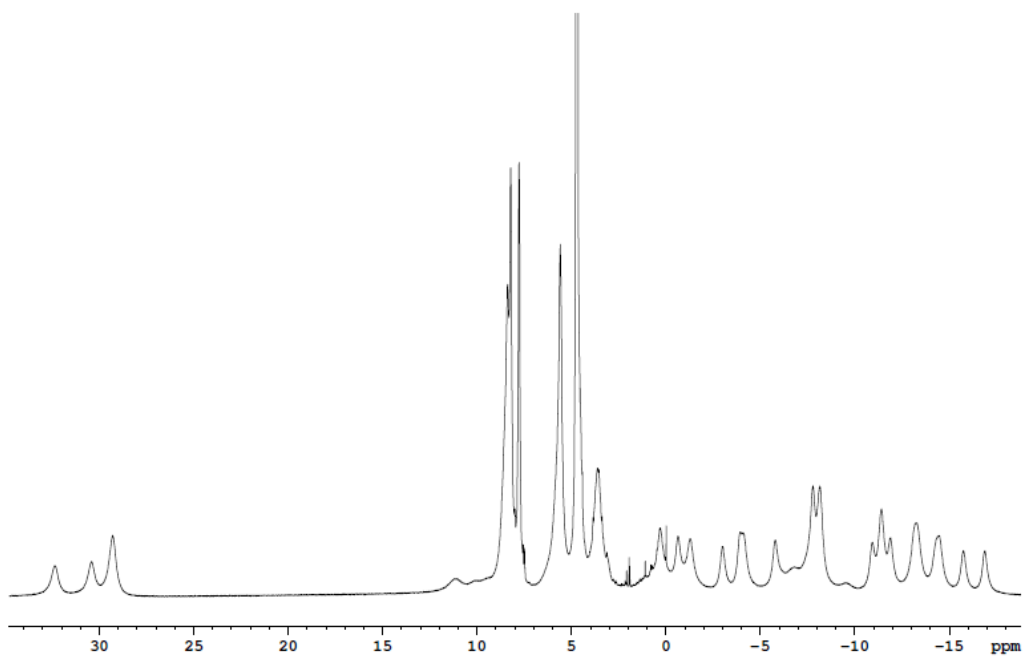


Figure 2.3. ^1H NMR spectrum of EuL1 showing square antiprism (SAP) and twisted square antiprism (TSAP) structure in an approximate 4:1 ratio.

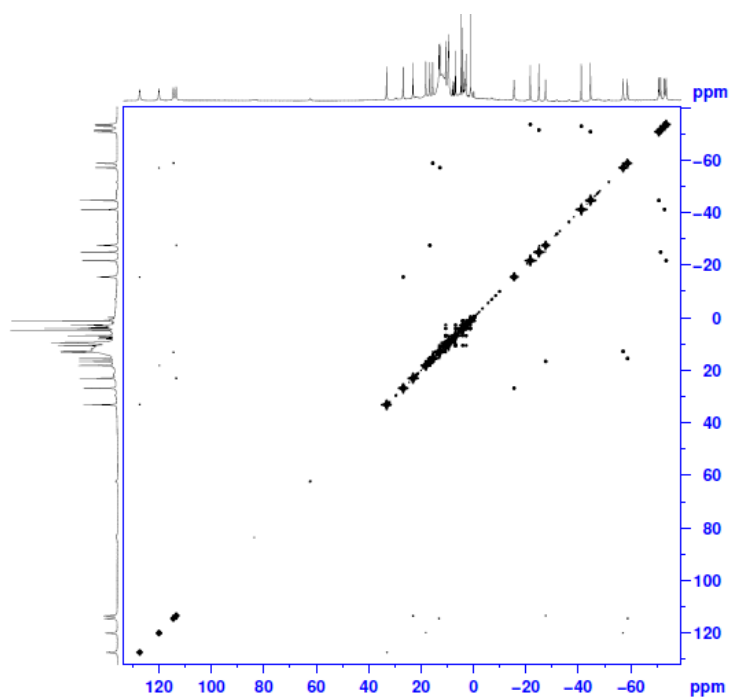


Figure 2.4. 2D-COSY spectrum of 80 mM YbL1.

2.3.4 Relaxivity Measurements

Longitudinal relaxivity values were measured in MRS-6 NMR analyzer at 20 MHz and determined from the slope of the line of $1/T_1$ versus the concentration of Gadolinium. Various solutions with different concentrations of GdL complexes were prepared in 0.1 M MOPS buffer pH= 7.4 or buffer with 600 μ M HSA. CuCl_2 , ZnCl_2 , MgCl_2 , CaCl_2 and FeCl_3 was then added to each of above complex solutions to produced desired $[\text{GdL}]: [\text{M}^{n+}]$ ratios for the titrations. After 30 min of incubation at 310 K, T_1 measurements were made at same temperature using warm air blower.

The MOPS buffer was used in all the measurements due to its weak interaction with Cu^{2+} .

2.3.5 Job's Plot

Longitudinal relaxivity data were obtained as described above at 20 MHz. Various concentrations of a solution of GdL1 complexes were prepared in 0.1 M MOPS buffer at pH 7.4, and the CuCl_2 solution was added to obtain desired molar ratios for the titration. The total concentration of GdL1 and Cu^{2+} were kept constant at 0.2 mM. A titration of GdL1 and Cu^{2+} was carried out by varying the mole fractions, but the total concentration of GdL1 and Cu^{2+} kept constant at 0.2 mM.

2.3.6 Determination of the GdLx- Cu^{2+} binding constants by fluorescence

A 35 μ M solution of GdL1-3 was prepared in 10mM Tris buffer (pH = 7.4) and titrated with 100 mM CuCl_2 stock solution. Addition of Cu^{2+} results in quenching of the native fluorescence of each GdL1-3 complex. The fluorescence intensity was measured upon each addition of Cu^{2+} at 25°C using a Fluoromax-4 Spectro fluorimeter in a 1cm quartz cuvette (Horiba). The excitation wavelength for all GdL sensors was at 260 nm. The emission wavelength for GdL1 was 350 nm while the emission wavelength for GdL2 and GdL3 was 404 nm and 326 nm respectively. The GdL- Cu^{2+} dissociation constant was determined by fitting the data to the following equation:

$$\Delta F = (\Delta F_{\max} [\text{Cu}^{2+}]) / (K_d + [\text{Cu}^{2+}])$$

2.3.7 Determination of Cu mediated ternary complex formation by Size-Exclusion Chromatography

Equimolar solutions (100 μM) of LaL1: HSA: Cu^{2+} , LaL1: Cu^{2+} and LaL1: HSA were prepared and purified with size exclusion chromatography in Hi-trap desalting column (5 ml, 1.6 X 2.5 cm) using an FPLC (AKTA, GE HealthCare). Each collected peak was analyzed for La^{3+} ion concentration in 4% HNO_3 solutions using ICP-MS.

2.3.8 Determination of dissociation constant of GdL-Cu-HSA by relaxometry measurements

Dissociation constants to HSA were determined by proton relaxation enhancement (PRE) measurements according to published procedures.^{50,51} The proton relaxation rates at increasing concentrations of protein were measured with a MRS-6 NMR analyzer (20 MHz, 310 K). For the E-titration, the concentrations of GdL complex (0.1 mM) and Cu^{2+} (0.1 mM) were kept constant, while HSA concentration was varied from 0 to 1 mM. ($[\text{GdL}]: [\text{Cu}^{2+}] = 1:1$)

2.3.9 Determination of dissociation constant of GdL-Cu-HSA by fluorescence

A solution containing 5 μM of dansylglycine (or warfarin), 5 μM HSA, 400 μM GdL1 with 5 μM of Cu^{2+} was prepared in MOPS buffer. Aliquots of this solution were 2-fold diluted serially ten times by addition of a solution which contained the same concentrations of dansylglycine (or warfarin) and HSA but no agent. The fluorescence of 100 μL aliquots was measured in duplicate in 96 well plates. Similarly, solutions containing agent, HSA but no dansylglycine (warfarin), were also included. Four 100 μL aliquots of the solution containing no agent (maximum fluorescent intensity) were also measured in the same 96-well plate, along with four 100 μL aliquots of HSA in the buffer. Further, the same procedure was repeated to find the K_D in the absence of GdL1, by replacing the GdL1 agent with 400 μM CuCl_2 solution. The excitation and emission wavelengths used for the dansylglycine: 360 and 465 nm and warfarin: 320 and 380 nm, respectively. Fitting was done with OriginPro8 from Origin

Lab Corporation. The competitor is the Cu/Gd agent. K_D is the dissociation constant of the fluorescent probe and HSA. For dansylglycine, a K_D of 2.5 μM was used as reported in the literature.⁵² Controls with solutions containing 5 μM of dansylglycine alone and 5 μM of dansylglycine (or warfarin) and 5 μM of Cu^{2+} were also measured. Fluorescence values did not show any effect on the measured fluorescence values for both competitors.

2.3.10 ^{17}O NMR measurements

^{17}O NMR experiments were performed at 9.4 T on a Bruker AVANCE III NMR spectrometer and temperature was regulated by air flow controlled by a Bruker VT unit. The samples ($[\text{Gd}^{3+}] = 25.4 \text{ mM}$) were prepared in ^{17}O enriched water (10%) with the pH being maintained at 7.4 with 0.1 M Tris buffer. The sample was loaded into 80 μL spherical bulb (Wilma-Lab Glass, Vineland, NJ) and placed inside a 5 mm NMR tube. Longitudinal relaxation rates ($1/T_1$) were obtained by the inversion recovery method, and transverse relaxation rates ($1/T_2$) were obtained by the Carr–Purcell–Meiboom–Gill spin echo technique. The acidified water (pH = 3.0) containing 10% enriched ^{17}O water was used as a reference for the measurements. The corresponding fittings were performed with the Scientist 3.0 software (Micromath®). ^{17}O NMR data have been analyzed within the framework of Solomon-Bloembergen-Morgan theory as previously reported.⁵³

2.3.11 Analysis of ^{17}O NMR Data

^{17}O NMR data have been analysed within the framework of Solomon-Bloembergen-Morgan theory.

^{17}O NMR spectroscopy

From the measured ^{17}O NMR relaxation rates and angular frequencies of the paramagnetic solutions, $1/T_1$, $1/T_2$ and ω , and of the acidified water reference, $1/T_{1A}$, $1/T_{2A}$ and ω_A , one can calculate the reduced relaxation rates and chemical shifts, $1/T_{2r}$ and ω_r , which may be written in Equations (A1)-(A3), where, $1/T_{1m}$, $1/T_{2m}$ is the relaxation rate of the bound water and $\Delta\omega_m$ is the chemical shift difference between

bound and bulk water molecules, τ_m is the mean residence time or the inverse of the water exchange rate k_{ex} and P_m is the mole fraction of the bound water.

$$\frac{1}{T_{1r}} = \frac{1}{P_m} \left[\frac{1}{T_1} - \frac{1}{T_{1A}} \right] = \frac{1}{T_{1m} + \tau_m} + \frac{1}{T_{1os}} \quad (A1)$$

$$\frac{1}{T_{2r}} = \frac{1}{P_m} \left[\frac{1}{T_2} - \frac{1}{T_{2A}} \right] = \frac{1}{\tau_m} \frac{T_{2m}^2 + \tau_m^{-1} T_{2m}^{-1} + \Delta\omega_m^2}{(\tau_m^{-1} + T_{2m}^{-1})^2 + \Delta\omega_m^2} + \frac{1}{T_{2os}} \quad (A2)$$

$$\Delta\omega_r = \frac{1}{P_m} (\omega - \omega_A) = \frac{\Delta\omega_m}{(1 + \tau_m T_{2m}^{-1})^2 + \tau_m^2 \Delta\omega_m^2} + \Delta\omega_{os} \quad (A3)$$

The outer sphere contributions to the ^{17}O relaxation rates $1/T_{1os}$ and $1/T_{2os}$ are being neglected according to previous studies. Therefore, Equations (A1-A2) can be further simplified to Equations (A4) and (A5):

$$\frac{1}{T_{1r}} = \frac{1}{T_{1m} + \tau_m} \quad (A4)$$

$$\frac{1}{T_{2r}} = \frac{1}{T_{2m} + \tau_m} \quad (A5)$$

The exchange rate is supposed to obey the Eyring Equation. In Equation (A6) ΔS^\ddagger and ΔH^\ddagger are the entropy and enthalpy of activation for the water exchange process, and k_{ex}^{298} is the exchange rate at 298.15 K.

$$\frac{1}{\tau_m} = k_{ex} = \frac{k_B T}{h} \exp \left\{ \frac{\Delta S^\ddagger}{R} - \frac{\Delta H^\ddagger}{RT} \right\} = \frac{k_{ex}^{298} T}{298.15} \exp \left\{ \frac{\Delta H^\ddagger}{R} \left(\frac{1}{298.15} - \frac{1}{T} \right) \right\} \quad (A6)$$

In the transverse relaxation, the scalar contribution, $1/T_{2sc}$, is the most relevant [Equation (A7)]. $1/\tau_{s1}$ is the sum of the exchange rate constant and the electron spin relaxation rate [Equation (A8)].

$$\frac{1}{T_{2m}} \cong \frac{1}{T_{2sc}} = \frac{S(S+1)}{3} \left(\frac{A}{\hbar} \right)^2 \left(\tau_{s1} + \frac{\tau_{s2}}{1 + \omega_S^2 \tau_{s2}^2} \right) \quad (\text{A7})$$

$$\frac{1}{\tau_{s1}} = \frac{1}{\tau_m} + \frac{1}{T_{1e}} \quad (\text{A8})$$

The ^{17}O longitudinal relaxation rates in Gd^{3+} solutions are the sum of the contributions of the dipole-dipole (dd) and quadrupolar (q) mechanisms as expressed by Equations (A11-A13) for non-extreme narrowing conditions, where γ_S is the electron and γ_I is the nuclear gyromagnetic ratio ($\gamma_S = 1.76 \times 10^{11} \text{ rad s}^{-1} \text{ T}^{-1}$, $\gamma_I = -3.626 \times 10^7 \text{ rad s}^{-1} \text{ T}^{-1}$), r_{GdO} is the effective distance between the electron charge and the ^{17}O nucleus, I is the nuclear spin (5/2 for ^{17}O), χ is the quadrupolar coupling constant and η is an asymmetry parameter :

$$\frac{1}{T_{1m}} = \left[\frac{2}{5} \left(\frac{\mu_0}{4\pi} \right)^2 \frac{\hbar^2 \gamma_I^2 \gamma_S^2}{r^6} S(S+1) + \frac{3\pi^2}{10} \frac{2I+3}{I^2(2I-1)} \chi^2 (1 + \eta^2/3) \right] \tau_c \quad (\text{A9})$$

with:

$$\frac{1}{T_{1dd}} = \frac{2}{15} \left(\frac{\mu_0}{4\pi} \right)^2 \frac{\hbar^2 \gamma_I^2 \gamma_S^2}{r_{GdO}^6} S(S+1) \times [3J(\omega_I; \tau_{d1}) + 7J(\omega_S; \tau_{d2})] \quad (\text{A10})$$

$$\frac{1}{T_{1q}} = \frac{3\pi^2}{10} \frac{2I+3}{I^2(2I-1)} \chi^2 (1 + \eta^2/3) \times [0.2J_1(\omega_I) + 0.8J_2(\omega_I)] \quad (\text{A11})$$

In Equation (A3) the chemical shift of the bound water molecule, $\Delta\omega_m$, depends on the hyperfine interaction between the Gd^{3+} electron spin and the ^{17}O nucleus and is directly proportional to the scalar coupling constant, $\frac{A}{\hbar}$, as expressed in Equation (A12).

$$\Delta\omega_m = \frac{g_L \mu_B S(S+1) B}{3k_B T} \frac{A}{\hbar} \quad (\text{A12})$$

The isotopic Landé g factor is equal to 2.0 for the Gd^{3+} , B represents the magnetic field, and k_B is the Boltzmann constant. The outer-sphere contribution to the chemical shift is assumed to be linearly related to $\Delta\omega_m$ by a constant C_{os} [Equation (A13)].

$$\Delta\omega_{os} = C_{os} \Delta\omega_m \quad (\text{A } 13)$$

Analysis Details

In the ^{17}O NMR data fitting for the Gd^{3+} complexes, r_{GdO} has been fixed to 2.50 Å, based on available crystal structures and recent electron spin-echo envelope modulation (ESEEM) results. The quadrupolar coupling constant, $\chi (1+\eta^2/3)^{1/2}$, has been set to the value for pure water, 7.58 MHz. The following parameters have been adjusted: the water exchange rate, k_{ex}^{298} , the activation enthalpy for water exchange, ΔH^\ddagger , the scalar coupling constant, A/\hbar , the rotational correlation time (τ_R^{298}) and its activation energy, E_R . The parameters characterizing the electron spin relaxation, such as the correlation time for the modulation of the zero-field-splitting, τ_v^{298} , and its activation energy, E_v , and the mean-square zero-field-splitting energy, Δ^2 were sometimes fixed to 11 ps, 1 kJ mol $^{-1}$, and $0.16 \times 10^{-20} \text{ s}^{-1}$, respectively, for simpler analogy as reported for various Gd-DOTA derivatives. C_{os} was fixed to 0 for the remaining complexes. Inner sphere water molecules were adjusted to the values calculated by ^{17}O NMR for each complex. Underlined values have been fixed in the fitting.

2.3.12 Determination of Kinetic Inertness

Kinetic inertness was determined according to the published procedure with some modifications.^{8,9} The sample (500 μl) for relaxivity measurements was prepared in 30mM phosphate buffer with 1.5 mM GdL1 and 4.5 mM of CuCl_2 . The samples were measured 15 minutes after the sample temperature stabilized at 310 K on 20 MHz NMR analyzer over the time.

2.3.13 Electrochemistry

Cyclic voltammograms were obtained with a CV50-W electrochemical analyzer using a glassy carbon working electrode, an Ag/AgCl reference electrode and a platinum wire auxiliary electrode. Samples were prepared in 0.1M MOPS under N_2 and analyzed using a scan rate of 100 mV/s. $E_{1/2}$ values were the averages of E_{pa} and E_{pc} .

Since the proposed copper binding site assumed to be dianionic carboxylate with an amine, a tridentate receptor, we examined the redox behavior of GdL1 with 1 equivalent of Cu^{2+} . Since GdL1- Cu^{2+} expected to have a small diffusion coefficient, shows the reduction current of the GdL- Cu^{2+} complexation. GdL- Cu^{2+} quasi-reversible signal with oxidation peak at 0.31V and reduction at 0.01 V result in $E_{1/2}=0.16V$, which is comparable to reported value can prove that this binds to Cu^{2+} .^{10,11}

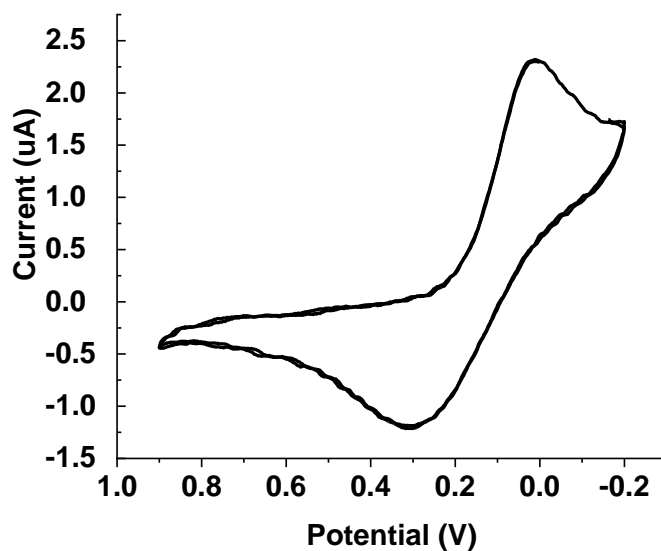


Figure 2.5. Cyclic voltammograms of 0.4 mM GdL1 with 0.4 mM Cu^{2+} acquired in 0.1 M MOPS buffer (pH 7.4) at 25 °C. All potentials are referenced to the standard hydrogen electrode (SHE).

2.3.14 Determination of GdL1-Cu coordination by ^1H -NMR

20 mM solution of LaL1 was prepared and titrated with various concentration (1,10,15,20,25 and 40 mM) of Cu^{2+} . The ^1H NMR of LaL1 was recorded at 37°C with Bruker AVANCE III 400 MHz NMR spectrometer.

2.3.15 EPR

Equimolar solutions (250 μM) of LaL1: HSA: Cu^{2+} , LaL1: Cu^{2+} and Cu^{2+} : HSA were prepared in 10mM MOPS buffer at pH 7.2. All the EPR spectra were obtained at 30K Bruker EMX Spectrometer operating at a microwave frequency of ~ 9.3 GHz. The spectra were recorded at 10 K employing a helium flow cryostat, using a microwave power of 12.8 mW and a modulation amplitude of 10 Gauss.

2.3.16 Determination of metal binding site of HSA by ^{113}Cd NMR

^{111}Cd -NMR spectra (9.4 T on a Bruker AVANCE III NMR spectrometer) were acquired by using a 5-mm BBO probe head, with 0.1 M $\text{Cd}(\text{ClO}_4)_2$ (0 ppm) as an external standard. Proton decoupling was achieved by inverse-gated composite pulse de-coupling and spectra were acquired over a sweep width of 250 ppm, the acquisition time of 1 s, and a recycle delay of 5 s. To gain further insights into selectivity of the primary copper binding site on HSA (NTS vs. MBS), we performed ^{113}Cd NMR studies. Previous reports demonstrated that Cu^{2+} binds preferentially to the NTS site with non-specific binding also occurring at the MBS when Cu^{2+} is in excess.⁵⁶ The Cu^{2+} bound to MBS (also known as zinc binding site A) is easily displaced by the other metals, but not from the primary NTS terminal site.^{57,58} With those considerations, we have repeated the ^{113}Cd NMR experiments reported previously by Sadler et al. to determine the extent to which Cu^{2+} ions could displace Cd^{2+} ions from the MBS site.⁵⁹ The ^{113}Cd NMR spectra showed that excess Cd^{2+} binds at three distinct MBS sites (site A, B, and C).⁵⁹ When 1-molar equivalent of Cu^{2+} was added to an HSA solution containing 2-molar equivalents of Cd^{2+} , only minor changes were observed in the ^{113}Cd signal of site A (Figure 2.6). This

indicates at one molar equivalent, Cu^{2+} binds to a different site other than the MBS site A, B and C, most likely to the selective N-Terminal site. Addition of a second equivalent of Cu^{2+} results in partial displacement of Cd^{2+} from site A and a new peak appears at 135 ppm that increase the population in site C. This provides the evidence that ternary complex selectively forms at NTS site in the presence of equimolar Cu^{2+} concentration with HSA.

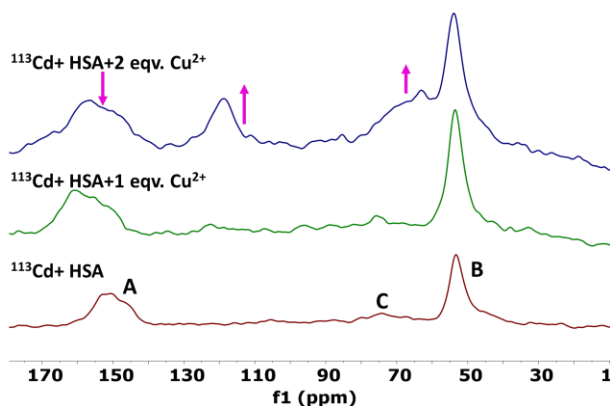


Figure 2.6. ^{113}Cd NMR spectra of (A) 2mM HSA and 6mM $^{113}\text{CdCl}_2$ (B) 2mM HSA, 2mM Cu^{2+} , 4mM LaL1 and 6mM $^{113}\text{CdCl}_2$ (C) 2mM HAS, 4mM Cu^{2+} , 4mM LaL1 and 6mM $^{113}\text{CdCl}_2$ at 59.92 MHz, pD = 7.4 in MOPS buffer.

2.3.17 XAS (XANES and EXAFS)

GdL1- Cu^{2+} , HSA- Cu^{2+} and GdL1- Cu^{2+} -HSA (2mM) in 20 mM MOPS pH 7, 10 % (w/v) glycerol were generated by addition of a CuCl_2 stock solution to GdL1 and/or HSA and loaded into custom made polycarbonate XAS sample cells, sealed with tape, flash frozen in liquid nitrogen and stored in liquid nitrogen until data collection. X-ray absorption spectroscopy measurements were performed at Stanford Synchrotron Radiation Light source with the SPEAR 3 storage ring.

Copper K-edge data were collected using beamline 9-3 with a wiggler field of 2 Tesla and employing a Si (220) double-crystal monochromator and a vertically-collimating pre-monochromator mirror. The incident and transmitted X-ray intensities were monitored using

nitrogen-filled ionization chambers, and X-ray absorption was measured as the copper $K\alpha$ fluorescence using a Lytle detector.

Nickel filters were placed between the cryostat and detector to reduce scattered X-ray not associated with Cu fluorescence. During data collection, samples were maintained at a temperature of ~ 10 K using an Oxford instruments liquid helium flow cryostat. XAS spectra were measured using 10 eV steps in the pre-edge region (8750–8960 eV), 0.35 eV steps in the edge region (8960–9010 eV) and 0.05 \AA^{-1} increments in the EXAFS region (to $k = 13 \text{ \AA}^{-1}$). Three to four scans were accumulated, and the energy was calibrated by reference to the absorption of a standard copper metal foil measured simultaneously with each scan, assuming a lowest energy inflection point of the copper foil to be 8980.3 eV. The cryostat was moved after each scan to prevent photoreduction and to have the X-ray beam focused on a new area of the sample holder where the sample was not exposed previously to radiation.

The extended x-ray absorption fine structure (EXAFS) oscillations (k) were quantitatively analyzed by curve fitting using the EXAFSPAK suite.⁶⁰ Ab initio theoretical phase and amplitude functions were calculated using the program FEFF version 8.2.⁶¹

2.3.18 Molecular Modelling

The initial model of HSA at N-terminus site bound to Cu^{2+} was based on the published crystal structure of Cu bound DAHK (CCDC- 809109) was determined by the crystal structures. The N-terminus site was imported into HyperchemTM7.5 (Hypercube, Inc.,) and previously optimized SAP conformation GdL1 complex used in all coordination. Geometry optimization was performed based on EXAFS experimental bond lengths of N and O coordinated to the Cu centers. All optimizations were carried

out using the Polak-Ribiere algorithm until the termination condition of 0.1 Kcal/ (\AA mol) RMS gradient was met.

2.3.19 In-vitro Phantom MR images

In vitro phantom, MR images were obtained for GdL1 in 50 mM Tris-saline buffer at pH 7.4 and 0.1 mM GdL1 with and without 600 μ M HSA with 25, 50, 75 and 100 μ M of Cu²⁺ loaded in 96-well plate. Image T₁ values were obtained at 400 MHz (9.4 T) in Varian MRI scanner microimaging system using a spin-echo multislice (SEMS) sequence. Image analyzed were carried out using ImageJ software provided by the National Institute of Health, USA.

2.3.20 In-vivo Imaging

All animal experiments were performed by guidelines set by the UT Southwestern Institutional Animal Care and Use Committee (IACUC). Male C57bl/6 mice were anesthetized with isoflurane. One group of mice (n=3) were injected with 5 mg/kg of ATN- 224, 2 hrs. before the injection of GdL1. Once the animals were secured inside a 38-mm volume coil, the liver was positioned in the center of the 4.7 T Varian MRI scanner. Two 3D T₁-weighted gradient echo pre-injection scans were obtained (TE/TR = 1.57/3.11 ms, NEX8, Matrix = 128 \times 128 \times 128). 0.1 mmol/kg of GdL1/Gadavist were injected to the mice after with and without injection of ATN-224 in a group of n=3, and post-injection scans were obtained. Consecutive 3D T₁-weighted scans were obtained sequentially to monitor signal enhancement in the liver. Identification of the liver was accomplished by locating the tissues surrounded by the spleen, stomach, and heart. The images were quantified and analyzed using ImageJ (National Institutes of Health, Bethesda, MD). The signal intensities from ROIs of the liver and kidney were measured separately and averaged at 6, 9, 12, 15, and 18 minutes. The values were normalized to the signal intensity obtained from mouse

back muscle. Contrast enhancement was calculated using the formula($\frac{\text{Signal post-injection}}{\text{Signal pre-injection}} - 1$)
 $\times 100\%$. Statistical analysis was performed by comparing the mean values using a two-tailed *t*-test. Statistical difference was evaluated using the *t*-statistic and p-values at a 95% confidence level.

2.3.21 Bio-distribution analysis of metal by ICP-MS

Mice were treated with GdL1 and ATN-224 similar to the *in vivo* imaging experiments. After 5 min of injection of GdL1, the mice were heavily anesthetized, and tissues were isolated. The tissues were homogenized and completely lysed in 2 ml freshly made aqua Regia for 24 hrs. The samples were then heated at 120°C in an oil bath until complete evaporation of aqua Regia. The residue was re-dissolved in 0.5M HCl and sonicated for 30 min. The samples were centrifuged at 4000 g for 5 min to eliminate any residue. The resultant samples were diluted with 4% HNO₃ and analyzed by ICP-MS.

2.4. Results and Discussion

2.4.1 Design and Synthesis Methods

The structure of the Cu²⁺-responsive agent reported here consists of a GdDO3A with a bis (benzoic acid)methylamine side-chain as a potential chelator for Cu²⁺. This design was motivated by our previous MR-responsive Zn²⁺ sensor scaffold where the ion of interest initiates formation of a ternary complex between the agent and HSA.^{40,41} Although Cu²⁺ has a preference for nitrogen donor atoms, the coordination rigidity provided by the bis(benzoic acid)methylamine could potentially favor coordination by geometrical stabilization of tetragonal or square pyramidal structures typical of Cu²⁺.^{60,61} This structural feature precludes the possibility of binding with the more abundant biological ions like Ca²⁺ and Mg²⁺. To evaluate the impact of the repositioning the

carboxylate groups on the aromatic side-chain and lowering the charge on the carboxylate groups, GdL2 and GdL3 were also synthesized and compared. The synthetic details of all three contrast agents are outlined in experimental section.

2.4.2. Water proton relaxivity measurements in the presence of various metal ions

The longitudinal relaxivity (r_1) of GdL1 ($4.7 \pm 0.1 \text{ mM}^{-1}\text{s}^{-1}$) was unchanged upon addition of Ca^{2+} , Mg^{2+} or Fe^{3+} ions (Figure 2.7 and Figure 2.8). But addition of Zn^{2+} increased the r_1 value to $5.3 \text{ mM}^{-1}\text{s}^{-1}$ (a 12% increase) while addition of Cu^{2+} increased the r_1 to $6.7 \text{ mM}^{-1}\text{s}^{-1}$ (a 47% increase). In all cases, the background relaxivity due to the weak paramagnetism of Cu^{2+} and Fe^{3+} were subtracted from the r_1 values shown in Figure 2.7 and reported in Table 2.1.⁶² These data suggest that GdL1 have some selectivity for Cu^{2+} over Zn^{2+} in agreement with the Irving-William series and Pearson's Hard-Soft Acid Base (HSAB) theories.⁶³ Even though the origin of this r_1 enhancement is unclear from these data alone, one possibility is that the linker side-arm with the anionic carboxyl groups on the bis-benzoic acid motif could interact with a single exchanging inner-sphere water molecule on the Gd^{3+} ion, and this interaction is reduced when Cu^{2+} binds to GdL1. This could in principle alter the water exchange rate in this system and result in the changes in r_1 . A second contributing factor might be that GdL1 experiences relatively slower molecular rotation (τ_R) upon binding to Cu^{2+} , and this could result in a slight increase r_1 relaxivity. These two hypotheses were examined in more detail below. The binding stoichiometry between GdL1 and Cu^{2+} was determined to be 1:1 as reported by the method of continuous variations and by an inflection point⁶⁴ in the relaxivity data (Figure 2.9). This stoichiometry was assumed in all calculations of K_d . The increase in r_1 of GdL2 and GdL3 were considerably lower upon addition

of Cu^{2+} (Figure 2.10), suggesting that either the binding affinity of GdL2 and GdL3 are lower for Cu^{2+} or the resulting GdLx- Cu^{2+} complexes have quite different water exchange properties.

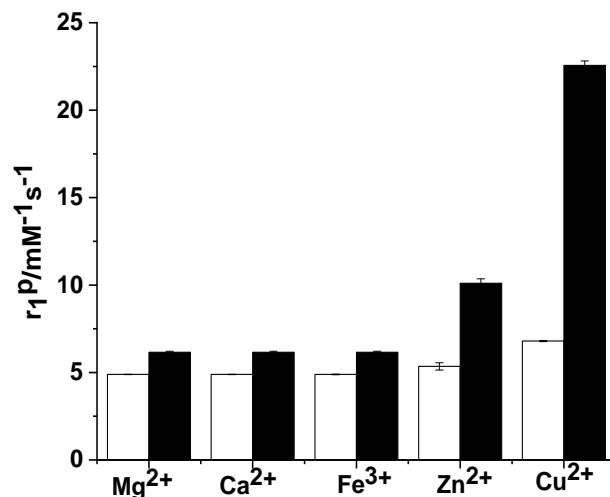


Figure 2.7. The relaxivity (r_1) of GdL1 in the presence of various $\text{M}^{2+} \pm \text{HSA}$. The white bars reflect r_1 after addition of 0.5 mM Mg^{2+} , Ca^{2+} , Fe^{3+} , Zn^{2+} or Cu^{2+} to 0.5 mM solution of GdL1. The black bars reflect r_1 after subsequent addition of 0.6 mM HSA to the GdL1- M^{2+} solutions. The r_1 values were determined in 0.1 M MOPS buffer (pH 7.4) at 37°C and 20 MHz.

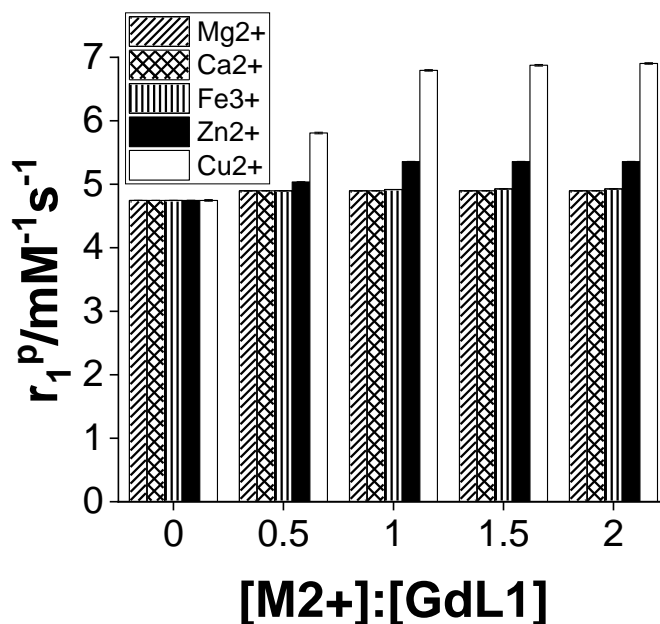


Figure 2.8. Relaxivity response of 0.5 mM GdL1 to various metal ions in 0.1 M MOPS buffer at 20 MHz at 37°C.

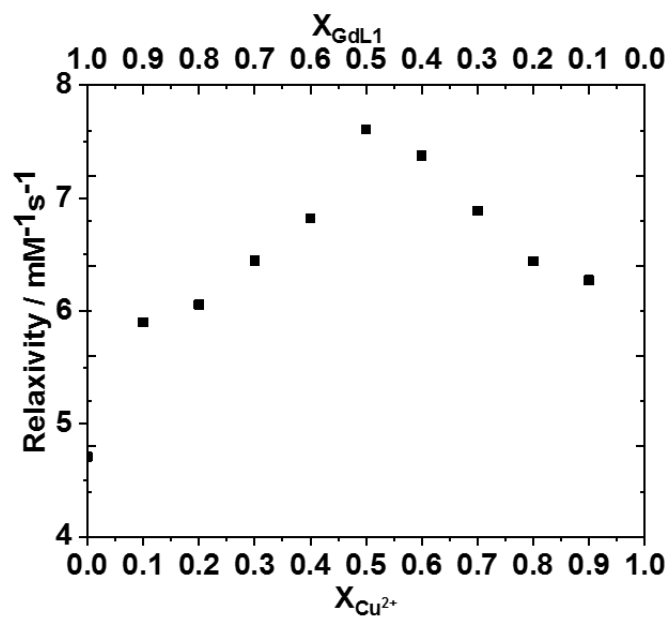


Figure 2.9. Job's plot for GdL1 and Cu²⁺.

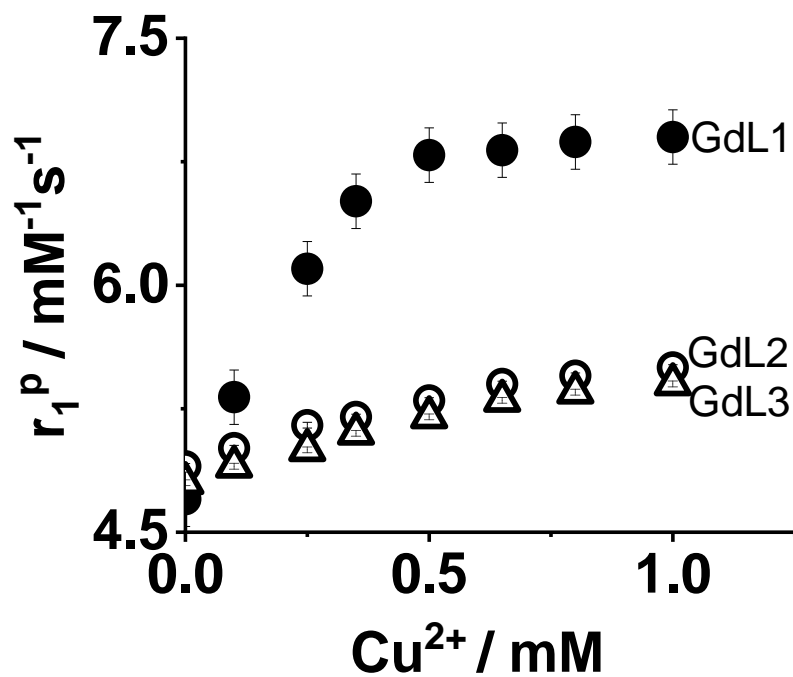


Figure 2.10. The r₁ relaxivity of GdL1-3 as a function of added Cu²⁺ ions. The concentration of GdL1-3 was 0.5 mM in 0.1M MOPS buffer (pH 7.4). The data were collected at 20 MHz and 37°C.

2.4.3. Binding experiments in the absence of HSA (GdLx-Cu²⁺)

The equilibrium dissociation constants (K_d) between the three GdLx complexes and Cu²⁺ were determined by fluorescence spectroscopy by performing titrations in which Cu²⁺ was added to a buffered solution containing GdLx. Addition of Cu²⁺ results in quenching of the intrinsic fluorescence of the benzoic acid moieties in GdLx (Figure 2.11).^{65, 66} These binding curves were fit to a 1:1 binding model to give the K_d values reported in Table 2.1. These data indicate that GdL1 has the highest affinity for Cu²⁺ ($84 \pm 10 \mu\text{M}$), followed by GdL3 ($352 \pm 9 \mu\text{M}$) and GdL2 ($895 \pm 32 \mu\text{M}$). This suggests that the position of the carboxyl groups (meta *versus* para) and charge are both important for Cu²⁺ binding.

Table 2.1. Relaxivity and K_d values for GdL1-3 in 0.1M MOPS buffer (pH 7.4) at 37°C.

| GdLx | r_1 (mM ⁻¹ s ⁻¹) | | | | r_1 (mM ⁻¹ s ⁻¹) | | | K_d (GdL-Cu ²⁺ -HSA) (μM) **** |
|-------------|---|-----------------------------|-----|--------------|---|--|------|---|
| | No Cu ²⁺ | 1 eq. Cu ²⁺ * | | | 0.6 mM HSA | 0.6 mM HSA with 1 eq. of Cu ²⁺ ** | | |
| GdL1 | 4.7 \pm 0.1 | 6.7 \pm 0.1 | 47% | 84 \pm 10 | 6.1 \pm 0.1 | 22.6 \pm 0.2 | 270% | 45 \pm 3.1 |
| GdL2 | 4.9 \pm 0.2 | 5.5 \pm 0.1 | 12% | 895 \pm 32 | 6.5 \pm 0.2 | 14.5 \pm 0.1 | 123% | 59 \pm 5 |
| GdL3 | 4.8 \pm 0.1 | 5.4 \pm 0.2 | 12% | 352 \pm 9 | 6.3 \pm 0.2 | 12.0 \pm 0.2 | 90% | 60 \pm 10 |

* r_1 of Cu²⁺ in 0.1M MOPS buffer is 0.739 mM⁻¹s⁻¹.

** r_1 of Cu²⁺ with HSA in 0.1M MOPS Buffer 5.10 mM⁻¹s⁻¹. r_1 of HSA with GdL1 in 0.1M MOPS Buffer 0.739 mM⁻¹s⁻¹.

*** K_d (GdL-Cu²⁺) was determined by fluorescence experiments.

**** K_d (GdL-Cu²⁺-HSA) was determined by Proton Relaxation Enhancement experiments.

***** All the relaxivity measurements were measured at 20MHz.

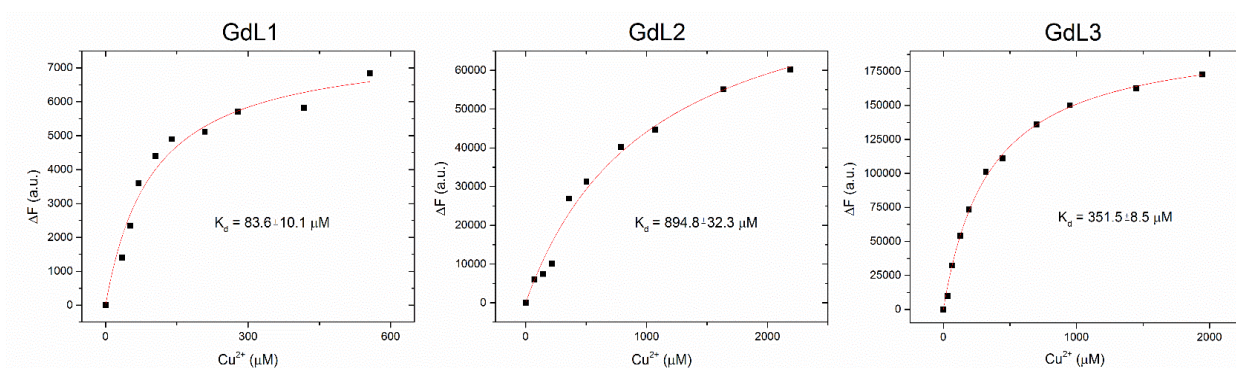


Figure 2.11. Experimental and fitted titration curves for change in fluorescence intensity upon titration with Cu^{2+} at 25°C for GdL1, GdL2, and GdL3.

2.4.4. Water proton relaxivity measurements in the presence of various metal ions and HSA

HSA, the most abundant protein in serum ($\sim 600 \mu\text{M}$), plays a key role in the transport of metal ions, fatty acids, and other hydrophobic molecules including many drugs. HSA has two Cu^{2+} binding sites, the N-terminal site (NTS) and multi-metal binding site (MBS).^{67,68} It was reported that Cu^{2+} has a significantly higher affinity for the NTS site ($\sim 1 \text{ pM}$)⁶⁵ than the MBS site ($\sim 10 \text{ nM}$)⁶⁹. Thus, the NTS site is considered to be the only site in HSA to occupy Cu^{2+} since the concentration of HSA is much higher than the biological concentration of free Cu^{2+} ions.^{67,70} We recently demonstrated that analogous Gd-based MR contrast agents responded to sudden increases in free Zn^{2+} ions from pancreatic β -cells³⁹ and epithelial prostate cells stimulated by an increase in plasma glucose.³⁸ This functional response was shown to reflect formation of a ternary GdL-Zn-HSA complex at the MBS site A.⁴⁰ This previous data suggested that perhaps Cu^{2+} could also be detected *in vivo* in those situations where excess free Cu^{2+} ions in extracellular spaces might be available for binding to a contrast agent. This motivated further relaxometric studies to determine the magnetic contributions of all the GdLx with Cu^{2+} in the presence of physiological levels of HSA. As summarized in Table 2.1, the r_1 values for all three complexes increase slightly in the

presence of HSA alone (likely reflecting a slight increase in viscosity) but increase substantially after the addition of Cu^{2+} ions. This suggests that the GdLx complexes experience slower molecular rotation by the formation of a GdLx-Cu-HSA ternary complex. This is particularly true for GdL₁ where r_1 increases from 6.1 ± 0.1 to $22.6 \pm 0.2 \text{ mM}^{-1}\text{s}^{-1}$ (a 270% increase). As shown in Figure 2.7 (and Figures 2.12, 2.13), Mg^{2+} , Ca^{2+} , Fe^{3+} do not result in an increase in r_1 in the presence of HSA while Zn^{2+} ions do to a lesser extent, about 2-fold lower than the increase in r_1 induced by Cu^{2+} .

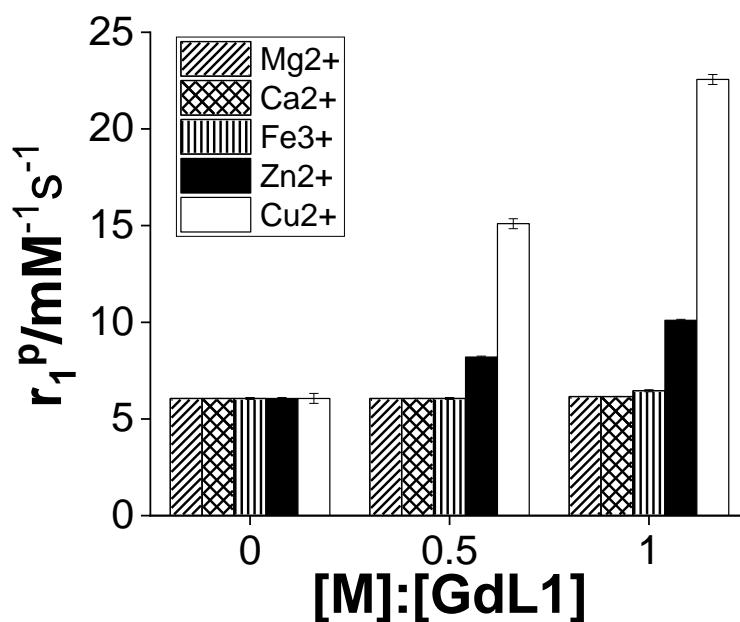


Figure 2.12. The r_1 relaxivity of 0.5 mM GdL1 after addition of Mg^{2+} , Ca^{2+} , Fe^{3+} , Zn^{2+} or Cu^{2+} in 0.1M MOPS buffer (pH 7.4) and 600 μM HSA at 37°C and 20MHz.

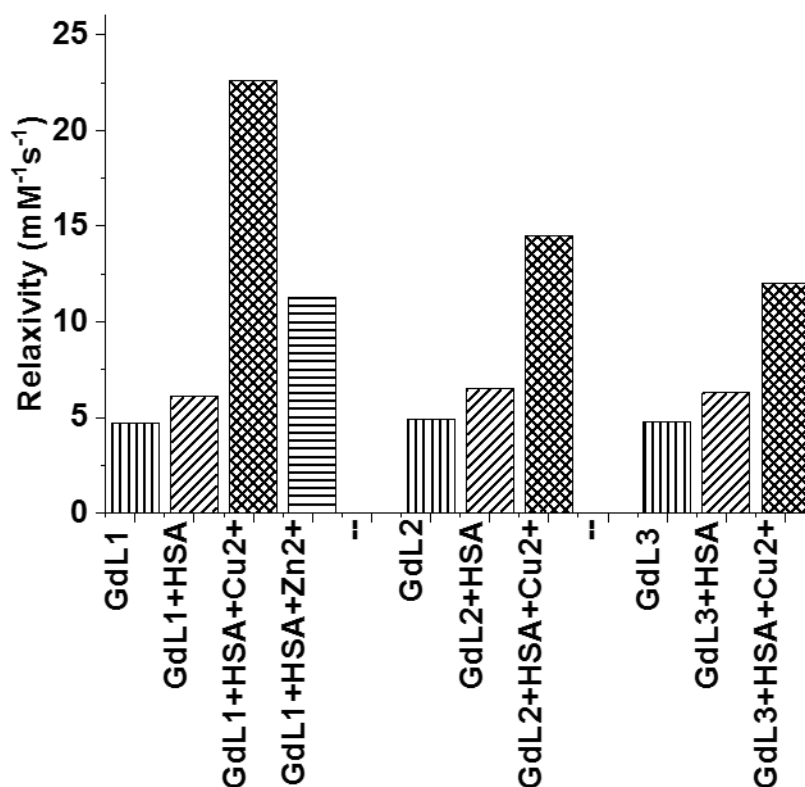


Figure 2.13. Relaxivity response of 0.5 mM GdL1-3 to 1 equivalents of Zn²⁺ and Cu²⁺ in 0.1M MOPS buffer (pH 7.4) with 600 μ M HSA at 37°C at a proton Larmor frequency of 20MHz.

2.4.5. Binding experiments in the presence of HSA

To examine these binding interactions further, additional proton relaxation enhancement (PRE) titrations were carried out to quantitatively evaluate the binding constants for each GdL_x complex with HSA in the presence of 1 molar equivalent of Cu²⁺. A fitting of those data (Figure 2.14 and Table 2.2) to a 1:1 binding model gave the K_d values reported in Table 2.1. GdL1 showed the highest binding affinity to HSA-Cu²⁺ ($K_d = 45 \pm 3.1 \mu$ M) while the binding affinities of GdL2 and GdL3 were surprisingly weaker only by ~30%. This demonstrates that the large differences in binding affinity between the different GdL_x and Cu²⁺ are leveled upon formation of the ternary GdL_x-Cu²⁺-HSA complexes. These data alone suggest that HSA plays a significant role in

stabilizing the binding interactions between GdL_x and Cu²⁺ ions. To confirm the formation of the LnL_x-Cu²⁺-HSA ternary complex, a sample of LaL₁ (a diamagnetic analog), Cu²⁺ and HSA (from an EPR experiment, see below) were passed through a size exclusion chromatography column, and the eluent peaks were separately analyzed for Cu and La by ICP-MS.

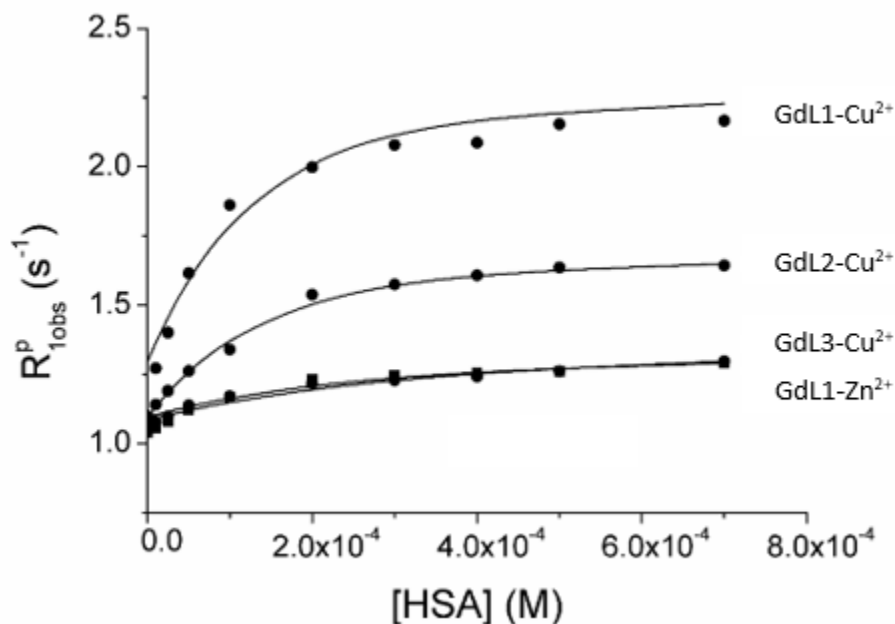


Figure 2.14. Proton relaxation enhancement of GdL-Cu²⁺ complexes with increasing concentration of HSA. All measurements were performed at 20 MHz and 310 K in 0.1 M MOPS buffer at pH 7.4.

Table 2.2. Best-fit parameters Relaxivity and K_d value for GdL1-3 in 0.1 M MOPS buffer (pH 7.4) at 37°C.

| Gd-Complex | GdL1 | | GdL2 | GdL3 |
|---|------------------|------------------|------------------|------------------|
| Metal | Cu ²⁺ | Zn ²⁺ | Cu ²⁺ | Cu ²⁺ |
| K _D (μM) | 44.0 ± 3 | 110 ± 20 | 59 ± 5 | 60 ± 10 |
| R _{1bound} (mM ⁻¹ · s ⁻¹) | 22 ± 0.5 | 11 ± 0.9 | 17 ± 0.6 | 12.9 ± 0.8 |

Those results (Figure 2.15 and Table 2.3) showed that ~63% of the total La eluted from the column in the form of a ternary $\text{LaL}_1\text{-Cu}^{2+}\text{-HSA}$ complex, confirming the formation of a stable Cu mediated ternary complex. The most widely studied high affinity Cu^{2+} binding site in HSA is at the amino terminus (NTS) while the second weaker binding site (MBS) is located at the interface of domain IB and IIA.⁶⁷⁻⁶⁹ Some recent evidence showed that metal ion binding at the MBS site is affected by binding of drugs and fatty acids at drug site 2 in HSA.⁶⁹⁻⁷¹ Therefore, an experiment was performed to examine whether warfarin or dansylglycine disrupt the $\text{GdL}_1\text{-Cu}^{2+}\text{-HSA}$ ternary complex. These molecules bind specifically to the two different drug binding sites in HSA, warfarin to drug site 1 in domain IIA and dansylglycine to drug site 2 in subdomain IIIA.⁷¹⁻⁷⁵

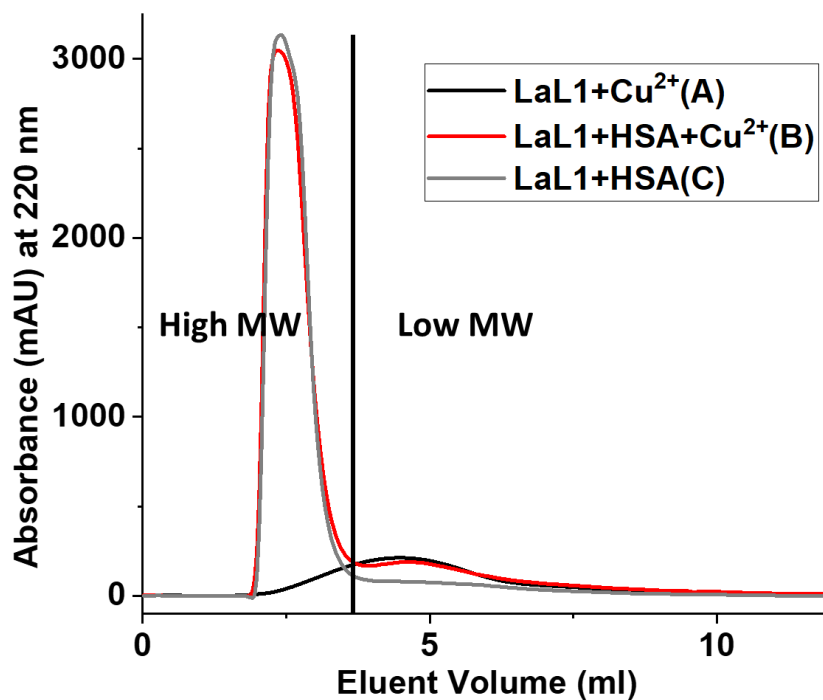


Figure 2.15. Chromatogram for of size exclusion chromatography

Table 2.3. Lanthanum metal ion concertation in high-molecular-weight fraction and low-molecular-weight fraction.

| Sample | La ³⁺ ion concentration in High MW fraction (μM) | La ³⁺ ion concentration in Low MW fraction (μM) |
|---------------------------|---|--|
| LaL1+Cu ²⁺ | 10 | 84 |
| LaL1+HSA+Cu ²⁺ | 63 | 28 |
| LaL1+HSA | 14 | 82 |

A competition binding study was performed by titrating a solution of either warfarin or dansylglycine, HSA, GdL1, Cu²⁺ with an identical solution lacking GdL1. As shown in Figure 2.16, only dansylglycine was displaced from its binding site when GdL1 was added to the mixture. This suggests that the ternary GdL1-Cu²⁺-HSA complex either directly displaces dansylglycine from its binding site in subdomain IIIA or more likely initiates a structural change that weakens the binding affinity between HSA and dansylglycine. A fit of the dansylglycine displacement results using the published binding constant for HSA-dansylglycine (2.5 μM)⁷⁶ gave a binding constant for the ternary GdL1-Cu²⁺-HSA complex of 40 ± 1 μM, a value similar to the K_d value obtained in the PRE-experiments.

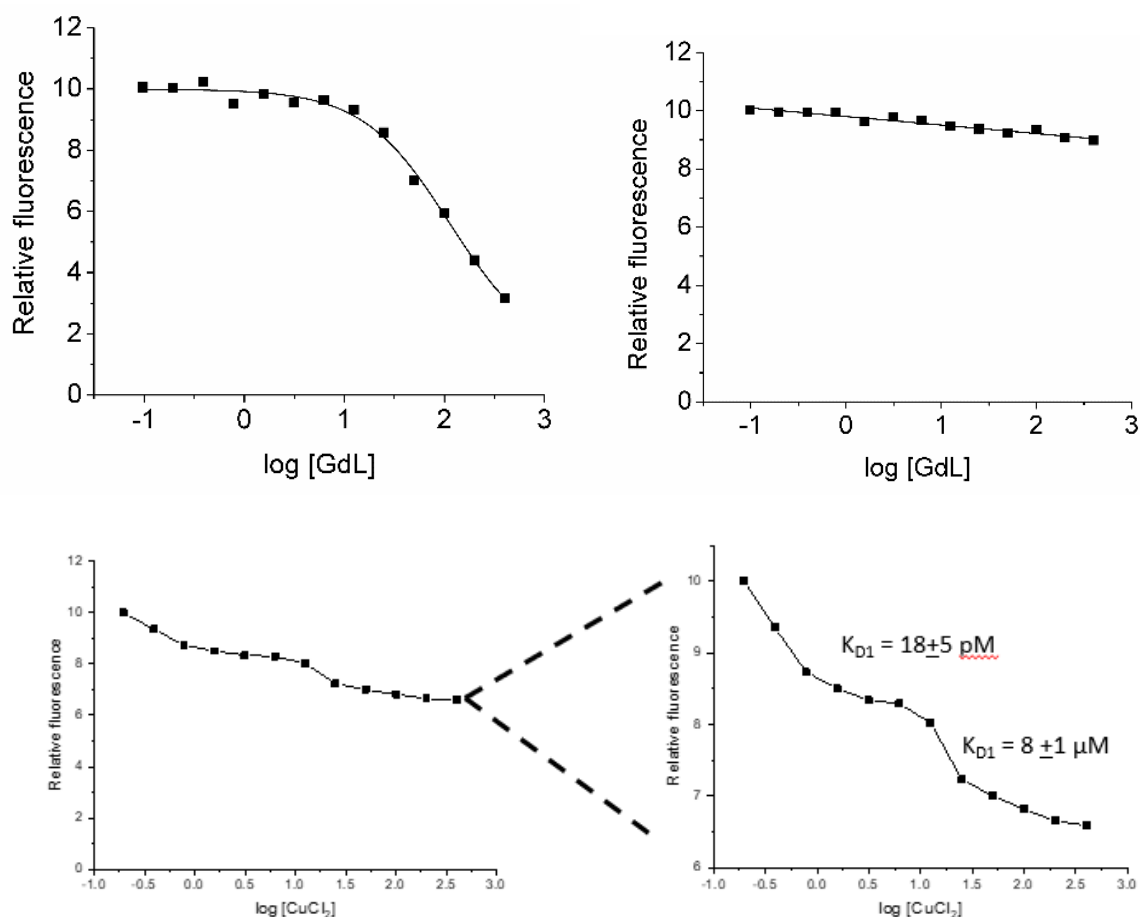


Figure 2.16. Competition binding curves are showing that dansylglycine (drug site 2) (top left) is displaced by GdL1 while warfarin (drug site 1) (top right) is not. Bottom curves represent the competition titration with CuCl₂ instead of GdL1.

2.4.6 Water exchange rates

The longitudinal relaxivity (r_1) of Gd-complexes such as this is governed by several parameters including the water exchange rate (k_{ex}), the number of inner-sphere water molecules on Gd³⁺ (q), and rotational tumbling of the molecule (τ_R) (see equations in supporting information). A simple and direct way to measure the water exchange rate is by measuring the temperature-dependent T_{2s} by ¹⁷O NMR (Figure 2.17). A fit of those T_2 data to theory gave the water exchange rates reported

in Table 2.5. Both the GdL1 and GdL2 had similar water exchange rates (k_{ex}), somewhat slower than that reported for GdDOTA ($k_{ex} = \sim 3 \times 10^6 \text{ s}^{-1}$) as expected for monoamide derivatives. The number of the inner-sphere bound waters (q) coordinated to Gd^{3+} in these complexes was also calculated $q \sim 1.0 \pm 0.2$ for all complexes by the Evans method.⁷⁷⁻⁸¹

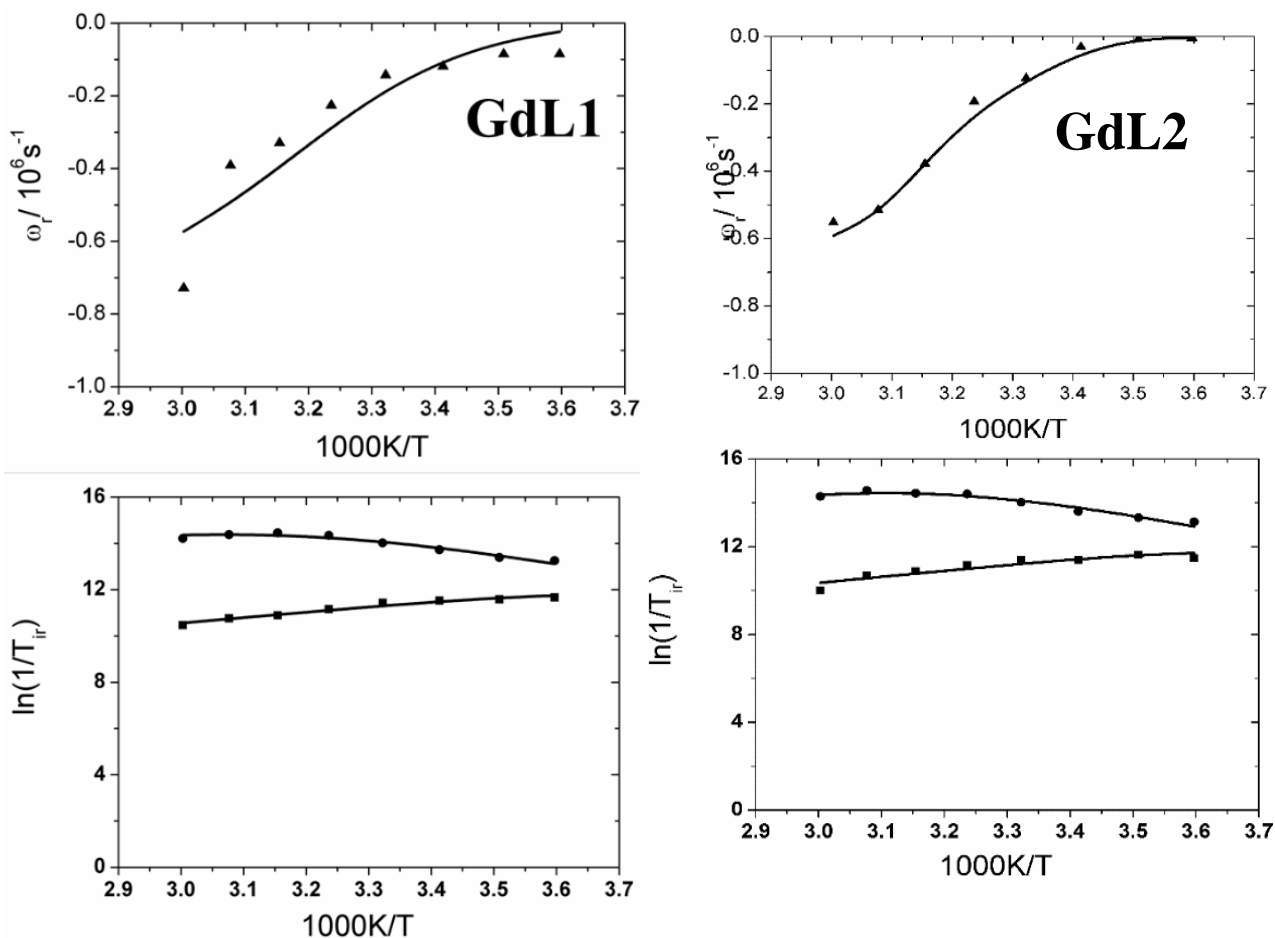


Figure 2.17. Temperature dependence of the reduced longitudinal (■) and transverse (▲) ^{17}O relaxation rates and reduced chemical shifts (●) of the GdL1(25.4 mM) and GdL2 (25.1 mM) in aqueous solution $B_0 = 9.4 \text{ T}$.

2.4.7 Kinetic inertness

The kinetic stability of a GdLx complex is also an important factor to consider when developing MRI probes. Previous studies reported that Cu^{2+} could displace Gd^{3+} from a complex by transmetalation.⁶⁹ This possibility was examined by challenging GdL1 with 3-molar equivalents of Cu^{2+} in 0.03 M phosphate buffer (pH =7.2). Under these conditions, if transmetallation occurred, any unchelated Gd^{3+} would then precipitate from the solution as an insoluble phosphate, a process that can be monitored by relaxometry. $R_{1\text{obs}}$ values measured over the time (Figure 2.18) show that the complexes are kinetically inert, even in the presence of 3-fold excess Cu^{2+} .⁸³ Additional LC-MS data showed that in the presence of 1 molar equivalent of Cu^{2+} no metal transmetallation was observed at room temperature after 7 days in MOPS buffer.

Table 2.4. Best-fit parameters obtained for GdL1 and GdL2 from analysis of ^{17}O NMR data.

| Parameters | GdL1 | GdL2 | $[\text{GdDOTA}(\text{H}_2\text{O})]^-$ |
|--|-------------|-------------|---|
| $r_{1\ 20\text{MHz}}^p [\text{mM}^{-1} \text{s}^{-1}]$ | 5.8±1 | 5.7±1 | 3.9 |
| $k_{\text{ex}}^{298} [10^6 \text{s}^{-1}]$ | 2.0±0.3 | 1.9±0.3 | 4.1 |
| $t_m [\text{ns}]$ | 497±1 | 526±1 | 243 |
| $\text{DH}^\ddagger [\text{kJ/mol}]$ | 40±5.0 | 45±7.0 | 49.8 |
| $E_R [\text{kJ/mol}]$ | <u>18.0</u> | <u>18.0</u> | 16.1 |

| | | | |
|----------------------------|-------------|-------------|------|
| t_{RO}^{298} [ps] | 530±10 | 497±10 | 77 |
| E_V [kJ/mol] | <u>1.0</u> | <u>1.0</u> | 1.0 |
| t_V^{298} [ps] | <u>3.4</u> | <u>3.4</u> | 11 |
| D^2 [$10^{20} s^{-2}$] | <u>0.55</u> | <u>0.55</u> | 0.16 |
| A/h [MHz/ 10^{-6}] | -3.9±0.3 | -3.9±0.2 | -3.7 |

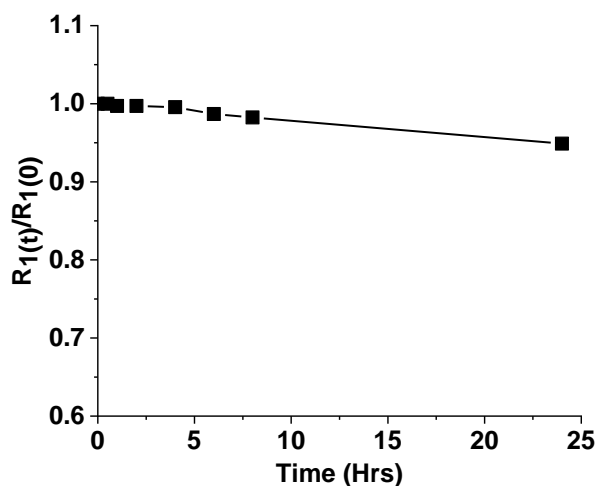


Figure 2.18. Relaxivity measurements of 1.5 mM GdL1 and 4.5 mM Cu^{2+} in 30 mM Phosphate buffer in 310 K at 20 MHz.

2.4.8 Identifying the Cu^{2+} donor atoms on GdL1

To learn more about the binding interactions between Cu^{2+} and GdL1, high-resolution 1H NMR spectra of LaL1 (the diamagnetic analog) were recorded in D_2O before and after addition of $CuCl_2$. The 1H NMR signals corresponding to the phenyl ring of benzoic acid (H_a , H_b , H_c , and H_d) and the

H_e and H_f methylene protons in the spectrum of LaL₁ broadened and shifted upon addition of Cu^{2+} (Figure 2.19). This supports the participation of the carboxylates and the tertiary amine of the bis(benzoic acid)methylamine moiety in Cu^{2+} coordination.⁸⁴⁻⁸⁶ The X-band EPR spectrum of the LaL₁- Cu^{2+} complex exhibited an unusual axial spectrum (devoid of well-defined hyperfine features and a $g_{\perp} \cong 1.99$) both in the absence and presence of HSA (Figure 2.20). The g_{\perp} values shown by these spectra significantly deviated from the typical values of an axial EPR spectrum for Type-2 Cu^{2+} complex.⁶⁷ This suggests that the Cu^{2+} center in both complexes are electron poor, likely due to the strong electron withdrawing effect of the lanthanum ion in the complex. In comparison, the X-band EPR spectrum of HSA- Cu^{2+} exhibited a typical Type-2 square pyramidal geometry very similar to previously reported EPR spectra in the literature.⁸⁷ However, the broadened hyperfine features of the Cu^{2+} EPR spectra after addition of LaL₁ precluded a detailed structural analysis of the copper center.

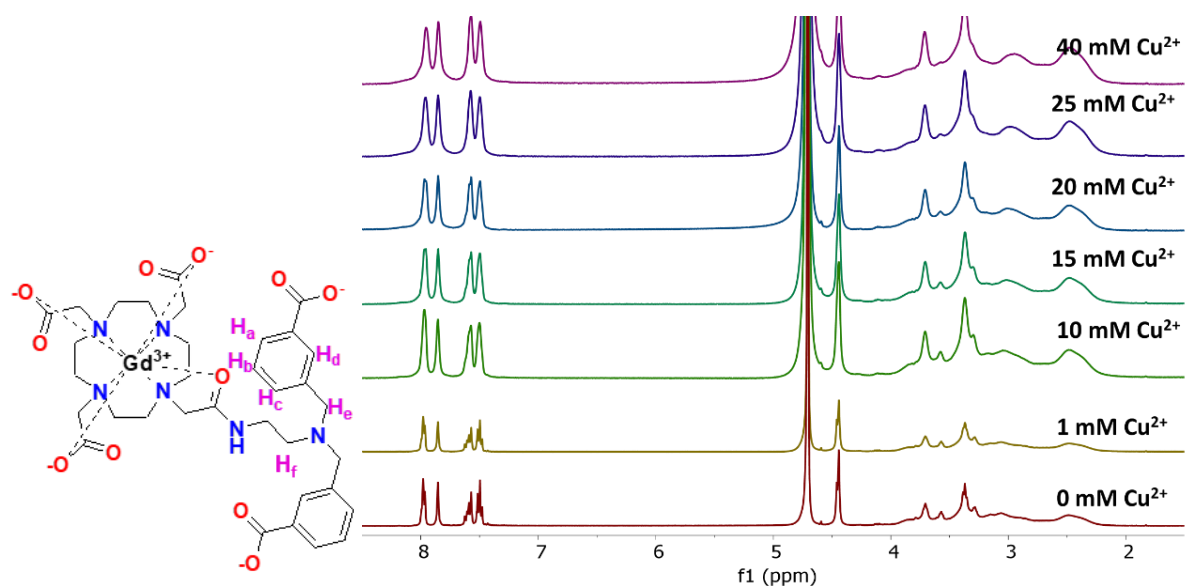


Figure 2.19. 1H NMR titration spectra of 20 mM LaL₁ in the presence of various concentrations of Cu^{2+} at 37°C in D_2O .

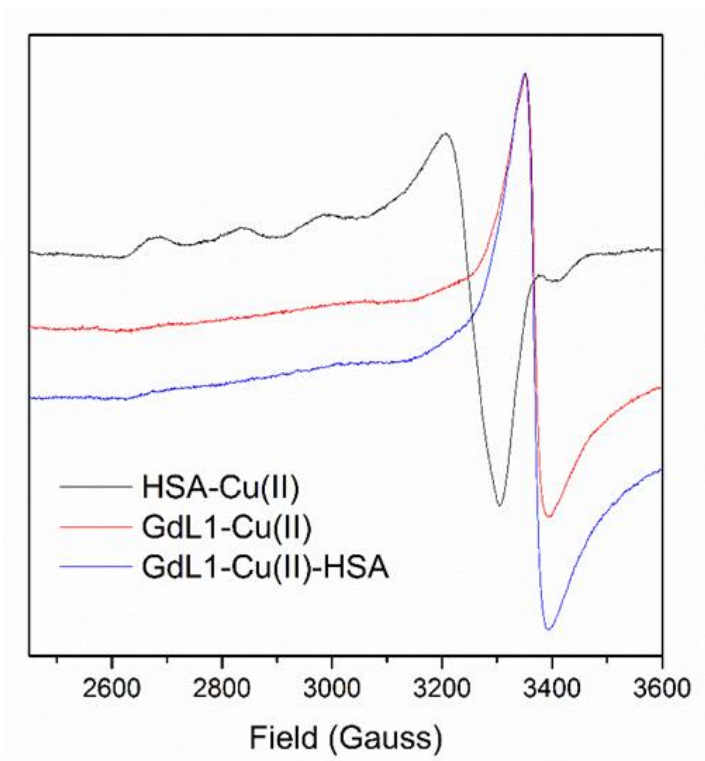


Figure 2.20. X-Band EPR Spectra of 250 μ M Cu²⁺ with 250uM LaL1 in 250uM HSA in 10mM MOPS buffer at pH 7.2 (2,500–3,500 G, 9.3 GHz, 30K)

2.4.9 XAS studies

Copper k-edge X-ray absorption spectroscopy (XAS) studies were also performed to identify the Cu²⁺ donor atoms in GdL1-Cu²⁺ and GdL1-Cu²⁺-HSA. The XANES spectrum of GdL1-Cu²⁺ (Figure 2.21) is characterized by an intense absorption feature at 8987–8988eV with broad low energy tail in the region below 8985eV (normalized absorption of approx. 0.5 at 8988 eV) arising from a 1s \rightarrow 4p transition characteristic of Cu²⁺ complexes. The presence of the first major inflection point at 8986eV and the absence of lower energy features (normalized absorption 0.15 at 8984 eV and first inflection point 8984 eV) is typical of classic tetragonal Cu²⁺ complexes with nitrogen and oxygen ligands. The complex also presents a weak 8979eV peak (more visible in the

first derivative spectra) corresponding to the $1s \rightarrow 3d$ transition possibly reflecting a less centrosymmetric nature of the center and thus a significant degree of distortion from planarity.⁸⁹ The XANES spectrum of GdL1-Cu²⁺-HSA is nearly identical to the spectrum of Cu²⁺-HSA, suggesting a very similar coordination environment in the two complexes. The spectra are characterized by an intense absorption feature at 8987–8988 eV arising from a $1s \rightarrow 4p$ transition. Additional features for the Cu²⁺ site include a lower-energy feature with normalized absorption of approximately 0.25 at 8984 eV, and the first inflection point determined in the first derivative spectrum at 8982 eV, about ~ 1 eV higher than the one observed in Cu⁺ complexes. Possible photoreduction of Cu²⁺ was prevented experimentally by collecting the spectra at different locations in the frozen sample in each scan. Also, the XANES spectra were quite similar to the one observed for the Cu²⁺-DAHK peptide complex representing the N-terminal Cu²⁺ binding site in HSA, thus supporting the same coordination environment in the full-length protein.⁶⁵ Additional information of coordination environment and ligand metal distances were obtained by copper K-edge extended X-ray absorption fine structure (EXAFS). The experimental copper EXAFS spectra are presented in Figure 2.22 together with best fits, and the corresponding EXAFS Fourier transforms. The spectrum of GdL1-Cu²⁺ could be fitted with 2 ligand shells indicative of a Cu complex coordinated by 3 N/O ligands at 1.99 Å and a N/O ligand at 2.51 Å (Table 2.5). The XANES and EXAFS results are consistent with the NMR analysis suggesting the presence of a distorted tetragonal complex in which 3 ligands arise from the carboxylates and the tertiary amine of the bis(benzoic acid)methylamine moiety and possible additional coordination by a solvent water molecule to the Cu²⁺ ion.

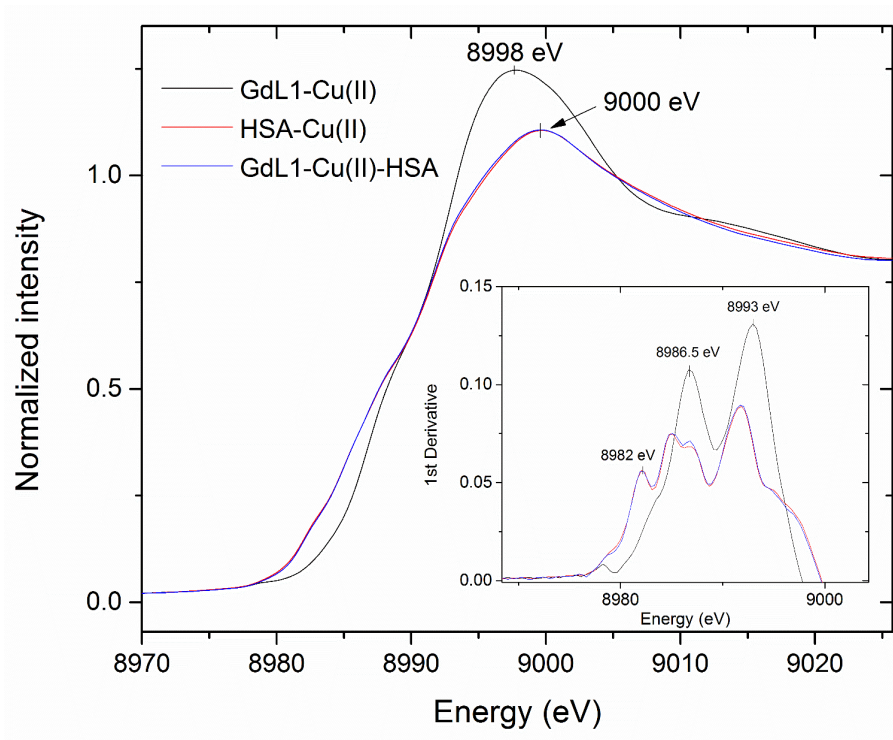


Figure 2.21. XANES spectra for GdL1 in the presence of Cu^{2+} and HSA.

In the HSA-Cu^{2+} complex, the EXAFS data were best fit with 3 coordinating shells around Cu^{2+} with 3 Cu-O/N bonds at 1.99 Å and an additional (likely equatorial) N/O bond at 2.28 Å. In addition, a third shell corresponding to a N/O ligand at 2.51 Å was obtained in the fit suggesting the presence of an axial ligand. This analysis was in agreement with a previously reported square pyramidal Cu^{2+} -HSA coordination at the N-terminal site (also known as ATCUN) with high-affinity for Cu^{2+} .⁵² Copper is coordinated to four nitrogen donors in the NTS site consisting of Asp, Ala, His amide nitrogen atoms and the His side chain in an equatorial position and a water molecule or N-terminal amine nitrogen in the axial position.^{65,74} For the GdL1- Cu^{2+} -HSA ternary

complex, the EXAFS data could be best fitted with 3 or 4 N/O ligands (resulting in similar F-values) at 1.96 Å and 2 additional N/O ligands at 2.33 Å and 2.89 Å. The analysis predicts the presence of a distorted square pyramidal/ octahedral coordination around the Cu^{2+} in the ternary complex with 4 equatorial ligands with short bond distances and 1 or 2 axial ligands with longer bond distance (Table 2.5).

This coordination anticipates the replacement of loosely bound axial ligand in Cu^{2+} -HSA complex by the chelating sites in bis(benzoic acid)methylamine moiety of GdL1. It should be noted that the bond distances for distorted square pyramidal Cu^{2+} -HSA complex are distinctly different from the bond distances of the distorted square pyramidal ternary complex. Despite being difficult to unambiguously distinguish the coordination 1 or 2 axial ligands by XAS, the EXAFS analysis confirms small differences in the coordination shells between GdL1- Cu^{2+} -HSA and HSA- Cu^{2+} . This distorted octahedral or square pyramidal coordination of Cu^{2+} in ternary complex compared to the distorted square pyramidal coordination of Cu^{2+} -HSA supports the formation of a copper-mediated complex between HSA and GdL1.

This coordination anticipates the replacement of loosely bound axial ligand in Cu^{2+} -HSA complex by the chelating sites in bis(benzoic acid)methylamine moiety of GdL1. It should be noted that the bond distances for distorted square pyramidal Cu^{2+} -HSA complex are distinctly different from the bond distances of the distorted square pyramidal ternary complex. Despite being difficult to unambiguously distinguish the coordination 1 or 2 axial ligands by XAS, the EXAFS analysis confirms small differences in the coordination shells between GdL1- Cu^{2+} -HSA and HSA- Cu^{2+} . This distorted octahedral or square pyramidal coordination of Cu^{2+} in ternary complex compared

to the distorted square pyramidal coordination of Cu²⁺-HSA supports the formation of a copper-mediated complex between HSA and GdL1.

Table 2.5. Structural and coordination parameters obtained from fitting Cu K-edge EXAFS. (N- Coordination Number, R -interatomic distance, σ^2 - Debye-walker factor)

| Complex | N | bond | R (Å) | $\sigma^2(\text{\AA}^2)$ | F-factor |
|-----------------|---|--------|----------|--------------------------|----------|
| GdL1-Cu(II) | 3 | Cu-N/O | 1.994(3) | 0.0008 | 0.488 |
| | 1 | Cu-N/O | 2.51(1) | 0.0001 | |
| Cu(II)-HSA | 3 | Cu-N/O | 1.991(2) | 0.0016 | 0.398 |
| | 1 | Cu-N/O | 2.278(7) | 0.0013 | |
| | 1 | Cu-N/O | 2.515(7) | 0.0008 | |
| GdL1-Cu(II)-HSA | 3 | Cu-N/O | 1.954(6) | 0.0054 | 0.576 |
| | 1 | Cu-N/O | 2.33(1) | 0.0037 | |
| | 1 | Cu-N/O | 2.86(1) | 0.0001 | |
| GdL1-Cu(II)-HSA | 4 | Cu-N/O | 1.965(6) | 0.0054 | 0.587 |
| | 1 | Cu-N/O | 2.31(2) | 0.0037 | |
| | 1 | Cu-N/O | 2.87(1) | 0.0001 | |

Coordination numbers are indicated by N , interatomic distances R are given in Å (the values in parentheses are the estimated standard deviations), Debye–Waller factors σ^2 (the mean-square deviations in interatomic distance) in Å², and the fit-error function F is defined by $F = [\sum k^6(\chi(k)_{\text{calcd}} - \chi(k)_{\text{exp}})^2 / \sum k^6(\chi(k)_{\text{exp}})^2]^{1/2}$ where $\chi(k)$ are the EXAFS oscillations and k is the photoelectron wavenumber.

This coordination anticipates the replacement of loosely bound axial ligand in Cu^{2+} -HSA complex by the chelating sites in bis(benzoic acid)methylamine moiety of GdL1. It should be noted that the bond distances for distorted square pyramidal Cu^{2+} -HSA complex are distinctly different from the bond distances of the distorted square pyramidal ternary complex. Despite being difficult to unambiguously distinguish the coordination 1 or 2 axial ligands by XAS, the EXAFS analysis confirms small differences in the coordination shells between GdL1- Cu^{2+} -HSA and HSA- Cu^{2+} . This distorted octahedral or square pyramidal coordination of Cu^{2+} in ternary complex compared to the distorted square pyramidal coordination of Cu^{2+} -HSA supports the formation of a copper-mediated complex between HSA and GdL1.

2.4.10 Molecular Modelling

Molecular models of the Cu centers in GdL1, HSA, and the ternary complex were generated based upon the coordination geometry and bond lengths for N and O atoms obtained from the EXAFS experimental data (Table 2.5) using standard MM+ methods. The energy-minimized models are presented Figure 2.23. The model of GdL1- Cu^{2+} reflects a distorted tetragonal geometry around the Cu center as predicted by XAS. The geometry of the NTS Cu^{2+} site in HSA reflects a square pyramidal geometry similar to the previously reported crystal structures,⁶⁵ while Cu center in the ternary complex is a distorted octahedral geometry. These models support the EPR and XAS data by predicting only small differences in coordination geometry of GdL1- Cu^{2+} -HSA compared to HSA- Cu^{2+} .

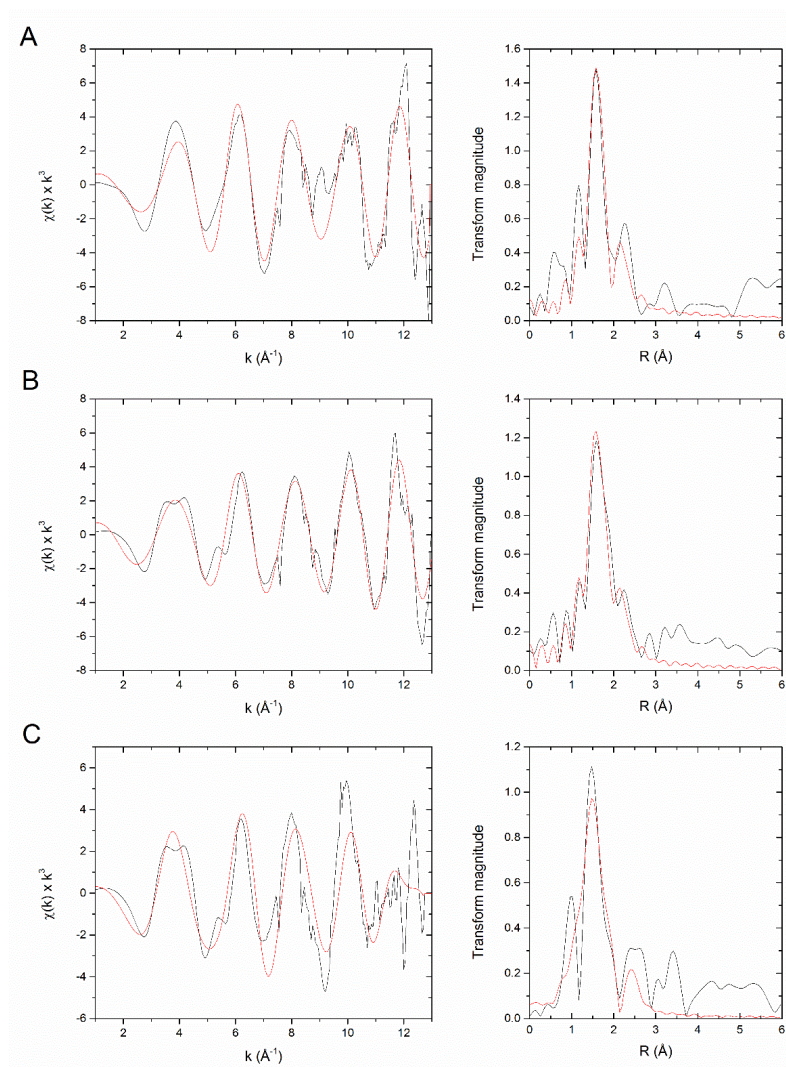


Figure 2.22. EXAFS experimental oscillations (black lines) and corresponding calculated best fits (red lines) and corresponding EXAFS Fourier transforms determined for GdL1-Cu(II) (A), HAS-Cu(II) (B) and GdL1-Cu(II)-HAS (C).

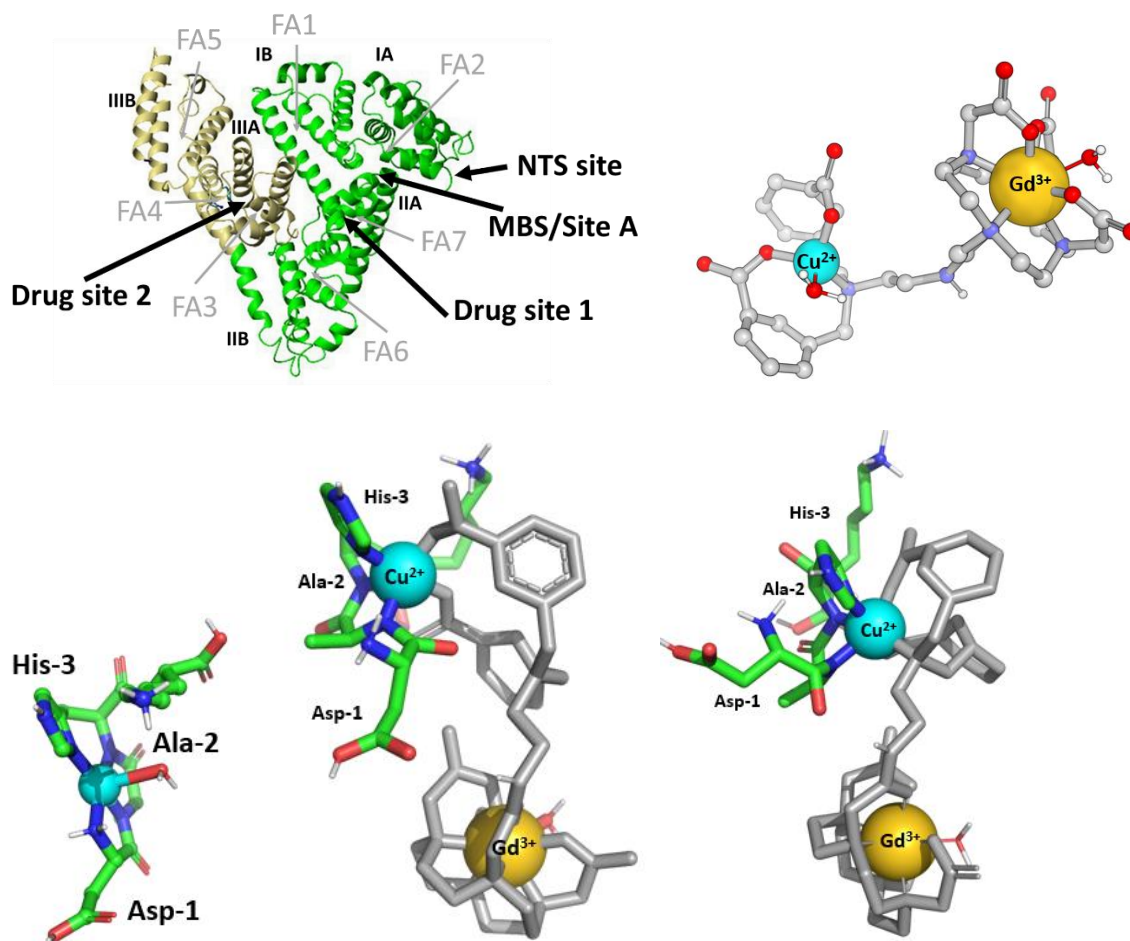


Figure 2.23. MM⁺ minimized structures of (A) Domain structure of albumin (PDB ID code 1AO6): domain I and II are colored green (residues 1–373), domain III in yellow (residues 380–571), long chain fatty acid sites (FA), Sudlow's drug binding sites, Cu²⁺ binding NTS site and zinc binding site A (MBS/Site A) are also shown. (B) GdL1-Cu²⁺ complex (C) HSA-Cu²⁺ complex (CCDC-809109)⁵² (D) HSA-Cu²⁺-GdL1 distorted square pyramidal complex (E) HSA-Cu²⁺-GdL1 distorted octahedral complex consistent with all NMR, XAS and EXAFS data. Hydrogen atoms and other sites of HSA have been removed to simplify visualization. Only residues at NTS site in HSA are included. These figures were generated using HyperchemTM7.5

2.4.11 In vivo imaging of free copper pools in living mice

Most serum copper is bound to ceruloplasmin, a multi-copper oxidase. Nevertheless, serum albumin acts as transporter protein to maintain total exchangeable forms of copper in the μM range.⁹⁰⁻⁹⁵ To examine the possibility of using GdL1 to image excess, free Cu^{2+} ions *in-vivo*, T_1 -weighted images of phantoms containing GdL1 various amounts of Cu^{2+} and HSA were acquired at 9.4T (Figure 2.24). Phantom images of 100 μM of GdL1 in the presence of various concentration of Cu^{2+} (0, 25, 50, 75 and 100 μM) suggests that GdL1 should be able to detect differences in copper levels in the micromolar range. Addition of 600 μM HSA to each of those solutions further enhanced the signal intensity (shorter T_1 s) as expected for an increase in r_1 .

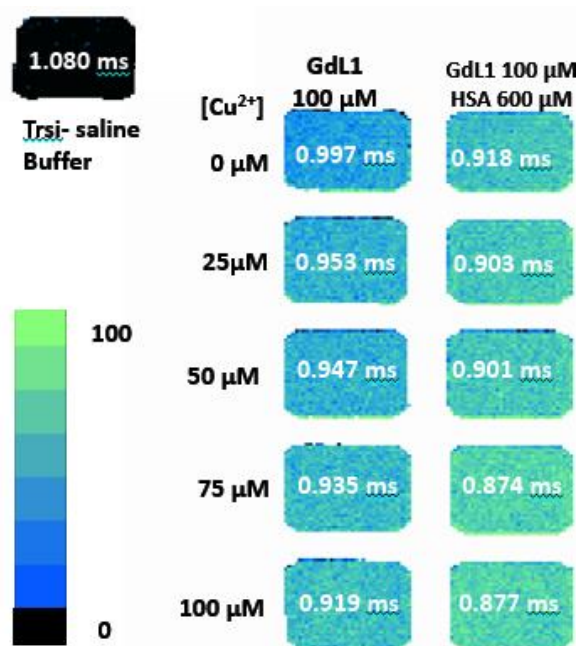


Figure 2.24. T_1 -Weighted phantom MR images. Repetition time (TR) = 2500.0 ms; echo time (TE) = 10.0 ms; Data Matrix = 256 x 256. Images and T_1 values were obtained at 400 MHz (9.4T).

Most dietary absorbed copper is transported to the liver via enterohepatic circulation. Hence, the liver has a key role in copper homeostasis by facilitating copper storage and incorporating copper into ceruloplasmin. An abnormal copper metabolism that results in either elevated or reduced copper in the liver is usually associated with neurological disorders and liver diseases. Therefore, a non-invasive *in vivo* method to image those abnormalities is of broad interest. T₁-weighted MR images of the liver of healthy mice C57b1/6 are shown in Figure 2.25. After i.e. injection of a bolus with 0.1 mmol/kg GdL1, an average signal intensity enhancement of 25% was observed in the liver compared to the pre-contrast images. The liver signal intensities return to baseline after 15-30 minutes post-injection, indicating fast excretion of GdL1. To demonstrate the capacity of GdL1 to detect various levels of labile copper pools in the living mice, in separate experiments, mice were treated with the copper chelator, ATN-224 (5 mg/kg), two hours prior to injection of GdL1.^{96, 37} In those animals, the average signal intensity gain after injection of 0.1mmol/kg GdL1 was only ~11%. This shows that pre-treatment with the copper chelator removed much of the excess Cu²⁺ prior to injection of GdL1. The tissue distribution of Cu and Gd in the same mice used in the imaging experiments were determined by ICP-MS analysis (Figure 2.28C). The results confirmed that the higher MR signal intensities directly correlated with higher copper levels in the liver of healthy C57b1/6 mice.

It should be noted that the Gd³⁺ content was similar for both ATN-224 treated and non-treated animals. No significant contrast enhancement was observed when an equivalent amount of Gadavist, a clinically approved hepatobiliary contrast agent, was substituted for GdL1 (Figure 2.28B). Taken together, these data demonstrate that it is possible to detect variations in extracellular exchangeable liver copper *in vivo* using the Cu²⁺- sensitive MR agent, GdL1.

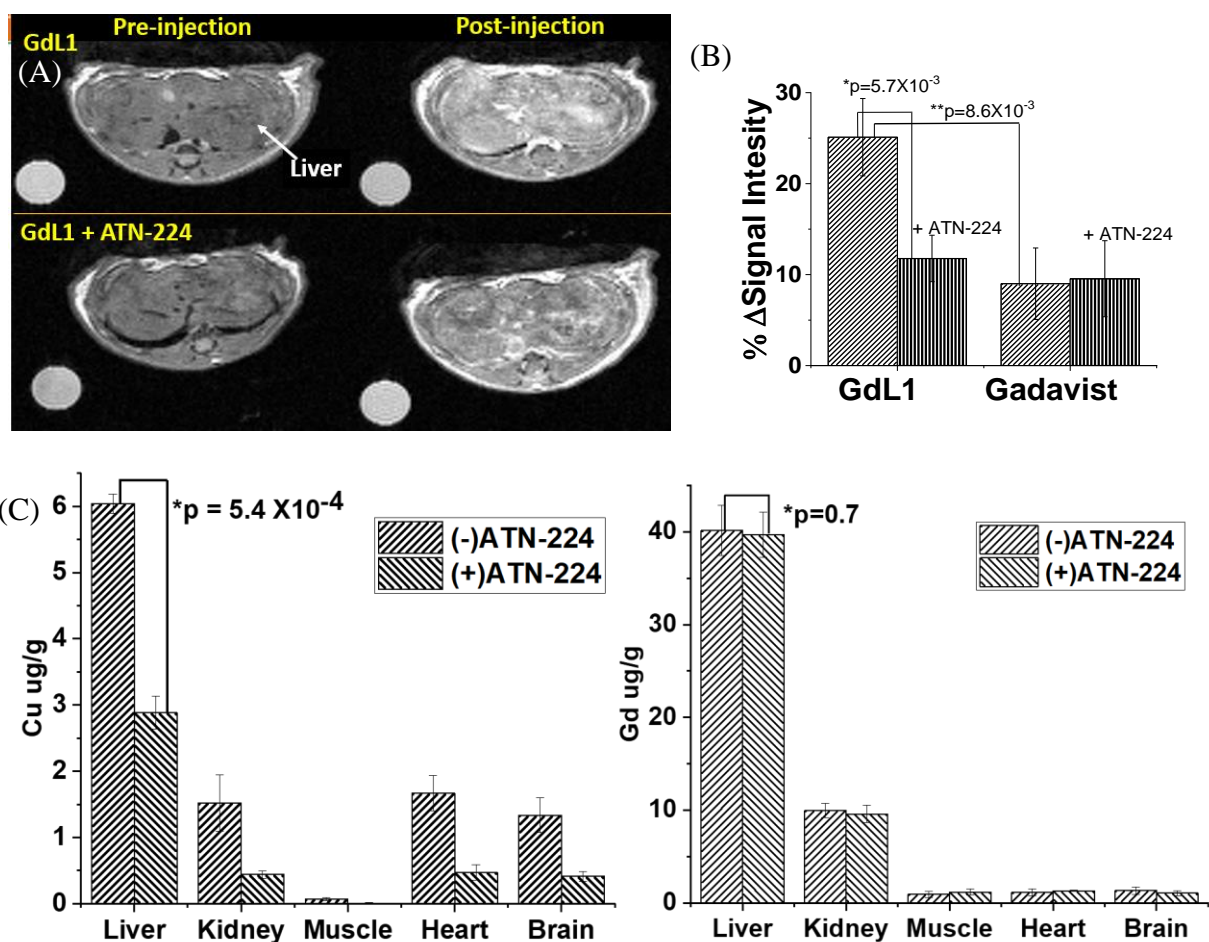


Figure 2.25. (A) *In vivo* MRI images of wild type mouse liver (n=3) pre- and post-injection of GdL1 (0.1mmol/kg) without (top) or with (bottom) pretreatment with ATN-224 (5mg/kg in 50ul). All images were obtained at 4.7 T. (B) The average MRI signal intensity of mouse liver 6 min after injection of GdL1 in control mice *versus* mice pretreated with ATN-224. The columns on the right show the same measurements for animal injected with Gadavist™ rather than GdL1. The data were compared using a two-tailed student t-test. $*p < 0.05$ (n=3); error bars reflect \pm SD. (C) Total Cu and Gd ($\mu\text{g/g}$ tissue) in various tissues collected from the mice with or without pretreatment of ATN-224, 6 min after the injection of GdL1. Tissue copper levels relative to tissue wet weight were determined by ICP-MS. The data were compared using a two-tailed student t-test. $*p < 0.05$ (n=3); error bars reflect \pm SD.

In this study, we have investigated whether a new macrocyclic gadolinium complex, GdL1, could bind with divalent Cu^{2+} selectively. We also explored the properties of the formation of a ternary complex GdL1- Cu^{2+} -HSA that resulted in magnified longitudinal r_1 relaxivity of $22.6 \text{ mM}^{-1}\text{s}^{-1}$. Our results showed that the observed r_1 enhancement due to the slow tumbling of the ternary complex was sufficient to allow detection of μM levels of freely available Cu^{2+} in the liver by T_1 -weighted MR imaging. After injection of GdL1 into healthy untreated mice, the liver was nicely enhanced at 3-5 min, and image contrast returned to background levels after ~ 30 min. However, when mice were treated with ATN-224, the MR signal intensity variation at the liver was $\sim 50\%$ less compared to control animals. The lower contrast enhancement observed in the liver of mice pretreated with ATN-224 paralleled the reduction in total liver copper as detected by ICP-MS. To our knowledge, this is the first report of non-invasive detection of excess Cu^{2+} in the liver by MRI. The second goal of this study was to identify the Cu^{2+} donor atoms on GdL1 and in the ternary GdL1- Cu^{2+} -HSA complex. Although the exact location of Cu^{2+} in GdL1- Cu^{2+} -HSA remains a challenge, the fact that Cu^{2+} has only one high-affinity site on HSA, the N-terminal site,^{65,67} it is reasonable to assume that GdL1 also binds at this site by contributing donor atoms to Cu^{2+} . This model is consistent with the changes in the Cu^{2+} coordination sphere as reported by EPR and X-ray absorption spectroscopy (XAS) data. The combined results indicate that the Cu^{2+} binds to GdL1 via a single tertiary N atom and two carboxylate O atoms on GdL1 and a single water molecule to form a distorted tetragonal complex. The Cu^{2+} center in GdL1- Cu^{2+} -HSA ternary complex is coordinated to four equatorial nitrogen donor atoms from the protein and one or two axial O/N donor from GdL1 resulting distorted octahedral/square pyramidal geometry. The slight

coordination changes in the Cu^{2+} center with GdL1 in the presence of HSA results in a stable ternary complex that results in a surprisingly high r_1 relaxivity.

2.5. Conclusion

In summary, our study shows that GdL1 can be used as a selective sensor to Cu^{2+} ions. In the presence of HSA, the copper freely available in solution can form a stable ternary complex GdL1- Cu^{2+} -HSA that magnifies r_1 relaxivity to such an extent that *in vivo* detection of exchangeable Cu^{2+} MR imaging was possible. To our knowledge, this is the first time that extracellular copper levels in the liver could be detected and with a remarkable statistical difference. Although this work has not included a mouse disease model to validate the obtained results, there is enough evidence to show that this sensor can easily be used in different applications of significant relevance. The total serum copper levels can be markedly elevated in acute liver failure due to its release of excess copper ions from liver tissue stores. This results in elevated total serum Cu^{2+} not bound to ceruloplasmin referred to as “free-copper”.⁹⁷ For example, Wilsons’ disease patients reported significantly higher concentration of serum non-ceruloplasmin copper ($>4.0\mu\text{M}$) in the blood⁹⁸ and hepatic copper content of $>250\mu\text{g}$ per gram of dry liver weight.⁹⁹ Similarly, deficiency of copper has been reported in a variety of genetic, neurological, cardiovascular and metabolic disease.^{9,101} Furthermore, it has recently been shown that elevated serum and tumor copper levels are linked to the progression of cancer malignancy¹⁰² and also plays an important role in the regulation of sleep-related and arousal behaviors.¹⁰³ Therefore, we believe that the observations reported here using GdL1 will catalyze discoveries of Cu^{2+} -responsive MRI agents for imaging

acute liver conditions such as that found in Wilsons diseases or elevated copper levels in other diseases conditions.

REFERENCE

1. Puig, S.; Thiele, D.J. *Curr. Opin. Chem. Biol.* **2002**, 6, 171-180.
2. Maryon, E.B.; Molloy, S.A.; Zimnicka, A.m.; Kaplan, J.H. *Biomaterials*. **2007**, 20, 355- 364.
3. Linder MC, Wooten L, Cerveza P, Cotton S, Shulze S, Lomeli N. *Am J Clin Nutr.* **1998**,67,965S–71S.
4. Prohaska, J.R.; Gybina, A.A. *J. Nutr.* **2004**, 134, 1003-1006.
5. Lutsenko, S.; Barnes, N.L.; Bartee, M.Y.; Dmitriev. O.Y. *Physiol Rev.***2007**. 87,1011-1046.
6. Balamurugan K.; Schaffner W. *Biochim Biophys Acta.* **2006**,1763,737–46.
7. Macreadie I.G. *Eur. Biophys. J.* **2007**, 37, 295–300.
8. Waggoner, D.J.; Bartnikas, T.B.; Gitlin, J.D. *Neurobiol. Dis.* **1999**, 6, 221-225.
9. Que, E.L.; Domaille, D.W.; Chang, C.J. *Chem. Rev.* **2008**, 108, 1517–1549.
10. Zatta, P.; Frank A. *Brain Res Rev.* **2007**, 54,19–33.
11. Bush, A.I. *Curr. Opin. Chem. Biol.* **2000**, 4, 184-191.
12. Brown, D.R.; Qin, K.F.; Herms, J.W.; Madulaung, A.; Manson, J.; Strome, R.; Fraser, P.E.; Kuck, T.; Bohlen A.V.; Schulz- Schaeffer, W.; Giese, A.; Westway, D.; Kretzscmar, H. *Nature*, **1997**, 390, 684-687.
13. Morgan, M. T.; Bagchi, P.; Fahrni, C. J. *Encyclopedia of Inorganic and Bioinorganic Chemistry*.**2013**, 1–19.
14. Rae, T.D.; Schmidt, P.J.; Pufahl, R.A.; Culotta,V.C.; O’Halloran, T.V. *Science*, **1999**, 284, 805.
15. Gaggelli, E.; Kozlowski, H.; Valensin, D.; Valensin, G. *Chem. Rev.* **2006**, 106, 1995-1998.
16. Waggoner, D.J.; Bartnikas, T.B.; Gitlin, J.D. *Neurobiol. Dis.* **1999**, 6, 221-230.
17. Desai, V.; Kaler, S.G. *Am J Clin Nutr.* **2008**, 88, 855S-858S.
18. Multhaup, G.; Schlicksupp, A.; Hesse, L.; Beher, D.; Ruppert, T.; Masters, C.L.; Beyreuther, K. *Science*, **1996**, 271, 1406-1409.

19. Bertini, I.; Rosato, A., *Cell Mol. Life Sci.* **2008**, 65, 89-91.
20. Kaler, S.G., *Nat. Rev. Neurol.* **2011**, 7, 15-29.
21. Lutsenko, S.; Gupta, A.; Burkhead, J.L.; Zuzel, V., *Arch. Biochem. Biophys.* **2008**, 476, 22-32.
22. Cox, D.; Moore, S.D., *J Bioenerg. Biomembr.* **2002**, 34, 333-338.
23. Valentine, J.S.; Doucette, P.A.; Potter, S.Z., *Annu. Rev. Biochem.* **2005**, 74, 563- 572.
24. Peng, F.; Lutsenko, S.; Sun, X.; Musik, O., *Mol. Imaging Biol.* 2012, 14, 70-78.
25. Peng, F., *Ann. N.Y. Acad. Sci.* **2014**, 1314, 24–31.
26. Aime, S.; Botta, M.; Terreno, E., *Adv. Inorg. Chem.*, **2005**, 57, 173-232.
27. Aime, S.; Botta, M.; Fasano, M.; Terreno, E., *Chem. Soc. Rev.*, **1998**, 27, 19-29.
28. Caravan, P.; Ellison, J. J.; McMurry, T.J; Lauffer, R.B., *Chem. Rev.*, **1999**, 99, 2293-2352.
29. Que, E.L.; Domaille, D.W.; Chang, C.J. *Chem. Rev.* **2008**, 108, 1517.
30. Moats, R.A.; Fraser, S.E.; Meade, T.J., *Angew. Chem. Int. Ed. Eng.*, **1997**, 36, 726-732.
31. Raghunand, N.; Howison, C.; Sherry, A.D.; Zhang, S.; Gillies, R.J., *Magn. Reson. Med.*, **2003**, 49, 249-257.
32. Aime, S.; Botta, M.; Gianolia, E.; Terreno, E., *Angew. Chem. Int. Ed.*, **2000**, 39, 747-754.
33. Berkowitz, B.A.; Handa, J.T.; Wilson, C.A., *NMR Biomed.* **1992**, 51, 65-71.
34. Que, E.L.; Chang, C.J., *J. Am. Chem. Soc.* **2006**, 128, 15942.
35. Que, E. L.; Gianolio, E.; Baker, S. L.; Wong, A. P.; Aime, S.; Chang, C. J. *J. Am. Chem. Soc.* **2009**, 131, 8527.
36. Li, W.S.; Luo, J.; Chen, Z.N., *Dalton Trans.* **2011**, 40, 484-492.
37. Hirayama, T.; Van de Bittner, G.C.; Gray, L.W.; Lutsenko, S.; Chang, C.J. *PNAS*, **2012**, 109, 2228-2233.

38. Jordan, M.V.C.; Lo, S.; Chen, S.; Preihs, C.; Chirayil, S.; Zhang, S.; Kapur, P.; Li, W.; Leon-Rodriguez, L.M.D.; Lubag, A.J.M.; Rofsky, N.M.; Sherry, A.D., *PNAS*, 2016, 113, E5464-E5471.
39. Lubag, A.J.M.; Leon-Rodriguez, L.M.D.; Burgess, S.C.; Sherry, A.D., *PNAS*, **2011**, 108, 18400-18405.
40. Yu, J.; Martins, A.F.; Preihs, C.; Clavijo-Jordan, V.; Chirayil, S.; Zhao, P.; Wu, Y.; Nasr, K.; Kiefer, G.E.; Sherry, A.D., *J. Am. Chem. Soc.*, **2015**, 137, 14173–14179.
41. Esqueda, A. C.; López, J. A.; Andreu-de-Riquer, G.; Alvarado-Monzón, J. C.; Ratnakar, J.; Lubag, A. J. M.; Sherry, A. D.; De León-Rodríguez, L. M. *J. Am. Chem. Soc.* **2009**, 131, 11387- 11391.
42. Gaur, A.; Klysubun, W.; Nair, N.N.; Shrivastava, B.D.; Prasad. J.; Srivatava, K., *Journal of Molecular Structure*, **2016**, 1118, 212-218.
43. Laussac, J.P; Sarkar, B., *Biochemistry*, **1984**, 23, 2832-2838.
44. Zgierski, A.; Friden, E. *J. Inorg. Biochem.* **1990**, 39, 137-149.
45. Bal, W. Christodoulou, J.; Sadler, P.J.; Tucar, A., *J. Inorg. Biochem.* **1998**, 70, 33-39.
46. Lu, J.; Stewart, A.J.; Sadler, P.J.; Pinheiro, T.J.T.; Blindauer, C.A. *Biochem. Soc. Trans.* **2008**, 36, 1317-1321.
47. Hu, H.; Lim, N.; Ding-Pfennigdorff, D.; Saas, J.; Wendt, K.U.; Ritzeler, O.; Nagase, H.; Pletenburg, O.; Schultz, C.; Nazare, M.; *Bioconjugate Chemistry* **2015** 26 (3), 383-388.
48. ChemAxon – Software for Chemistry and Biology <https://www.chemaxon.com/> (accessed June 15, 2017).
49. Kiyose, K.; Kojima, H.; Urano, Y.; Nagano, T. *J. Am. Chem. Soc.* **2006**, 128, 6548–6549.
50. Martins, A. F.; Morfin, J.-F.; Geraldès, C. F. G. C.; Tóth, É. *J. Biol. Inorg. Chem.* **2013**, 19, 281–295.
51. Martins, A. F.; Morfin, J.-F.; Kubíčková, A.; Kubíček, V.; Buron, F.; Suzenet, F.; Salerno, M.; Lazar, A. N.; Duyckaerts, C.; Arlicot, N.; Guilloteau, D.; Geraldès, C. F. G. C.; Tóth, É. *ACS Med. Chem. Lett.* **2013**, 5, 436–440.
52. Muller, N.; Lapique, F.; Drelon, E.; Netter, P. *J. Pharm. Pharmacol.* 1994, 46, 300-304.

53. Yu, J.; Martins, A.F.; Preihs, C.; Clavijo-Jordan, V.; Chirayil, S.; Zhao, P.; Wu, Y.; Nasr, K.; Kiefer, G.E.; Sherry, A.D., *J. Am. Chem. Soc.*, **2015**, 137, 44, 14173–14179.
54. Silverio, S.; Torres, S.; Martins, A. F.; Martins, J. A.; Andre, J. P.; Helm, L.; Prata, M. I. M.; Santos, A. C.; Geraldès, C. F. G. C. *Dalton Trans.* **2009**, 24, 4656–4670.
55. Laurent, S.; Vander Elst, L.; Henoumont, C.; Muller, R. N. *Contrast Media Mol. Imaging* **2010**, 5, 305–308.
56. Jiang, D.; Min, L.; Wang, J.; hang, Y.; Chickenyun, S.; Wang, Y.; Zhou, F., *Biochemistry*, **2007**, 46, 9270-9282.
57. Bal, W.; Christodoulou, J.; Sadler, P. J.; Tucker, A. In *Metal Ions in Biology and Medicine*; Collery, Ph., Poirier, L. A., Littlefield, N. A., Etienne, J. C., Eds.; *Eurotext: Paris*, **1994**; 43-45.
58. Chuquing, C.; Santos, O.; Xu, X.; Canarg, J.W., *Inorg. Chem.*, **1997**, 36, 1967-1972.
59. George, G.N., <http://ssrl.slac.stanford.edu/exafspak.html>.
60. Shakhdofa, M.; Shtaiwi, M.; Morsy, N.; Abdel-raseel, T.M.A., *Main Group Chemistry*, **2014**, 13, 187-218.
61. Zhang, G.; Zhong, W.; Wei, Z.; Liu, Z.; Liu, X., *Dalton Transactions*, **2017**, 46, 8286-8297.
62. Vymazal, J.; Bulte, J. W. M.; Frank, J. A.; Chiro, G. D.; Brooks, R. A. *J. Magn. Reson. Imaging*, **1993**, 3, 637–640.
63. Casella, L.; Gullotti, M.; Pallanza, G.; Bugli, M.; *Biol. Metals.*, **1990**, 3, 137-142.
64. Job, P., *Ann.Chim(Paris)*, **1928**, 113-115.
65. Guo, M.; Zou, J.; Li, P.; Shang, Z.; Hu, G.; Yu, Q.; *Anaytical Sciences*, **2004**, 20, 465-470.
66. Cabaniss, S.E.; Shuman, M.S.; *Anal. Chem.* **1986**, 58, 398-401.
67. Hureau, C.; Eury, H.; Guillot, R.; Bijani, C.; Sagen, S.; Solari, P.; Guillon, E.; Faller, P.; Dorlet, P. *Chem. Eur. J.* **2011**, 17, 10151-10160.
68. Bal, W.; Christodoulou, J.; Sadler, P.J.; Tucker, A., *Journal of Inorganic Biochemistry*, **1998**, 70, 33-39.
69. Sokolowska, M.; Pawlas, K.; Bal, W., *Bioinorg. Chem. Appl.*, **2010**, 725153-725156.

70. Neumann, P.Z.; Sass- Kortsark, A., *Journal of Clinical Investigation*, **1967**, 46, 646-658.
71. Sudlow, G.; Birkett, D.J.; Wade, D.N., *Molecular Pahrmacology*, **1975**,11, 824-832.
72. Sudlow, G.; Birkett, D.J.; Wade, D.N., *Molecular Paharmacology*, **1976**, 12, 1052-1061.
73. Montgomery, C.P.; New, E.J.; Parker, D.; Pealock, R.D., *Chem. Commun*, **2008**, 4261-4263.
74. Kehske, K.J.; Muller, W.E.; Wollert, U; *Biochemical Paharmacology*, **1981**, 7, 687-692.
75. Krenzel, E.S.; Chen, Z.; Hamilton, J.A., *Biochmeistry*, **2013**,52, 1559-1567.
76. Muller, N.; Lapique, F.; Drelon, E.; Netter, P. *J. Pharm. Pharmacol.* **1994**, 46, 300-304.
77. Sherry, A.D.; Wu, Y., *Curr. Opin, Chem, Biol.* **2013**, 17, 167-714.
78. Gonzalez, G.; Powell, D.H.; Tissieres, V.; Merbarch, A.E., *J. Phys. Chem.* **1994**,98,53-59.
79. Aime, S.; Botta, M.; Fasano, M.; Crich, S.G.; Terreno, E., *Coordination Chemistry Reviews*, **1999**, 321-333.
80. Caravan, P.; Farrar, C.T.; Frullano, L.; Uppal. R., *Contrast Media Mol. Imaging.* **2009**,4, 89-100.
81. Merch, A.E.; Helm, L.; Toth, E., *The Chemistry of Contrast Agents in Medical Magnetic Resonance Imaging*, John Wiley & Sons, **2013**.
82. Tweedle, M. F.; Hagan, J. J.; Kumar, K.; Mantha, S.; Chang, C. A. *Magn. Reson. Imaging* **1991**, 9, 409–415.
83. Xio, Y.; Zhao, G.; Fang, X.; Zhao, Y.; Wang, G.; Yang, W.; Xu, J., *RSC Adv*, **2014**, 4, 34421- 34427.
84. Mukherjee, P.; Drew, M.G.B.; Figenerola, A., *Polyhedron*, **2008**, 27, 3343-3345.
85. Mouni, L.; Akkurt, M.; Yildrim, S.O., *J. Chem. Crystallogr.* **2010**, 20, 169- 172.
86. Karabiyik, H.; Erdem, O.; Aygun, M., *J. Inorg. Organomet. Polym*, **2010**, 20, 142-145.
87. Martins, D.A.; Gourea, L.R.; Muniz, G.S.; Louro, S.; Gama, D.; Soeiro, M.; Teixeira, L.R., *Bioinorganic chemistry and application*, **2016**, 1-11.
88. Sadler, P.J.; Viles, J.H., *Inorg. Chem.* **1996**, 35, 4490-4496.

89. Sano, M.; Komorita, S.; Yamatera, H., *Inorg. Chem* **1992**, 31, 459-463.
90. Askwith, C.; Eide, D.; Van Ho, A.; Bernard, P.S.; Li L.; Davis-Kaplan, S.; Sipe, D.M.; Kaplan J., *Cell*, **1994**, 76,403–10.
91. Linder, M.C.; Massaro, E.J., editor. Handbook of copper pharmacology and toxicology. Humana Press: New Jersey; **2002**. 3–32.
92. Zatta P, Frank A. *Brain Res Rev.* **2007**;54:19–33.
93. Vural, H.; Uzun, K.; Uz, E.; Kocgilgil, A.; Cigli, A.; Akyol, O., *J, Trace Elements Med.Biol.*, **2000**, 14, 88-91.
94. Alebic-Juretic. A.; Frkovic, A.; *J. of Trace Elements in Medicine and Biology*, **2005**, 19,191-194.
95. Linder MC, Wooten L, Cerveza P, Cotton S, Shulze S, Lomeli N. *Am J Clin Nutr.*, **1998**, 67,965S–971S.
96. Lowndes, S.A.; Sheldon, H.V.; Cai, S.; Taylor, J.M.; Harris, A.L., *Microvascular Research*, **2009**, 77, 314-326.
97. Ferenci, P.; Czlonkowska, A.; Merle, U.; Ferenc, S.; Gromadzka, G.; Yurdaydin, C.; Vogel, W.; Bruha, R.; Schmidt, H.T.; Strmmel, W., *Roenterology*, **2007**, 132, 1294-1298.
98. Frommer, D.J., *Clinica Chimica Acta*, **1976**, 68, 3030-307.
99. Yang, X.; Tang X.P.; Zhang, Y.H.; Luo, K.Z.; Jiang Y.F.; Luo H.Y.; Lei J.H.; Wang, W.L.; Li, M.M.; Chen, H.C.; Deng, S.L.; Lai, L.Y.; Liang, J., Zhang, M.; Tian, Y.; Xu, Y., *Hepatology*. **2015**, 62, 1731-41.
100. Poujois, A; Trocello, J-M; Djebrani-Oussedik, N; Poupon, J; Collet, C; Girardot-Tinant, N; Sobesky, R; Habès, D; Debray, D; Vanlemmens, C; Fluchère, F; Ory-Magne, F; Labreuche, J; Preda, C; Woimant, F, *European journal of neurology*. **2017**, 24,154-160.
101. Heffern, M. C.; Park, H. M.; Au-Yeung, H. Y.; Van de Bittner, G. C.; Ackerman, C. M.; Stahl, A. Chang, C. J. *Proc. Natl. Acad. Sci. USA* **2016**, 113, 14219-14224.
102. Mumper, R.J.; Gupte, A., *Cancer treatment Reviews*, **2009**, 35, 32-46.
103. Xiao, T; Ackerman, C.M.; Carroll, E.C.; Jia, S.; Hogland, A.; Chan, J.; Thai, B.; Liu, C.S.; Iscaccioff, E.Y.; Chang, C.J., *Nature Chemical Biology*, **2018**, 14,655–663.

CHAPTER 3
A NOVEL PH-SENSITIVE MRI CONTRAST AGENT BASED UPON GDDOTA-
MONOAMIDE METHYLENE PHOSPHONATE

Authors- Namini N. Paranawithana¹, Andre F. Martins ¹, Katherine Lopez³, Piyu Zhao¹, Gary
Kiefer^{1,3}, Paul Jurek³, and A. Dean Sherry^{1,2}

¹The Department of Chemistry and Biochemistry, BE26
The University of Texas at Dallas
800 West Campbell Road
Richardson, Texas 75080-3021

²Advanced Imaging Research Center
The University of Texas Southwestern Medical Center
2201 Inwood Road
Dallas, Texas 75390-8568

³Macrocyclics, Inc., An Orano Med Company,
700 Klein Road,
Plano, Texas 75074

NP, PZ, AFM, KL, GEK and PJ carried out the experiments. NP, AFM, PJ and ADS performed the data analysis. NP, AFM, PJ and ADS conceived the project and drafted the manuscript. All authors read and approved the manuscript.

3.1 Abstract

A simple GdDOTA-monoamide derivative, GdDOTA-1AmP, exhibits a surprisingly large increase in r_1 relaxivity from 3.0 to 6.3 $\text{mM}^{-1}\text{s}^{-1}$ as the pH is reduced from 9 to 2.5. The origin of this unique pH sensitivity was traced to protonation of the single phosphonate side-chain which, upon protonation, catalyzes exchange of protons between a Gd-bound water molecule and bulk water. T_1 -weighted images of phantoms showed that MR image intensity increased 12-fold between a physiological pH of 7.4 and pH 6. This demonstrates it is possible to design simple, small molecule MRI contrast agents that respond to pH using simple acid-base principles.

3.2 Introduction

Tissue pH is normally tightly regulated in cells by a variety of proton pumps, endogenous buffers, and rapid removal of excess acid by renal filtration.^{1,2} Interruption of this delicate balance and accumulation of excess tissue acid is associated with ischemia, infection, inflammation, various kidney disorders²⁻⁷ and most notably, cancer.^{2,3,8} Tumors are characteristically hypermetabolic and generate excess acid that is rapidly pumped into their extracellular space and this can result in aggressive and treatment resistant phenotypes.^{9,10} Thus, a simple method for reporting the extracellular pH of a tumor could be informative for choosing the best therapy. To date, despite much effort toward developing biomarkers of extracellular pH, agents for precisely imaging the extracellular pH of tumors *in vivo* non-invasively have not been reported.

A number of different spectroscopic and/or imaging techniques have been proposed for pH measurements, including magnetic resonance imaging (MRI)¹¹, magnetic resonance spectroscopy (MRS)¹² and positron emission tomography (PET)¹³. MRI has shown the most promise for

mapping tissue pH because it provides exquisite anatomical images, unlimited tissue depth, and directly detects tissue water protons.¹³⁻¹⁷ Several MRI approaches have been used to map extracellular pH including paramagnetic chemical exchange saturation transfer (paraCEST) agents¹⁷⁻²⁰ and a few gadolinium-based T_1 agents.²¹ Paramagnetic inorganic complexes known as contrast agents (CAs) have been widely used in MRI to alter the image contrast by shortening the $T_{1,2}$ relaxation time of water protons. Most Gd^{3+} -based contrast agents have a single water molecule in rapid exchange with bulk water. Efficient relaxation of the inner-sphere water molecule followed by fast exchange provides an efficient mechanism for relaxation enhancement (T_1 and T_2) of water protons. If water exchange is too slow or too fast in a Gd complex, this manifests as a lower than optimal r_1 or r_2 relaxivity so one approach in the design of a pH-sensitive contrast agent might be to alter the rate of water exchange rate. An optimal bound water lifetime for a Gd-based pH sensor is about 20-40 ns, about an order of magnitude shorter than most common current Gd-based agents, so if one could catalyze faster exchange of the bound water protons, this should also result in an increase in r_1 . Using this concept, our group previously reported a pH-sensitive agent, GdDOTA-4AmP, that displayed an increase in r_1 under more acidic conditions. This response was shown to be initiated by step-wise protonation of the four phosphonate groups when then act as catalysts to exchange of protons on a single inner-sphere water molecule on the gadolinium ion with protons in bulk water. Although the change in r_1 over the pH range of interest for imaging tissue pH was relatively small ($\Delta r_1 \sim 0.5$ between pH 6-7.4 at 37°C), this change was sufficient to detect the known pH gradient across the mouse kidney by MRI.²² Although GdDOTA-4AmP is also known for its superior kinetic inertness compared to other FDA approved CA,²³ it would be advantageous to lower the overall charge in this complex to improve the tissue

biodistribution of the agent. Hence, this study was designed to learn how many phosphonate groups are needed to initiate fast proton exchange in a pH sensor based on this mechanism. To examine this, we prepared the series of isostructural complexes containing one, two or three extended phosphonate side-chains, GdDOTA-1AmP, GdDOTA-2AmP, and GdDOTA-3AmP (Figure 3.1).

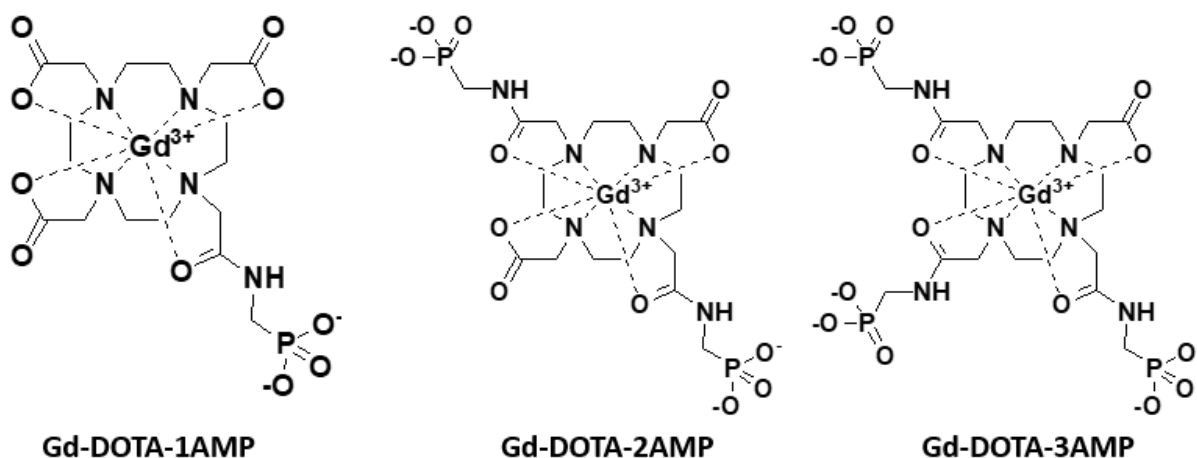


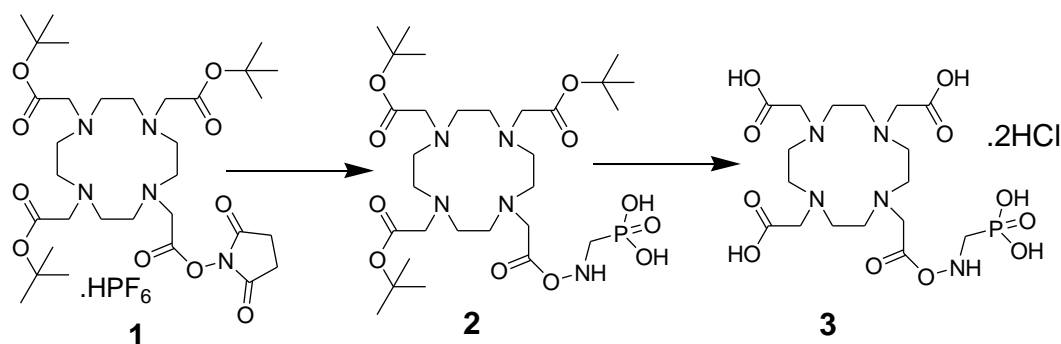
Figure 3.1. Gadolinium-amide phosphonate pH responsive agents

3.3 Experimental section

3.3.1 Methods and Materials

DO3A-tBu₃ was synthesized according to the reported procedure in literature.²⁴ Chemicals were purchased from Sigma–Aldrich (St. Louis, MO), Strem (Newburyport, M), Acros Organics (Morris Plains, NJ), TCI America (Portland, OR), and Alfa Aesar (Ward Hill, MA). They were used as received unless otherwise noted. Column chromatography was performed using Silica gel (200-400 mesh, 60A°), purchased from Sigma-Aldrich. Analytical Thin Layer Chromatography was performed using EMD Millipore precoated aluminum oxide or Whatman precoated Silica gel

on a polyester plate. Analytical HPLC was performed on an Agilent Technologies 1220 Infinity LC using a RESTEK Ultra C-18 IBD column (3 μm , 100 \times 4.6 mm). Preparative HPLC was performed on a Waters Delta Prep HPLC system equipped with a Water® 2996 photodiode array detector and a Phenomenex Kinetex® C18 column (5 μm , 21.2 mm \times 250 mm) or an Atlantis Prep T3 OBD Column (5 μm , 30 mm \times 250 mm). A Fisher Science Education pH-meter coupled with Thermo Scientific Orion Micro pH electrode was used for pH measurements. Milli-Q purified water was used for the preparation of all samples and preparative and analytical HPLC. ^1H and ^{13}C NMR spectra were obtained in deuterated solvents from Cambridge Isotope Laboratories (Cambridge, MA) on a Bruker AVANCE III 400 MHz NMR spectrometer for all synthetic intermediates, final products, ^{17}O temperature studies of all lanthanide complexes. A VirTis Freeze Dryer (Benchtop-k) was used to lyophilize the samples. Mass spectra were obtained using either HT Laboratories (San Diego, CA) instrument or a Waters Alliance e2695 Separations Module coupled with Xevo QToF MS using an Atlantis T3 Column (5 μm , 6 mm \times 250 mm) at The Advanced Imaging Research Center (University of Texas Southwestern Medical Center, Dallas). Inductive coupled plasma mass spectrometry (ICP-MS) was performed for calculating metal concentrations using Agilent 7900. Standard solutions for ICP-MS containing Gd, Eu, La, and Yb were purchased from Inorganic Ventures (Christiansburg, VA). Florescence Measurements were collected in Horiba Fluoromax 4 (Albany, NY) spectrofluorometer. Electronic Paramagnetic Resonance spectroscopy was performed in Bruker EMX Spectrometer with ER 041 XG microwave bridge. Chemical structures and IUPAC names were obtained using Chemaxon MarvinSketch 17.11 and ChemdrawUltra 7.0.²⁵



Scheme 3.1. Synthesis of DOTA-1AmP.

2-[4,10-bis(carboxymethyl)-7-(2-oxo-2-[(phosphonomethyl)amino]oxy)ethyl)-1,4,7,10-tetraazacyclododecan-1-yl]acetic acid dihydrochloride (DOTA-1AmP)

Compound 1 (1.0 g, 6.25 mmol) was Step 1: 4.09g DOTA-mono-NHS-tris-(tButyl)ester (Macrocyclics catalog number B-270) dissolved in 100mL acetonitrile. 0.55g aminomethylphosphonic acid dissolved in 100mL water. Solutions were combined and homogenous. 5.2mL diisopropylethyl amine added. After 1hr the acetonitrile was removed by rotary evaporation at 30C. The aqueous solution was purified by preparative HPLC using the following parameters: 250 x 50mm / 10um / C18 column, 100mL/min, wavelength 215nm, A = acetonitrile, B = 0.001M HCl, 2/98 to 40/60 ramp over 25min. The target peak eluted at 19-20min. The solvent was removed from the kept fractions by rotary evaporation at 40C. Net 2.26g. Yield = 60%. Purity by HPLC 96.2%. HPLC Conditions: 30C, 0.30mL/min, Restek Ultra BiPh column (150 x 2.1, 3um), 0-15min ramp 2/98 to 75/25 A/B, A = 0.1% TFA in CH₃CN, B = 0.1% TFA in H₂O.

2.00g of compound 2 was dissolved in 25mL water and 25mL 6N HCl was added. After 24 hours at room temperature the solvent was removed at 30C. The resulting hygroscopic solid was

dissolved in 100mL water. Solution pH = 1.4. SAX in the -OH form was added to raise the pH = 2.6. The solution was filtered and freeze dried. Net 1.29g. Yield = 75% as the 2HCl salt. Purity by HPLC 95.1%. HPLC Conditions: 30C, 1.25mL/min, Restek Ultra Amino column (250 x 3.0, 5um), 0-15min ramp 5/95/0 to 5/0/95 A/B/C, A = CH₃CN, B = H₂O, C = 50mM phos/Na/HCl buffer pH = 7.0.

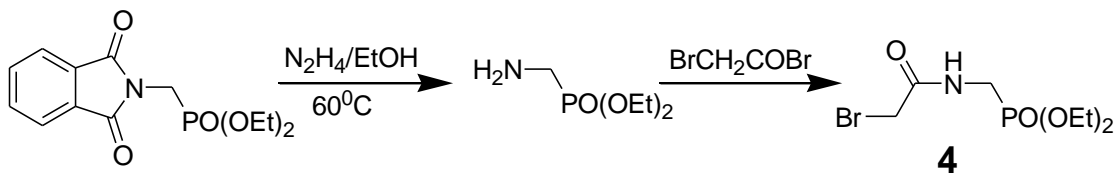
2.00g of compound 2 was dissolved in 25mL water and 25mL 6N HCl was added. After 24 hours at room temperature the solvent was removed at 30C. The resulting hygroscopic solid was dissolved in 100mL water. Solution pH = 1.4. SAX in the -OH form was added to raise the pH = 2.6. The solution was filtered and freeze dried. Net 1.29g. Yield = 75% as the 2HCl salt. Purity by HPLC 95.1%. HPLC Conditions: 30C, 1.25mL/min, Restek Ultra Amino column (250 x 3.0, 5um), 0-15min ramp 5/95/0 to 5/0/95 A/B/C, A = CH₃CN, B = H₂O, C = 50mM phos/Na/HCl buffer pH = 7.0.

¹H NMR (400 MHz, D₂O, TMS): δ 2.56 (8H, br, CH₂NCH₂CH₂NCH₂, macrocycle), 3.15 (8H, br, CH₂NCH₂CH₂NCH₂, macrocycle), 3.30 (2H, d, H₂O₃PCH₂NH), 3.42 (6H, br, HOOCCH₂N), 3.39 (2H, d, NCH₂CONH), 8.12 (CONHCH₂)

¹³C NMR (400 MHz, D₂O, TMS): δ 40.2 (H₂O₃PCH₂NH), 48.9 (NCH₂CH₂NCH₂CH₂N), 50.4 (NCH₂CH₂NCH₂CH₂N), 58.5 (NCH₂CO), 59.1 (NCH₂COOH), 169.2 (NCH₂CON), 174.3 (NCH₂COOH)

³¹P NMR (400 MHz, D₂O, TMS) – 20.23 (S, H₂O₃PCH₂)

MS(ESI-positive) $m/z = 497.20$ [$M-H^+$] (calculated 497.44)



Scheme 3.2. Synthesis of AmPBr.

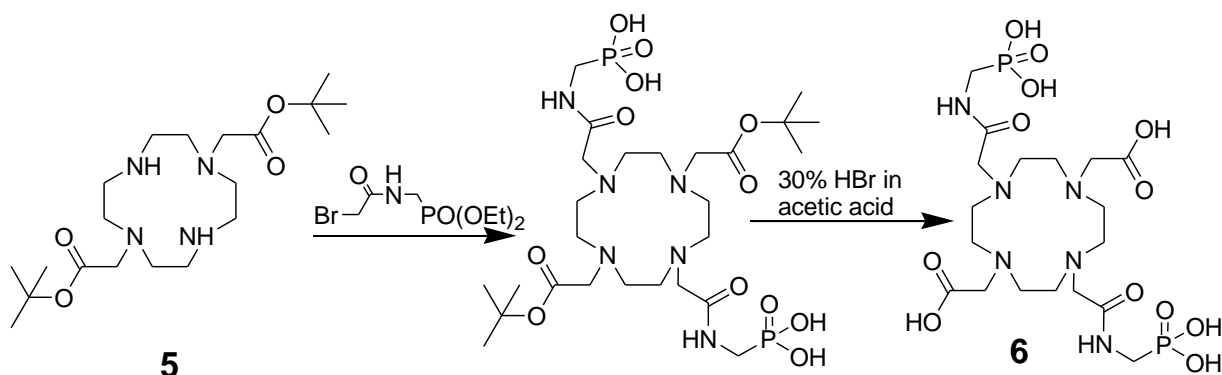
Diethyl bromoacetamidomethyl phosphonate

The synthesis of compound **4** was performed using a previously reported method.²⁷

1H NMR (400 MHz, $CDCl_3$, TMS): δ 1.23 (6H, t, \underline{CH}_3CH_2O), 3.59 (4H, d, $CH_3\underline{CH}_2O$), 5.64 (2H, s, $NH\underline{CH}_2PO$), 4.21 (2H, s, $Br\underline{CH}_2CO$), 8.01 ($CONH\underline{CH}_2$)

^{13}C NMR (400 MHz, $CDCl_3$, TMS): δ 16.0 (\underline{CH}_3CH_2O), 38.1 ($Br\underline{CH}_2CO$), 64.2 ($CH_3\underline{CH}_2O$), 172.6 ($CH_2\underline{CONH}$)

^{31}P NMR (400 MHz, $CDCl_3$): 27.60 (1P, s).



Scheme 3.3. Synthesis of DOTA-2AmP

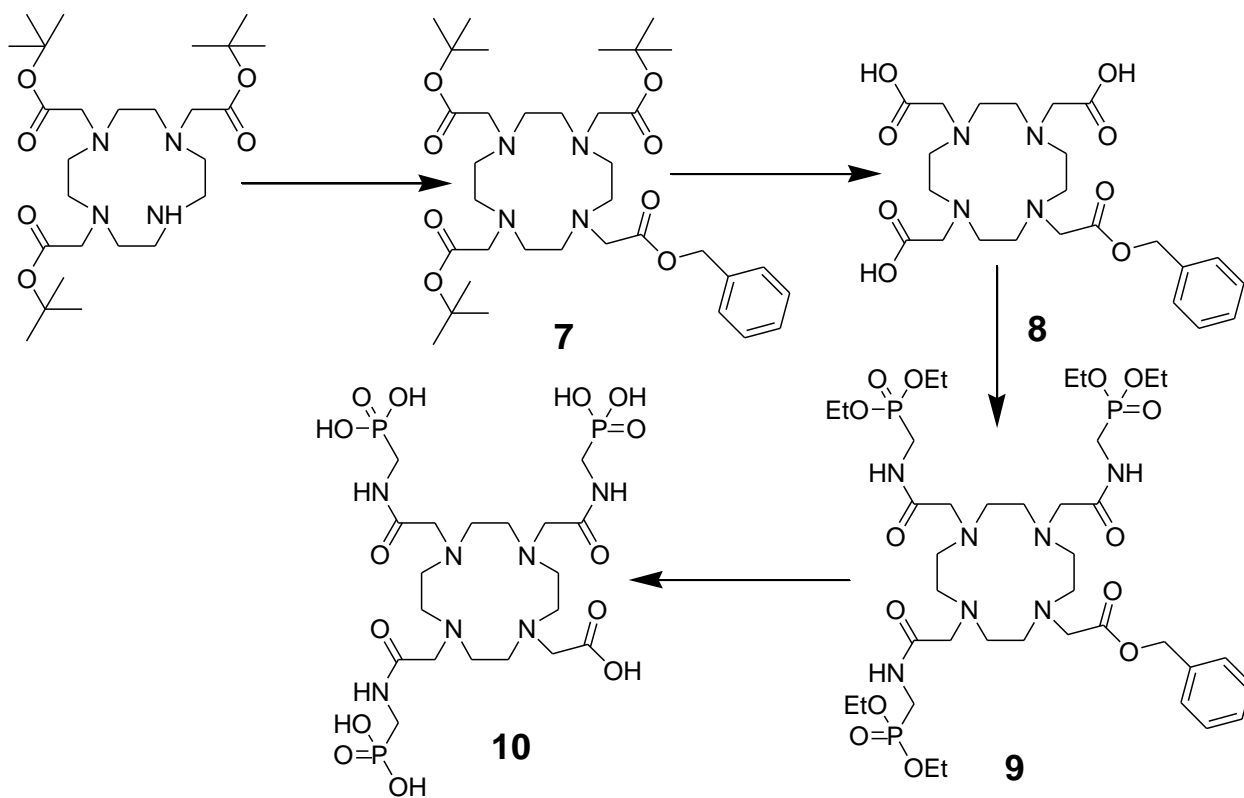
2-[7-(carboxymethyl)-4,10-di{[(phosphonomethyl)carbamoyl]methyl}-1,4,7,10 tetraazacyclododecan-1-yl]acetic acid (DOTA-2AmP)

DO2A-t-Bu ester (Compound 5) was synthesized as reported earlier.⁵⁻⁶ 1 g of compound 5 was dissolved in CH₃CN together with K₂CO₃ (1.0 g, 7.25 mmol, 1 equiv.) and KI (0.5 g, 3.0 mmol). The compound 4 (1.62 g, 5.62 mmol, 2.2 equiv.) was added to solution and reflux for 72 hrs and solvent was removed by rotary evaporation. The residue was dissolved and purified in SiO₂ with CH₂Cl₂ and CH₃OH (R_f = 0.62) to obtain intermediate compound. 1.5 g of this compound (2.5 mmol) was dissolved in 30% solution of HBr in acetic acid (15 ml) and stirred in room temperature (RT) for 18 hrs. The solvent was evaporated, and sample were purified with preparative HPLC to obtain compound 6 (DOTA-2AmP).

¹H NMR (400 MHz, D₂O, TMS): δ 2.41 (8H, br, CH₂NCH₂, macrocycle), 2.52 (8H, br, CH₂NCH₂, macrocycle), 2.91 (4H, d, H₂O₃PCH₂NH), 3.21 (4H, d, NCH₂CO), 8.06 (s, CONHCH₂)

^{13}C NMR (400 MHz, D_2O , TMS): δ 44.1 ($\text{H}_2\text{O}_3\text{PCH}_2\text{NH}$), 51.2 ($\text{NCH}_2\text{CH}_2\text{N}$), 58.4 (NCH_2CON), 60.2 (NCH_2COOH), 169.0 (CH_2CONH), 173.2 (CH_2COOH)

MS(ESI-positive) m/z = 589.19 $[\text{M}-\text{H}^+]$ (calculated 590.46)



Scheme 3.4. Synthesis of DOTA-3AmP.

2-(4,7,10-tri{[(phosphonomethyl)carbamoyl]methyl}-1,4,7,10-tetraazacyclododecan-1-yl) acetic acid (DO3A-3AmP)

Tert-butyl DO3A was synthesized as reported previously.¹ 1.0 g (2.0 mmol, 1 equivalent) of tert-butyl DO3A was dissolved in CH_3CN together with K_2CO_3 and 0.54 g (2.4 mmol, 1.2 equiv.) of Benzyl Bromoacetate. The reaction mixture was refluxed for 72 hrs and solvent was removed

under reduced pressure. The residue was purified by column chromatography over silica gel eluting with 10% MeOH and CH₂Cl₂ (R_f = 0.58) to obtain compound 7. 1.2 g of compound 7 was dissolved in CH₂Cl₂ and 20 ml of TFA, stirred for 8 hrs. The solvent was evaporated to obtain compound 8 and purified with reverse phase HPLC. A solution of compound 8 (0.8 g, 1.62 mmol), (aminomethyl)phosphonic acid (0.6 g, 5.4 mmol), PyBOP (Benzotriazol-1-yloxy) tripyrrolidinophosphonium hexafluorophosphate (5.0 g, 9.72 mmol) and DIPEA (5.0 mL, 29.0 mmol) were dissolved in dry DMF (20 mL) and was stirred at room temperature under N₂ atmosphere for 6 hrs. Fraction with desired product was freeze dried to obtain compound 9. 0.5 g (6.25 mmol) of compound 9 was dissolved in ethanol and mixed with 35% Pd/C, stirred for 18 hrs under H₂ atmosphere. The solution was filtered to remove Pd/C and solvent was evaporated to obtain compound 10. 0.46 g of compound 9 and trimethylsilyl bromide (TMSBr) (20.3 mL, 0.12 mmol) in dry DMF (1 mL) was stirred at RT for 12 h. The solvent was removed in rotary vapor and purified by preparative HPLC to obtain 10 (0.38 g, 5.56 mmol).

¹H NMR (400 MHz, D₂O, TMS): δ 2.64 (16H, br, CH₂NCH₂, macrocycle), 2.91 (6H, d, H₂O₃PCH₂NH), 3.21 (6H, t, NCH₂CO), 8.06 (CONHCH₂)

¹³C NMR (400 MHz, D₂O, TMS): δ 42.8 (H₂O₃PCH₂NH), 49.2 (NCH₂CH₂N), 56.8 (NCH₂CON), 58.2 (NCH₂COOH), 168.8 (CH₂CONH), 174.3 (CH₂COOH)

MS(ESI-positive) m/z = 683.20 [M-H⁺] (calculated 683.48)

3.3.3 General Procedure for preparation and characterization of lanthanide-ligand complexes

(a) Complexation of DOTA-1AmP

0.50g of the ligand dissolved in 25mL 0.1005N NaOH. Solution pH = 6.4. 5mL of an ~0.28M GdCl₃ solution was prepared in water. The Gd solution was added in increments. NaOH solution was used to keep the pH at ~6.4. The complexation was followed by HPLC. After a slight excess of Gd was added the pH was raised to 7.5 to assure complete complexation. The slight haze that was present was filtered (0.2um PVDF). SCX in the H⁺ form was added to remove any residual free Gd. The solution pH = 6.4. NaOH solution was again used to raise the pH = 7.4. The solution was freeze dried. Net 0.793g. Yield = 113% as the disodium salt. Based on the yield there is extra NaCl expected to be present. Purity by HPLC 98.8%. HPLC conditions same as the ligand.

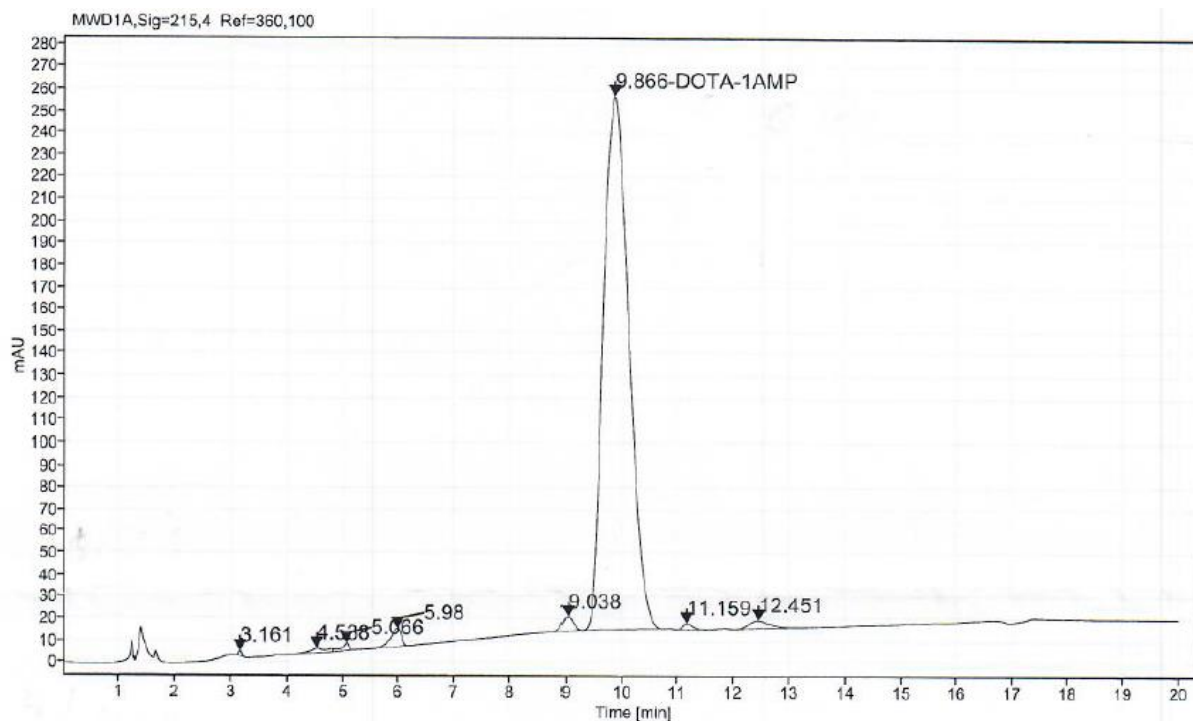
MS Gd-DOTA-1AmP - (ESI-positive) m/z = 653.09 [M-H⁺] (calculated 654.69)

(b) Complexation of DOTA-2AmP and DOTA-3AmP

The ligand (DOTA-2AmP and DOTA-3AmP) was dissolved in MilliQ grade water and mixed with a lanthanide chloride (Gd) in excess, 5-10% of stoichiometric amount. The solution pH was adjusted gradually to 8.5-9.0 by addition of 1M NaOH and stirred in room temperature for 18 hrs at 80°C. The resulted solution was agitated with excess of optimized Chelex-100(50-100 mesh) for 2 hrs to remove excess Gd³⁺ ions. The resin was removed by filtration and purified with preparative HPLC to obtain the Complex and characterized by LC-MS.

MS Gd-DOTA-2AmP (ESI-positive) m/z = 746.44 [M-H⁺] (calculated 747.71)

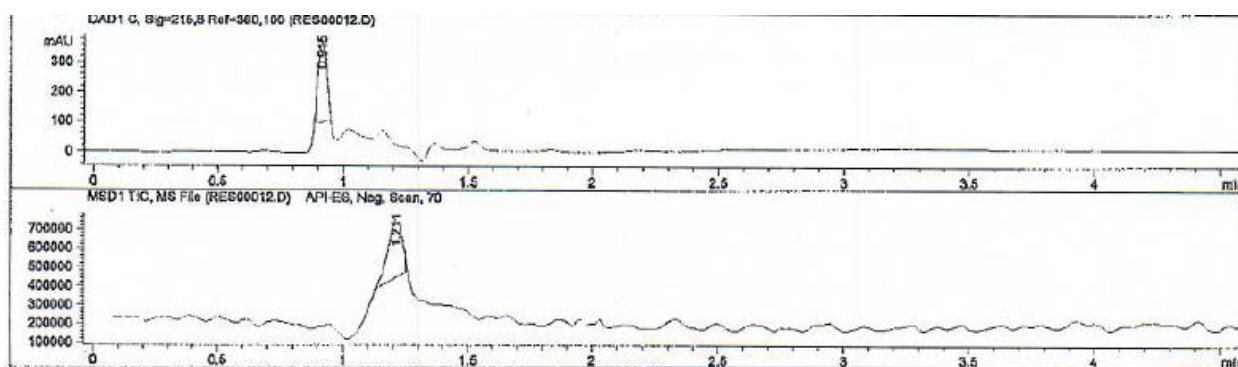
MS Gd-DOTA-3AmP (ESI-positive) m/z = 838.75 [M-H⁺] (calculated 840.73)



Signal: MWD1A,Sig=215,4 Ref=360,100

| RT [min] | Name | Peak Width | Peak Height | Area | Peak Area % |
|----------|-----------|------------|-------------|---------|-------------|
| 3.161 | | 0.06 | 2.309 | 8.5 | 0.10 |
| 4.538 | | 0.34 | 2.031 | 42.0 | 0.52 |
| 5.066 | | 0.11 | 3.427 | 30.9 | 0.38 |
| 5.980 | | 0.15 | 8.233 | 107.8 | 1.33 |
| 9.038 | | 0.22 | 6.284 | 81.9 | 1.01 |
| 9.866 | DOTA-1AMP | 0.37 | 242.174 | 7688.9 | 95.15 |
| 11.159 | | 0.43 | 2.702 | 32.0 | 0.40 |
| 12.451 | | 0.30 | 3.475 | 89.1 | 1.10 |
| Sum | | | | 8081.06 | |

Figure 3.2. HPLC profile of DOTA-1AmP



| Retention Time (LC) | LC Area | Retention Time (MS) | MS Area | Mol. Weight or Ion |
|---------------------|---------|---------------------|---------|--------------------|
| 0.915 | 555 | - | - | |
| - | - | 1.211 | 1258701 | 704.20 I |
| | | | | 683.20 I |
| | | | | 682.15 I |
| | | | | 520.75 I |
| | | | | 384.85 I |
| | | | | 248.95 I |
| | | | | 226.90 I |
| | | | | 205.00 I |
| | | | | 154.90 I |

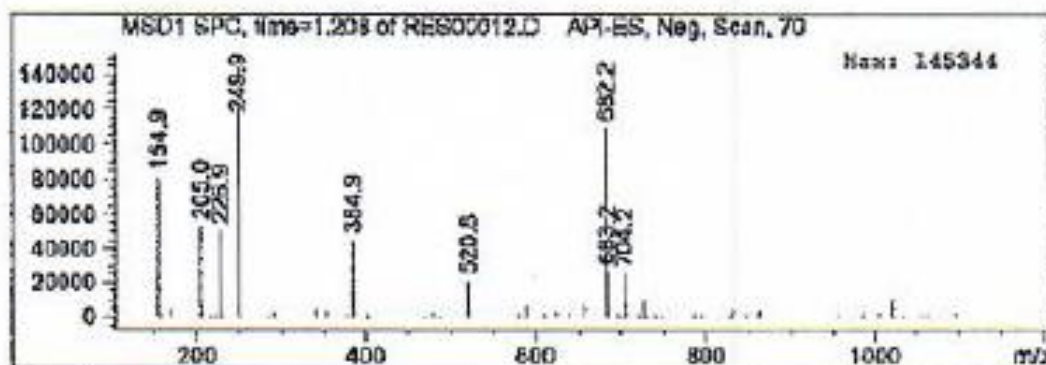
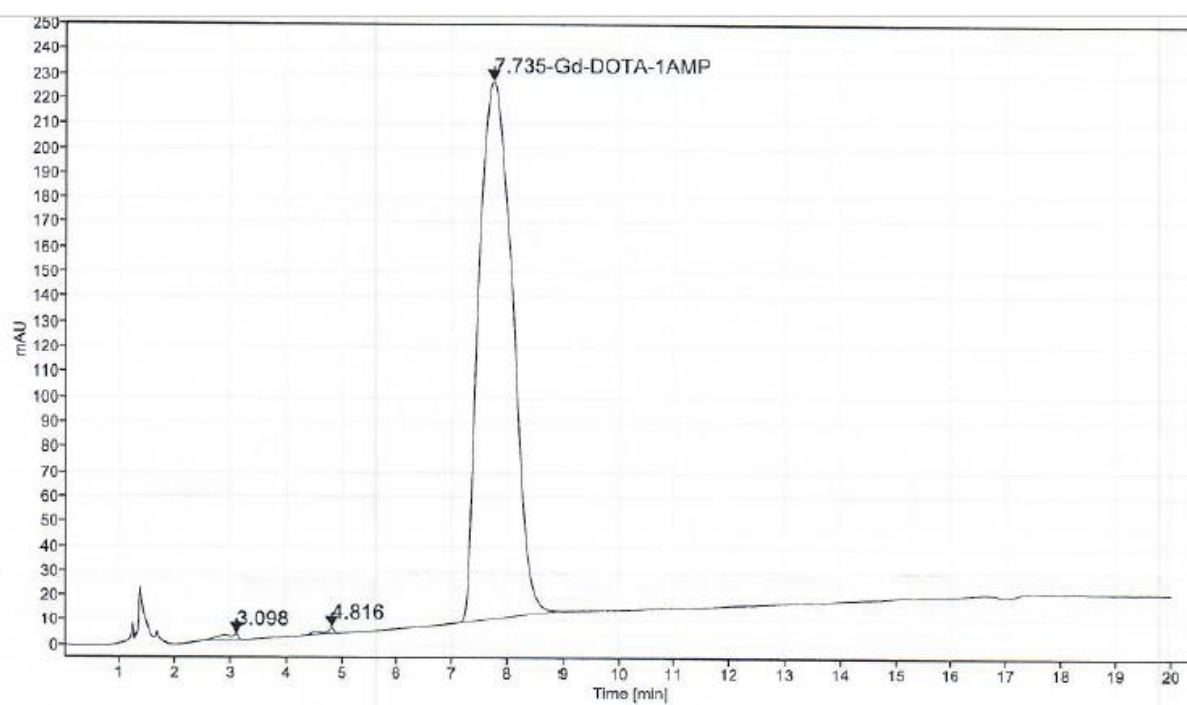


Figure 3.3. LC-MS profile of DOTA-3AmP



Signal: MWD1A, Sig=215,4 Ref=360,100

| RT [min] | Name | Peak Width | Peak Height | Area | Peak Area % |
|----------|--------------|------------|-------------|---------|-------------|
| 3.098 | | 0.26 | 2.429 | 53.8 | 0.59 |
| 4.816 | | 0.13 | 2.402 | 26.8 | 0.29 |
| 7.735 | Gd-DOTA-1AMP | 0.49 | 216.516 | 9094.1 | 99.12 |
| Sum | | | | 9174.68 | |

Figure 3.4. HPLC profile of Gd-DOTA-1AmP

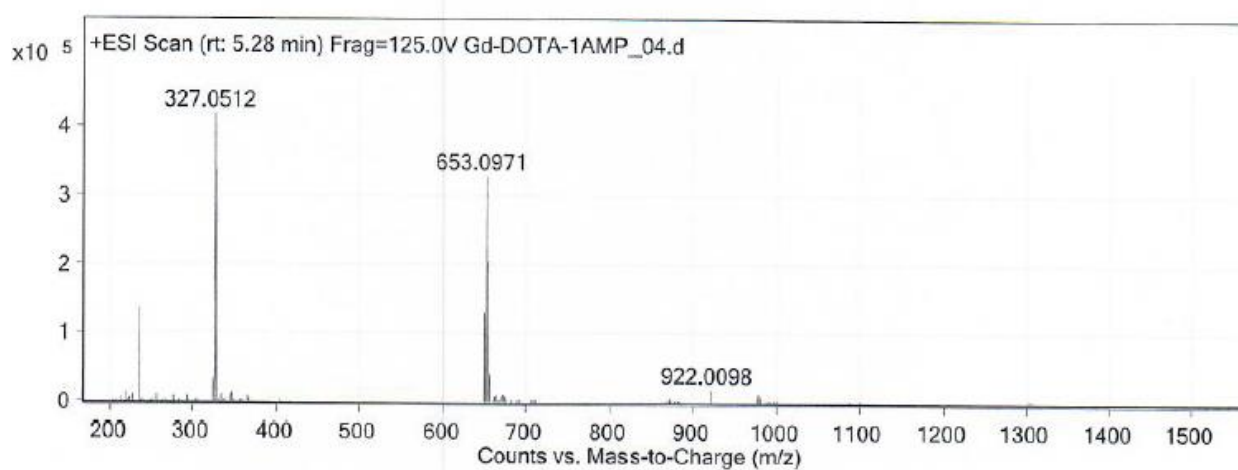
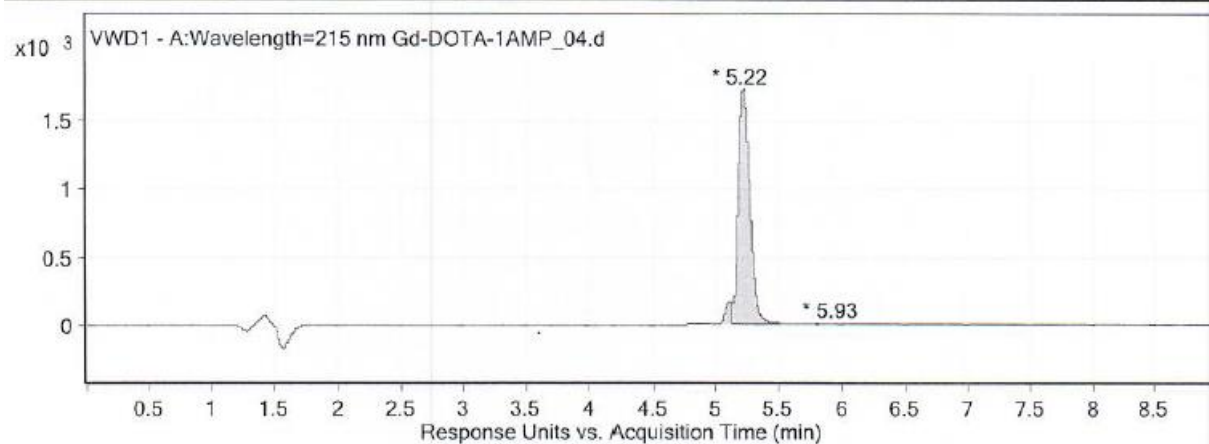
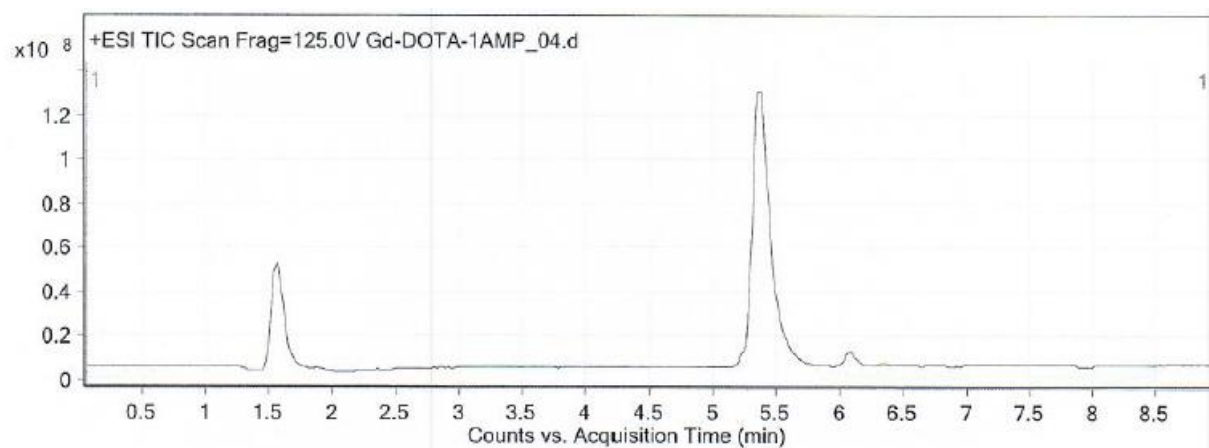


Figure 3.5. LC-MS of Gd-DOTA-1AmP Complex

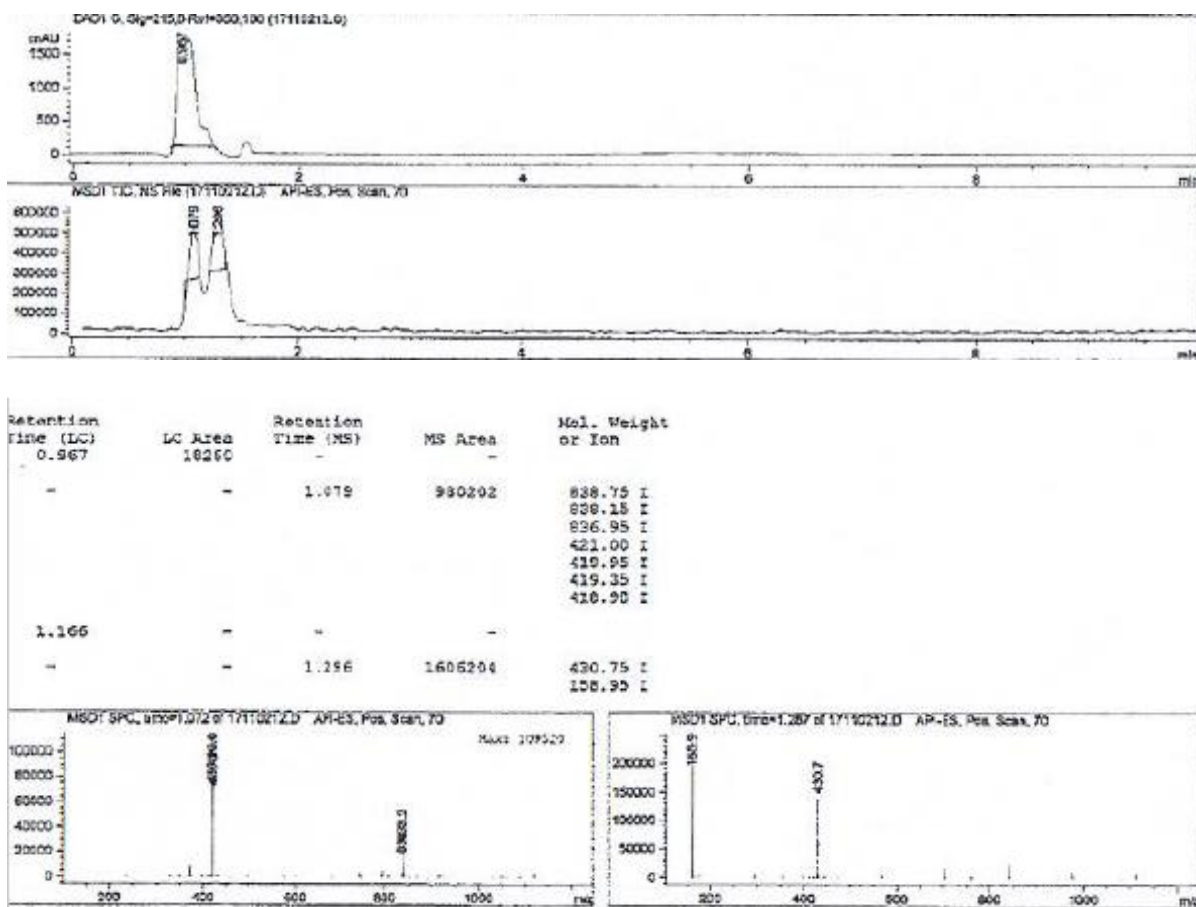


Figure 3.6. LC-MS of Gd-DOTA-3AmP Complex

3.3.4 Relaxivity Measurements

(a) Relaxivity Measurements at 0.5 T

(b) Longitudinal relaxivity values were measured in MRS-6 NMR analyzer at 20 MHz and determined from the slope of the line of $1/T_1$ versus the concentration of Gadolinium. These relaxivity data were collected by starting with a 0.5 mM solution of Gd-complex (Gd-DOTA-1AmP, Gd-DOTA-2AmP, Gd-DOTA-3AmP). Initial pH of sample was adjusted to pH~2 with addition of 1M hydrochloric acid. For each T_1 measurement, pH was raised

by the addition of small quantities of 1M Lithium Hydroxide (LiOH was chosen due to smaller size of ion). Each measurement was recorded after equilibration of 10 min of sample at 310 K. T_1 measurements were made at same temperature using warm air blower.

(c) Fitting of Relaxivity Measurements at 0.5 T

The point of inflection was calculated at a point where, $d^2y/dx^2 = 0$, for the relaxivity values of GdDOTA-1AmP as reported previously.⁸ Equations were adjusted as required. The common logistic function was used in this model.

$$f(x) = \frac{L}{1 + e^{-k(x-x_0)}}$$

e = the natural logarithm base (Euler's number),

x_0 = the x -value of the sigmoid's midpoint,

L = the curve's maximum value, and

k = the logistic growth rate or steepness of the curve

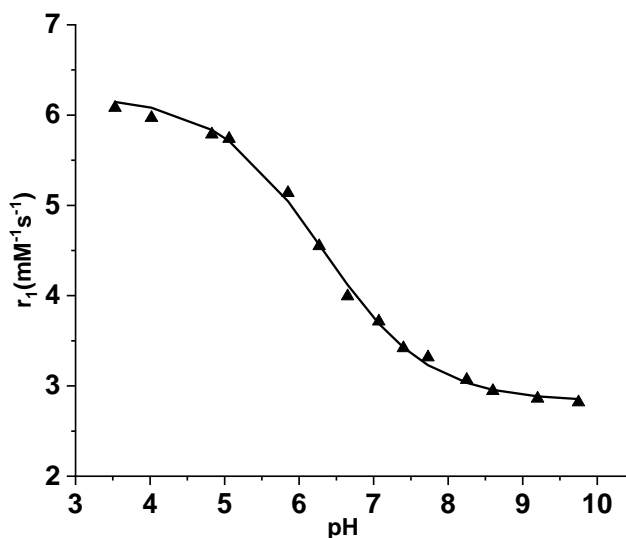


Figure 3.7. Fitted relaxivity curve as a sigmoidal function (solid line) and data points (triangles).

(d) Relaxivity Measurements at 9.4 T

Longitudinal relaxivity values were measured in Bruker AVII NMR at 400 MHz (310K) and determined from the slope of the line of $1/T_1$ versus the concentration of Gadolinium.

Samples were prepared as described above.

3.3.5 Relaxivity Measurements with Ca^{2+}

Longitudinal relaxivity data were obtained in a solution of 0.5 mM of Gd-DOTA-1AmP with 2.5 mM CaCl_2 , 5 mM KCl, 135 mM NaCl. Each T_1 measurement was recorded as described above at 20 MHz.

3.3.6 Determination of q value by Luminescence decay studies

Luminescence measurements were carried out in a F920 Edinburgh fluorescence spectrometer. Luminescence-decay curves of luminescence from Eu-DOTA-1AmP in water and deuterated water (D_2O). The decay life times (τ_H , τ_D) were calculated by fitting the decay curves. The q value was determined with the differences between luminescence decay rates measured in water (H_2O) and deuterated water (D_2O) using following equation introduced by Parker *et al.*³¹

$$q = 1.20 (\tau_H^{-1} - \tau_D^{-1} - k_{XH})$$

τ_H, τ_D - decay life times in H_2O and D_2O

k_{XH} - correction for CONH oscillators

3.3.7 ^{17}O NMR measurements to Determine τ_M

^{17}O NMR experiments were performed at 9.4 T on a Bruker AVANCE III NMR spectrometer and temperature was regulated by air flow controlled by a Bruker VT unit. The samples ($[\text{Gd}^{3+}] = 20.1$ mM) were prepared in ^{17}O enriched water (10%) with the pH being adjusted to 6, 7, and 9. The sample was loaded into 80 μL spherical bulb (Wilmad-Lab Glass, Vineland, NJ) and placed inside a 5 mm NMR tube. Longitudinal relaxation rates ($1/T_1$) were obtained by the inversion recovery method, and transverse relaxation rates ($1/T_2$) were obtained by the Carr–Purcell–Meiboom–Gill spin echo technique. The acidified water (pH = 3.0) containing 10% enriched ^{17}O water was used as a reference for the measurements. The corresponding fittings were performed with the Scientist 3.0 software (Micromath®).

3.3.8 Analysis of ^{17}O NMR Data

^{17}O NMR data have been analyzed within the framework of Solomon-Bloembergen-Morgan theory. Data was analysed similar to theory in Chapter 2.

3.3.9 Potentiometry

In a typical experiment, approximately 0.1 mmol of ligand or complex was added to a 100 mL jacketed reactor kept at 25°C. The solid was dissolved in 25.00 mL 2.00 M KCl. Standardized acid and water were added to obtain a final volume of 50.0 mL. Nitrogen was bubbled through the solution. Electrodes were calibrated by determining a value of E_0 from the titration of standard HCl. Potentials in millivolts were measured as standard KOH was added in small increments manually using a burette. Values of pH were then calculated using the measured potentials and the E_0 value. The program BEST was used to determine the equilibrium constants.

(a) Determination of Stability constant of Gd-DOTA-1AmP

The stability constant for Gd-DOTA-1AmP as well as KMHL was determined by the out-of-cell¹⁰ method due to slow equilibrium. Complex solutions of 0.002M were prepared in 1.0M KCl. The pH was adjusted using KOH. The samples were stored at 60°C for two weeks to speed up equilibration. Weight loss was $\leq 1\%$ over the two weeks. Nine different complex solutions covering the pH range of 1.8 – 2.1 were used. HPLC was used to analyze the complex at pH = 2.0 over time. No degradation was obvious over three weeks at 60°C.

(b) Determination of Stability constants of coordinated water molecules to Gd-DOTA-1AmP

The stability constant of water molecules coordinated to the complex were also determined by the out-of-cell method due to slow equilibrium.³² A solution of the complex was prepared in a 50mL volumetric flask. Solid KCl was added to make the ionic strength 1.0M. The solution was divided into 24 vials containing 2.00mL. A pipette was used to add various volumes of standardized base. The solutions were placed in an oven at 60°C for ten days. After 10 days the solutions were all clear and colorless. No precipitate indicating the formation of Gd(OH)₃ was observed. After the vials were allowed to equilibrate to room temperature, the pH was measured. A pH range of 8.0 to 9.5 was used. It was not possible to fit the data above pH = 9.5 so that data was not used.

3.3.10. ³¹P NMR titrations

A ³¹P NMR titration was performed in the acidic region for the determination of the lowest phosphonate protonation constant of DOTA-1AmP. The measurements were performed at 25°C in 1.0 M KCl in H₂O. A reference solution of Na₃PO₄ in D₂O/NaOD was placed in a coaxial tube.

A series of solutions were prepared using a ligand solution, water, standardized 6.16N HCl, and 2.00M KCl. The overall ionic strength was kept constant at 1.0M. The solutions covered a pH range of -0.25 to 2.74. A plot of observed chemical shift versus calculated pH generated a sigmoidal curve. The pK_a of the phosphonate is at the pH of the inflection point. A value of 0.85 was obtained.

3.3.11 In-vitro Phantom MR Images

In vitro phantom, MR images were obtained using 0.5 mM Gd-DOTA-1AmP at different pH values. Samples were prepared as described in the relaxivity measurement experiments. Image T₁ values were obtained at 400 MHz (9.4 T) in Varian MRI scanner microimaging system using a spin-echo multislice(SEMS) sequence. Image analyzed were carried out using ImageJ software provided by the National Institute of Health, USA.

3.4 Results and Discussion

The pH *versus* water proton relaxivity (r_1) profiles of GdDOTA-4AmP and the three new derivatives reported here are shown in Figure 2.1. Interestingly, the profiles for the three agents containing more than one phosphonate group (4AmP, 3AmP, and 2AmP) have similar shapes while the profile for 1AmP is distinctly different. 4AmP, 3AmP and 2AmP all show a maximum r_1 near pH 6.5 with a decrease in r_1 at both at higher and low pH values. For 4AmP, this behavior paralleled step-wise protonation of the four phosphonate groups beginning near pH 8 and ending around pH 5 (the pK_a's of the four phosphonate groups in GdDOTA-4AmP are 7.20, 6.47, 6.03, and 5.36 measured at 25°C).²³ These changes in r_1 were traced to an increase in the rate of proton exchange between a slowly exchanging, Gd-bound water molecule with bulk water protons

catalyzed by the appended monoprotonated phosphonate groups ($-\text{PO}_3\text{H}^-$). This provides a convenient mechanism for increasing the rate of proton exchange into bulk solvent without necessarily increasing the rate of water molecule exchange. The similar shapes and magnitude of r_1 in the curves for 4AmP, 3AmP, and 2AmP suggest that a larger number of appended protonated phosphonates is not necessarily better for initiating this catalytic proton exchange and, in fact, more may be detrimental to some extent. The fact that the r_1 relaxivity of all three compounds is higher at pH 8-9 (compared to 1AmP) where the phosphonate groups are essentially fully deprotonated likely reflects a higher molecular weight and slower overall molecular tumbling rates of these complexes. In fact, during HPLC purification of GdDOTA-2AmP, we detected small amounts of dimers or larger oligomers which could explain the higher r_1 value measured for this compound at pH 8.5.

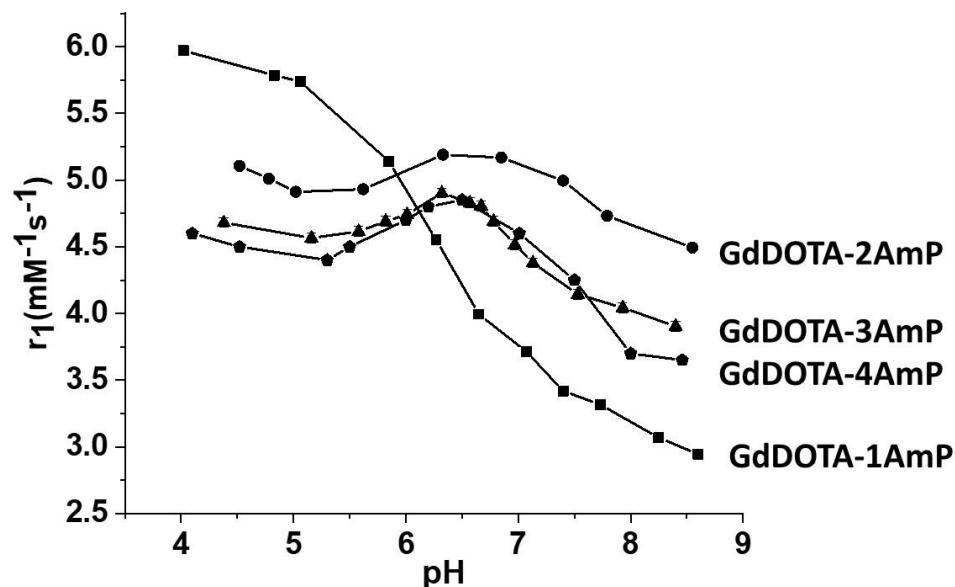


Figure 3.8. Effect of solution pH on the relaxivity of GdDOTA-1AmP (squares), GdDOTA- 2AmP (circles), GdDOTA- 3AmP (triangles) and GdDOTA- 4AmP (pentagons) recorded at 37 °C and 20 MHz with 0.5 mM of agent.

To our surprise, the r_1 versus pH curve for GdDOTA-1AmP displayed a quite different behavior. In this compound, protonation of the single phosphonate ($pK_a = 6.07$) favorably shifts the entire curve to the left and there is a smooth, almost linear relationship of r_1 with pH between pH 7.4 and 6, the range of greatest interest for physiological measurements. The r_1 of this compound is especially low at pH 8.5 ($3.1 \text{ mM}^{-1}\text{s}^{-1}$) and increases smoothly until near pH 4 where it reaches a maximum of $5.9 \text{ mM}^{-1}\text{s}^{-1}$. Given that the dynamic range (Δr_1) of GdDOTA-1AmP at 37°C is about 3-fold higher than that of GdDOTA-4AmP, the sensitivity of this agent for imaging tissue pH should be substantially improved.

To determine whether biological amounts of Ca^{2+} might impact the r_1 versus pH relationship, the relaxivity profile was recorded in a solution that stimulates *in-vivo* conditions (2.5mM CaCl_2 , 5 mM KCl, 135 mM NaCl) (Figure 3.9).

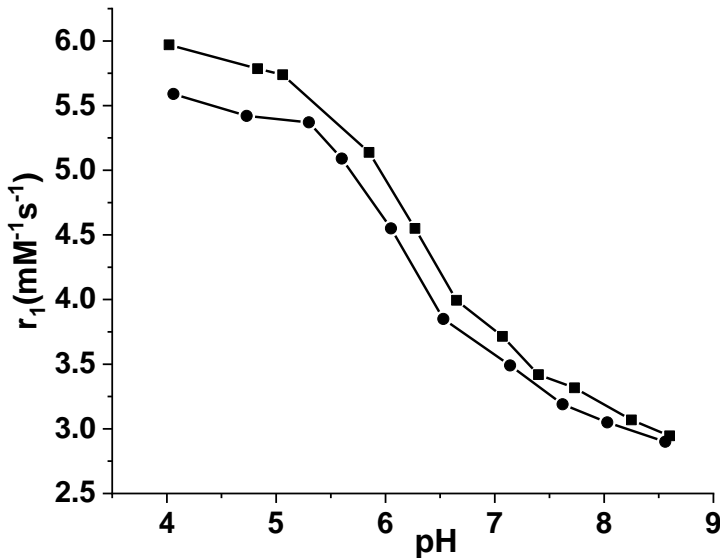


Figure 3.9. Effect of solution pH on the relaxivity of Gd-DOTA-1AmP (Squares) and Gd-DOTA-1AmP in the presence of 135 mM NaCl, 5 mM KCl, and 2.5 mM CaCl_2 (Circles). Measurements were recorded at 37°C and 20 MHz with 0.5 mM Gd-DOTA-1AmP.

The relaxivity profile was similar to that obtained in the absence of the cations, with a small shift of inflection point from pH 6.3 to 6.0. This demonstrates that the presence of the endogenous ions should not interfere with the use of GdDOTA-1AmP as a pH sensor. High-resolution NMR was recorded for analogous EuDOTA-1AmP complexes. These NMR data show that two coordination isomers are present in solution, a square antiprism (SAP) and twisted square antiprism (TSAP) structure in an approximate 78:22 ratio (Figure 3.10). This indicates that GdDOTA-1AmP likely also exists as a mixture of coordination isomers in solution with higher fraction of SAP isomer.

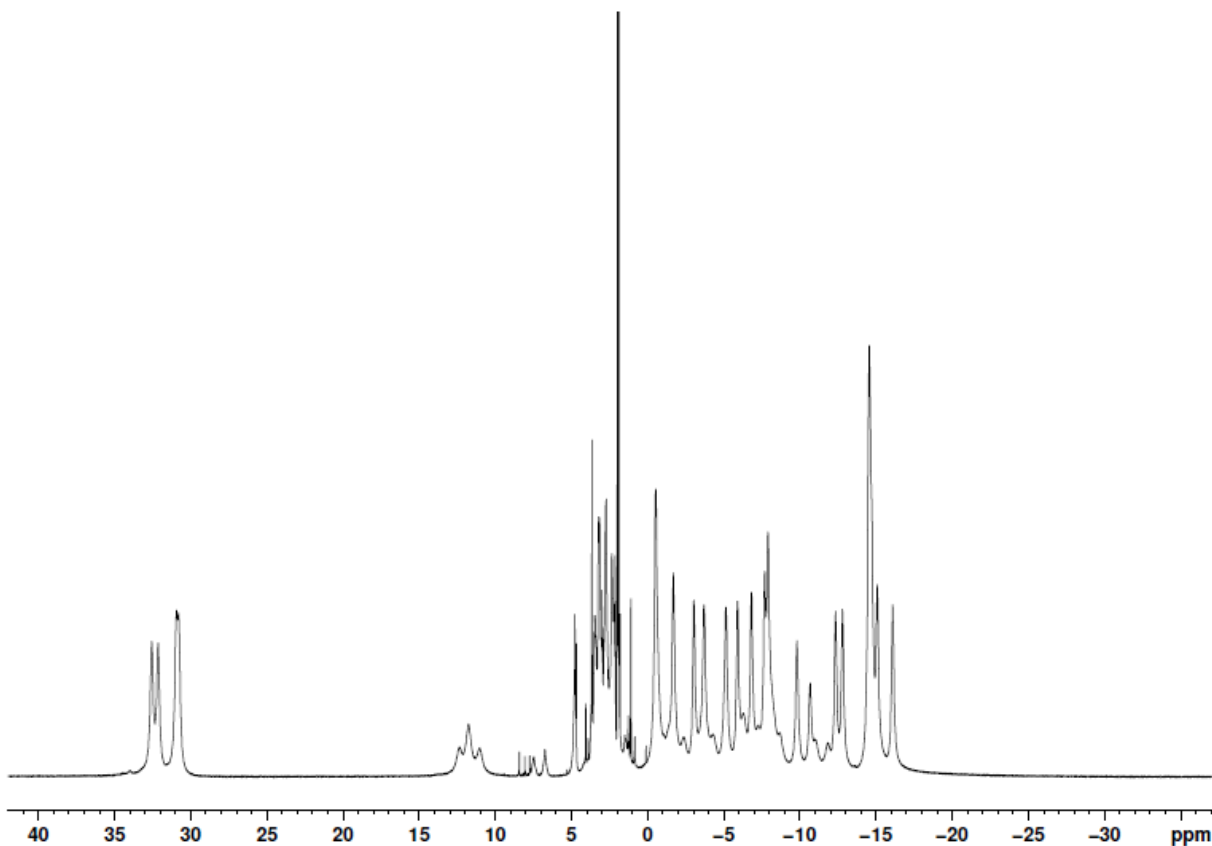


Figure 3.10. ^1H NMR spectrum of EuDOTA-1AmP (80 mM) showing square antiprism (SAP) and twisted square antiprism (TSAP) structure in an approximate 78:22 ratio at pD \sim 6.5 in D_2O at 400 MHz.

Luminescence decay measurements were studied as a simple and fast technique to determine the pH dependence of the inner sphere water coordination number (q) of the Eu-complex.²⁵ The data suggest that number of water molecules (q) of the complex in aqueous solution is 1 ± 0.1 and independent of pH (Figure 3.11 and Table 3.1).

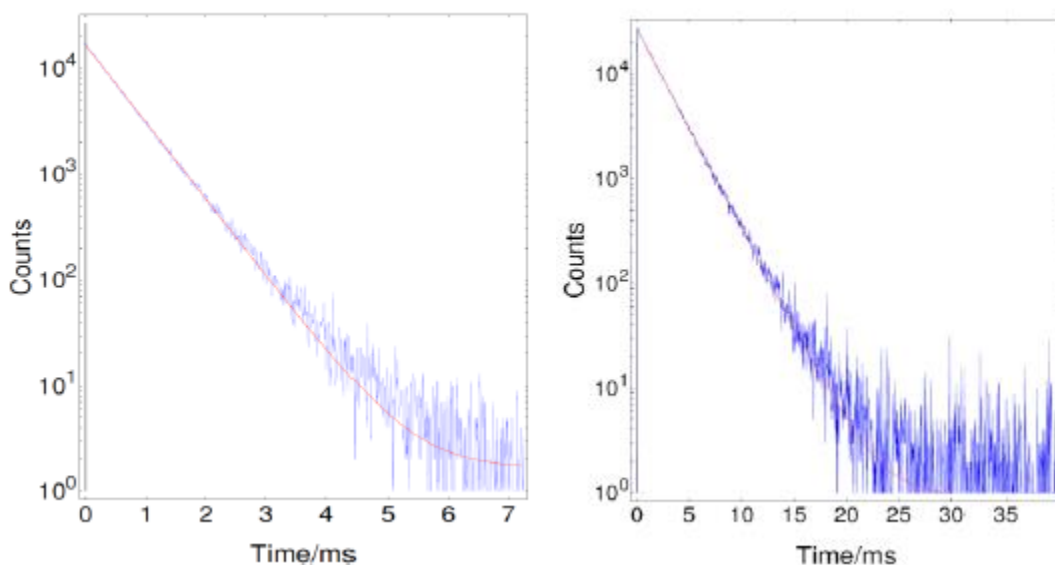


Figure 3.11. Decay curves of luminescence of 20 mM Eu-DOTA-1AmP in H₂O (left) and D₂O (right). $\lambda_{\text{ex}} = 394 \text{ nm}$, $\lambda_{\text{em}} = 595 \text{ nm}$.

Table 3.1. Measured q values at different pH at 25°C

| pH | q |
|-----|-----|
| 6.0 | 1.2 |
| 9.0 | 1.1 |

Therefore, the origin of the pH dependent relaxivity profile must reflect a change in either the rate of water molecule exchange or proton exchange.^{26,27} To differentiate between these two possibilities, rate of water molecule exchange was determined by measuring the temperature-

dependent T_{2s} by ^{17}O NMR (Table 3.2). A fit of those data to theory showed that water molecule exchange was no more than a factor of 2 faster at pH 6 than at pH 9. This small change is not enough to account for the increases in r_1 we observe upon lowering the pH for GdDOTA-1AmP.

Table 3.2. Best-fit parameters obtained for Gd-DOTA-1AmP from analysis of ^{17}O NMR data.

| | Gd-DOTA-1AmP | | |
|--|---------------------|---------------|---------------|
| pH | 9 | 7 | 6 |
| k_{ex}^{298} [10^6 s^{-1}] | 1.0 ± 0.1 | 1.2 ± 0.2 | 1.8 ± 0.2 |
| t_m [μs] | 1.0 ± 0.1 | 0.8 ± 0.1 | 0.5 ± 0.1 |

To investigate the involvement of amino-phosphonate arm in initiating the pH-dependent relaxivity profile, the protonation constants of the ligand and complex were determined by potentiometric titrations. Seven protonations were identified by pH potentiometry and eighth was determined by ^{31}P NMR. The two highest constants are attributed to protonation of two macrocyclic N-atoms in the macrocycle (Table 3.3).^{28,29} The third protonation constant (6.53) reflects protonation of the phosphonate³⁰ while the next (4.25) corresponds to protonation of the acetate group *trans* to the aminophosphonate arm again based upon comparison to other similar structures.³¹ The fifth and sixth protonation constants correspond to the two remaining acetate arms on the macrocyclic ring while the constant at 1.61 corresponds to another N-atom in the macrocyclic ring. The assignment of these protonation constants lies in the range of values reported in prior studies.²⁷⁻³¹

Table 3.3. Protonation Constants of DOTA-1AmP at 25 °C in 1.0 M KCl

| | p <i>K</i> _a |
|-------------|-------------------------|
| Log K_1^H | 10.12 |
| Log K_2^H | 9.53 |
| Log K_3^H | 6.53 |
| Log K_4^H | 4.25 |
| Log K_5^H | 2.66 |
| Log K_6^H | 1.95 |
| Log K_7^H | 1.61 |
| Log K_8^H | 0.85 |

The stability constant of GdDOTA-1AmP ($\log K_{ML} = 25.4$) was determined by potentiometry using the out-of-cell technique commonly used for complexation reactions that require some time to fully equilibrate.³² This value is comparable to the stability reported for GdDOTA^{31,33} and slightly higher when compared with stability constants reported for related ligands.²⁸⁻³³ The K_{MHL} constant corresponds to the first protonation of the single phosphonate moiety. The value is slightly lower in comparison to the value measured for the ligand alone. The lowest protonation constant ($K_{MLH2} = 1.74$) likely reflects protonation on one of the Gd-bound carboxyl groups. In addition to these values, two higher constants likely corresponding to formation of a hydroxo complex ($\log K_{ML(OH)} = 8.9$) and deprotonation of the amide group ($\log K_{ML(OH)H^{-1}}$) were needed to fit the entire titration curve.^{34,35} Thus, the sigmoidal dependence of r_1 with pH must largely reflect the first protonation step on the phosphonate moiety on the pendant arm. The inflection point (pH 6.3)

observed in the relaxivity curve corresponds reasonably close to the first protonation step $\text{PO}_3^{2-} \rightarrow \text{PO}_3\text{H}^-$ ($\text{Log}K_{\text{MLH}2} = 6.07$).

Table 3.4. Stability constant and protonation constants of GdDOTA-1AmP at 25 °C in 1.0 M KCl.

| | Equil. constant |
|--|-----------------|
| $\text{Log}K_{\text{ML}}$ | 25.4 |
| $\text{Log}K_{\text{MHL}}$ | 6.07 |
| $\text{Log}K_{\text{MLH}2}$ | 1.74 |
| $\text{Log}K_{\text{ML}(\text{OH})}$ | 8.90 |
| $\text{Log}K_{\text{ML}(\text{OH})\text{H}^-}$ | 9.50 |

A speciation diagram was generated using these protonation constants (Figure 3.12) and this was overlaid with the r_1 versus pH relaxivity curve. The near sigmoidal relaxivity curve correlates nicely with protonation of the single appended phosphonate group consistent with the monoprotonated phosphonate group acting as a general acid catalyst for initiating proton exchange of the Gd-bound water protons. The phosphonate on the single amide side-chain is positioned nicely to form a H-bond structure with the Gd-bound water molecule. Upon protonation of the phosphonate, it is envisioned that this proton forms a H-bond with the single lone pair of electrons of the water oxygen. This proton is relaxed rapidly by the paramagnetic Gd^{3+} ion before exchanging with other second-sphere water protons. This catalytic transfer of protons is reminiscent of the catalytic mechanism of proton exchange in the serine protease enzymes.^{36,37} Given that only a single lone pair of electrons is available on the Gd-bound water molecule, it is

reasonable to assume that a single phosphonate group is most efficient at catalyzing this proton exchange network. This seems to nicely explain the unique behavior of GdDOTA-1AmP among this class of pH sensitive agents (Figure 3.13).

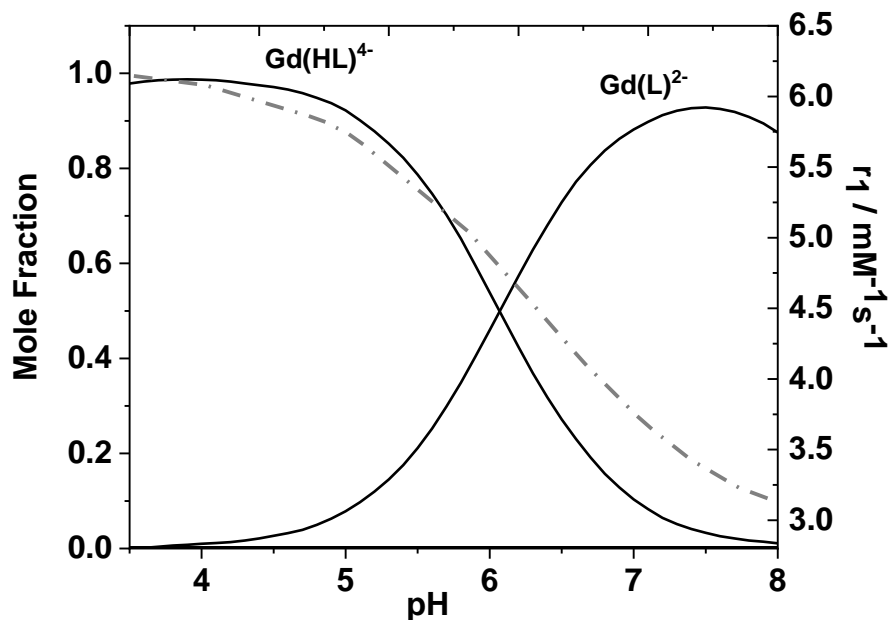


Figure 3.12. Longitudinal relaxivity pH profile of Gd-DOTA-1AmP (37 °C, 20 MHz, 0.5 mM) (Dashed line) laid over the speciation diagram of Gd-DOTA-1AmP.

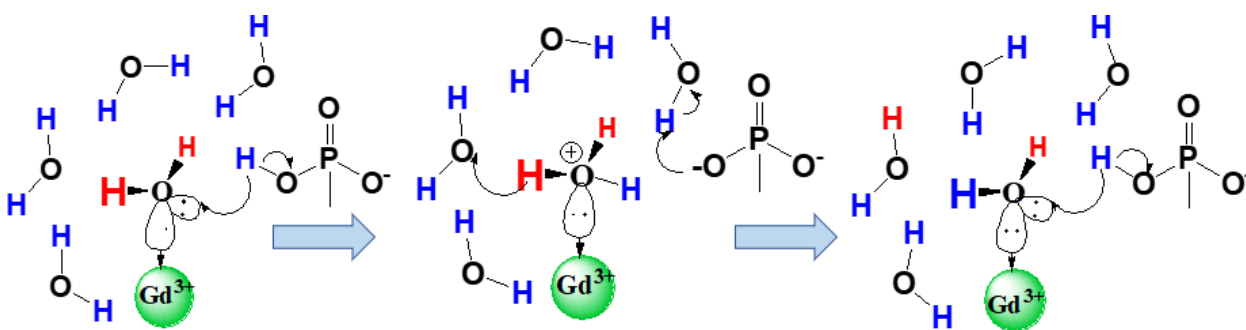


Figure 3.13. Schematic representation prototropic effect described, viewed down the Gd-OH₂ axis, of how the phosphonates in GdLH⁻ transfer protons between the coordinated water molecule and the bulk solvent. The relaxed protons of the coordinated water molecule (shown in red) and replaced by unrelaxed protons from the bulk water (shown in blue).

Finally, we evaluated the applicability of GdDOTA-1AmP as a pH probe for MRI. T_1 -weighted images of a phantom containing 0.5 mM solutions of GdDOTA-1AmP at different pH values were acquired at 9.4 T (Figure 3.14). The images have a trend very similar to the pH dependence relaxivity profile of GdDOTA-1AmP with lower T_1 values at acidic pH and higher T_1 values at basic pH.

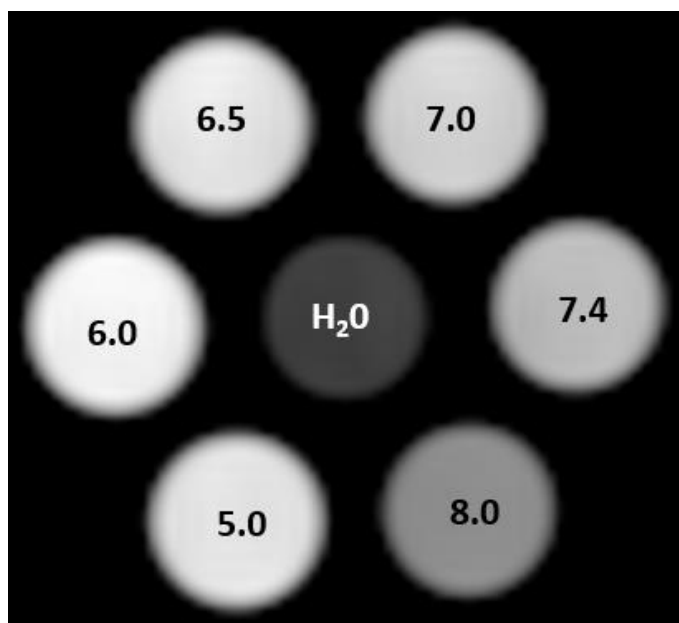


Figure 3.14. T_1 - Weighted phantom MR images. Repetition time (TR) = 2500.0 ms; echo time (TE) = 10.0 ms; Data Matrix = 256 x 256. Images and T_1 values were obtained at 400 MHz (9.4T).

3.5 Conclusion

In summary, GdDOTA-1AmP displays a surprisingly simple sigmoidal pH-dependent relaxivity profile in comparison to the other phosphonate complexes in the series. The relaxivity (r_1) decreases almost linearly from pH 6 to 8 making GdDOTA-1AmP an attractive pH sensor for imaging extracellular pH by MRI. Of course, this would still require a separate measure of agent concentration either by co-infusion of a T_2 agent³⁸ or a PET probe.³⁹ The protonation constants of

Gd-complex and ligand suggest the pH response of this agent originates with catalytic exchange of protons rather than dissociation and exchange of the entire water molecule. During this process monoprotonated phosphonate acts as an acid to accelerate proton exchange from the single Gd-bound water molecule to bulk solvent. This illustrates that even single amino-phosphonate side chain appears to have significant impact on catalysis of prototropic exchange.

REFERENCES

1. White, A.; Handler, P.; Smith, E. L., Principles of Biochemistry. McGraw-Hill, Kogakusha: New York; 1968.
2. Gillies, R. J.; Raghunand, N.; Garcia-Martin, M. L.; Gatenby, R. A., *IEEE Eng. Med. Biol. Mag.* 2004; 23: 57–64.
3. Zang, X.; Lin, Y.; Gillies, R.J., *Journal of nuclear medicine: official publication, Society of Nuclear Medicine*, 2010, 51, 1167–1170.
4. Sennoune Souad, R.; Luo, D.; Martinez-Zaguilan, R., *Cell Biochem. Biophys.* 2004, 40, 185-192.
5. Tannock, I. F.; Rotin, D., *Cancer Res.* 1989, 49, 4373-4380.
6. Vaupel, P.; Kallinowski, F.; Okunieff, P., *Cancer Res.* 1989, 49, 6449-6453.
7. Wike-Hooley, J. L.; Haveman, J.; Reinhold, J. S., *Radiother. Oncol.* 1984, 2, 343-349.
8. Perez-Mayoral, E.; Negri, V.; Soler-Padros, J.; Cerdan, S.; Ballesteros, P., *Eur. J. Radiol.* 2008, 67, 453-458.
9. Wike-Hooley, J.L.; Haveman, J.; Reinhold, H.S., *RadioTher. Oncol.* 1984, 2, 343-366.
10. Wojtkowiak, J.W.; Verduzco, D.; Schram, K.; Gillies, R.J., *Mol. Pharm.* 2011, 8, 2032-2038.
11. Sun, P.Z.; Longo, D.L.; Hu, W.; Xiao, G.; Wu, R.; *Phys. Med. Biol.*, **2014**, 59, 4493-4504.
12. van Sluis, R.; Bhujwalla, Z. M.; Raghunand, N.; Ballesteros, P.; Alvarez, J.; Cerdan, S.; Galons, J. P.; Gillies, R. *J. Magn. Reson. Med.* **1999**, 41, 743–750.
13. Frullano, L.; Catana, C.; Benner, T.; Sherry A.D.; Caravan, P, *Angew Chem Int Ed.*, 2010, 49, 2382-2384.
14. Pierre, V.C.; Allen, M.J.; Caravan, P.J., *Biol.Inorg. Chem.* 2014, 19, 127-131.
15. Zhang, S.; Zhou, K.; Huang, G.; Takahashi, M.; Sherry, A.D.; Gao, J., *Chem Commun.*, 2013, 49, 6481-6420.
16. Wang, X.; Wu. Y.; Soesbe, T.C.; Yu, J.; Zhao, P.; Kiefer, G.E.; Sherry, A.D., *Angew, Chem. Int. Ed.Engl.* 2015, 54, 8662-8664.

17. Toth, E.; Bolskar, R.D.; Borel, A.; Gonzalez, G.; Helm, L.; Merbarch, A.E.; Sitharam, B.; Wilson, L.J., *J.Am.Chem.Soc.* 2005,127,799-805.
18. Wang, X.; Wu, Y.; Soesbe, T.C.; Yu.J.; Zhao, P.; Kiefer, G.E.; Sherry, A.D., *Angew. Chem. Int. Ed. Engl.*, 2015, 54, 8662-8664.
19. Huang, C.H.; Hammell, J.; Ratnakar, S.J.; Sherry, A.D.; Morrow, J.R., *Inorg. Chem.* 2010, 49, 5963-5970.
20. Longo, D.L.; Zhe Sun, P.; Consolino, L.; Michelotti, F.C.; Uggeri, F.; Aime, S., *J.Am.Chem.Soc.*, 2014, 136, 14333–14336.
21. Gianolio, E.; Maciocco, L.; Imperio, D.; Giiovenzana, G.B.; Simonelli, F.; Abbas, K.; Bisi, G.; Aime, S., *Chem. Commun.*, 2011, 47, 1539-1541.
22. Raghunand, N.; Howison, C.; Zhang, S.; Sherry, A.D.; Gillies, R.J., *Magnetic Resonance in Medicine*. 2003, 49, 249-257.
23. Kalman, F.K.; Woods, M.; Caravan, P.; Jurek, P.; Spiller, M.; Tirisco, G.; Kiraly.; Brucher, E.; Sherry, A.D., *Inorg. Chem.* 2007, 46, 5260-5270.
24. Zhang, S.; Merritt, M.; Woessner, D.E.; Lenkinski, R.E.; Sherry, AD., *Acc. Chem, Res.*2003, 36,783-790.
25. Beeby, A.; Clarkson, I.M.; Dickins, R.S.; Faulkner, S.; Parker, D.; Royle, L.; de Sousa, A.S.; Williams, J.A.G.; Woods, M., *J.Chem.Soc. Perkin Trans.2*. 1999, 0, 493-504.
26. Aime, S.; Botta, M.; Fasano, M.; Terreno, E., *Acc.Chem.Res.*, 1999, 32, 941-949.
27. Aime, S.; Barge, A.; Botta, M.; Parker, D.; De Sousa, A.S., *J.Am.Chem.Soc.*, 1997, 119, 4767-4798.
28. Krchova, T.; Kotek, J.; Jirak, D.; Havlickova, J.; Ciscrova, I.; Hermann, P., *Dalton Trans.*, 2013, 42, 15735-15747.
29. Bianchi, A.; Calabi, L.; Giorgi, P.; Losi, P.; Mariani, P.; Kotek, J., *Dalton Trans.*, 2016, 45, 3486-3496.
30. Popov, K.; Ronkkomak, H.; Lajunen, L. J., *Pure. Appl. Chem.* 2001, 73, 1641-1677.
31. Krchova, T.; Herynek, V.; Galisova, A.; Blahut, J.; Hermann, P.; Kotek, J., *Inorg. Chem.*, **2017**,56,2078-2091.

32. Martell, A.E.; Smith, R.M.; Motekaitis, R.J., NIST Critically Selected Stability Constants of Metal complexes (Version 7); Texas A and M University: College Station, TX.
33. Pasha, A.; Tircso, G.; Benyo, E.T.; Brucher, E.; Sherry, A.D., *Eur J Inorg Chem.* **2007**, 27, 4340–4349.
34. Bars, C.F.J; Mesner, R.E., John Wiley and Sons, New York, 1976.
35. Ali, M.M.; Woods, M.; Caravan, P.; Opina, A.C.L.; Spiller, M.; Feltinger, J.C.; Sherry, A.D.; *Chem. Eur.J.*, **2008**, 14, 7250- 7258.
36. Blow, D.M.; Birktoft, J.J.; Hartley, B.S., *Nature*, **1969**, 221, 37-340.
37. Markley, J.L.; Ibanez, I.B., *Biochemistry*, **1978**, 17, 4627-4640.
38. Zhang, L.; Martins, A.F.; Zhao, P.; Wu, Y.; Tircso, G.; Sherry, A.D., *Angew, Che. Int. Ed.* **2017**, 56, 16626-16630.
39. Frullano, L.; Catana, C.; Benner, T.; Sherry, A.D.; Caravan, P., *Angew Chem Int Engl.*, 2010, 49, 2382-2384.

CHAPTER 4

FUTURE PERSPECTIVES

In this dissertation, we presented the development and optimization of two different smart MRI probes for imaging extracellular Cu^{2+} levels and for imaging pH *in-vivo*. In chapter 2, we described the synthesis and characterization of GdL1, a copper responsive Gd-based contrast agent. The *in-vitro* properties of this agent have been well characterized and the agent was used to visualize excess Cu^{2+} in mouse liver to demonstrate the potential utility of this agent for use in clinical studies. Going beyond this simple *in-vivo* experiments, we would like to use our probe for imaging disease. In Wilson's disease, a mutation in ATP7b protein causes loss of function and an increase tissue levels of Cu^{2+} in the liver. Similarly, elevated serum and tumor copper levels are linked to the progression of cancer malignancy. Future work on this complex will be focus on *in-vivo* imaging acute liver conditions such as that found in Wilson's disease or change in copper levels in other diseases conditions.

In chapter 3, we reported a simple monophosphoamide derivative of GdDOTA that exhibits an optimized sigmoidal increase in relaxivity (r_1) with a decrease in pH. Although the relationship between relaxivity and concentration has been determined with great accuracy *in vitro*, the value of r_1 *in vivo* is less well-defined because of possible interactions between the agent and other extracellular components such as small molecule binding proteins. Also, the local concentration of an agent in tissue is uncertain given the changes in tissue distribution and possible different r_1 values in each compartment. After injection, the concentration of a small molecule contrast agent changes with time due to filtration of agent by the kidneys. Consequently, the actual tissue concentration of the agent at any point in time is uncertain. To solve this problem, one might add

some radioactive tracer to the agent such that the quantitative PET signal would provide a direct readout of concentration at any point in time. Therefore, the subsequent work of this pH responsive agent would be to develop a PET/MRI platform for imaging tissue pH using GdDOTA-1AmP. This bimodal agent would be able to map the tissue pH of kidneys in mice using combined MR T_1 -weighted imaging and PET to quantitatively determine the concentration of the agent as it is cleared via renal filtration.

BIOGRAPHICAL SKETCH

Namini N. Paranawithana was born on June 20, 1985 in Sri Lanka. After completing her higher secondary in Girl's High School, Kandy, she was admitted to one of the best colleges in Sri Lanka, Institute of Chemistry Ceylon, Colombo. She graduated with her Bachelor of Chemistry in 2010 with Honors. She next joined Veterinary Research Institute, University of Peradeniya, as a research assistant while working as a Program Director at FRIDSRO, Sri Lanka. In 2011 she joined Sam Houston State University and earned her master's in August 2013. During her master's she joined Dr. Donovan C. Haines team and participated in investigating dimerization of P450_{BM-3} enzyme. In August of 2013, she entered the PhD program in Chemistry at The University of Texas at Dallas and joined Dr. A. Dean Sherry's lab in November 2013 and chose to work to develop smart probes for magnetic resonance imaging.

CURRICULUM VITAE

Namini Nirodha Paranawithana

E-mail: namini.paranawithana@utdallas.edu

Education

- 2013-2018 Doctor of Philosophy in Chemistry, University of Texas at Dallas, Texas.
Dissertation Title: “Development of non-invasive responsive agents for magnetic resonance imaging”
Advisor: **Prof. A. Dean Sherry**
- 2011- 2013 Master of Science in Chemistry, Sam Houston State University, Texas.
Dissertation Title: “Developing tools for Probing P450 BM-3 Dimerization using synthetic biology and froster resonance energy transfer”
Advisor: **Dr. Donovan C. Haines**
- 2005-2008 Bachelor of Science in Chemistry, Institute of Chemistry Ceylon, Sri Lanka.
Dissertation Title: “Effect on feeding coconut oil and sesame oil at different dietary levels on the concentration of crude protein and total fat in goat milk.”
Advisors: **Dr. Anoja Wanigasekera, Prof. Subramaniam Sotheeswaran**

Professional Experience

- 2015-2018 **Graduate Research Assistant**—The University of Texas at Dallas, Texas.
- * Designed and completed multi-step synthesis of novel MRI contrast agents for in-vivo imaging of metal ions (Cu, Zn) and pH differences. Synthesized 8 novel compounds using standard organic synthesis techniques. One of which enhance contrast by 270-fold in presence of copper ions.
 - * Characterization of molecules using standard analytical and bioanalytical techniques. (HPLC, NMR, Column(Flash) Chromatography, Thin Layer Chromatography, UV absorbance Spectroscopy, Fluorescence Spectroscopy, Isothermal Titration Calorimetry, Relaxometry, XANES, EXAFS, Potentiometry, FHPLC, Ion-exchange chromatography, LC-MS, ICP-MS)
 - * Phantom Imaging and In-vivo Imaging of mice using developed contrast agents
 - * Spearheaded collaborations between 3 principal investigators and Macrocyclic company for physio-chemical characterization of molecules
 - * Supervised undergraduate students
 - * Lab safety management
 - * Presented work at local and international scientific meetings

- 2013-2015 **Graduate Teaching Assistant** - The University of Texas at Dallas, Texas.
- 2011-2013 **Graduate Teaching Assistant** -Sam Houston State University, Texas.
- * Lesson Planning and conduct the lab courses (Biochemistry, Organic Chemistry, General Chemistry I and II, Inorganic and Environmental Chemistry, Advanced Organic Synthesis).
 - * Tutoring, class room management, grading exams and lab reports
 - * Involved in the development of new course materials
 - * Research Focused on Probing P450 BM-3 Dimerization using standard synthetic biology techniques, biological assays, Primer designs, PCR, Bacterial culture and transformations and SDS-PAGE.
- 2009-2011 **Research Assistant** – Veterinary Research Institute, Sri Lanka.
- * Evaluation of Antibiotics in Animal feeds and poultry products using HPLC methods
 - * Analysis of diet and use of competitive exclusion agents on the incidence of sub clinical necrotic in broiler chicken using standard veterinary biochemical techniques (Animal Nutrition, Feed Formulation, Animal handling and Microbiology)
 - * Isolation of beta lactoglobulin to analyse effect of ginger and clove on total protein profile using biochemical analytical techniques (Kjeldahl Method, SDS-PAGE, and biochemical assays)

Publications and Presentations

ORAL PRESENTATIONS

1. Paranawithana, Namini N.; Martins, Andre F.; Zhao, Piyu; Kiefer, Garry; Sherry, A. D. 67th Southeast/71st Southwest Joint Regional Meeting of the American Chemical Society, Memphis, TN, USA, November 4-7 (2015), SERMACS-SWRM-885.
2. Paranawithana, Namini N.; Martins, Andre F.; Meloni, Gabriele; Sherry, Dean. 254th ACS National Meeting & Exposition, Washington, DC, USA, August 20-24, 2017 (2017), INOR-521.
3. Paranawithana, Namini N.; Martins, Andre F.; Zhao, Piyu; Sherry, Dean. 70th Southwest Regional Meeting of the American Chemical Society, Fort Worth, TX, United States, November 19-22 (2014), SWRM-283.
4. Paranawithana, Namini N.; Martins, Andre F.; Zhao, Piyu; Sherry, A. Dean. World Molecular Imaging Congress, Honolulu, Hawaii, United State, September 02-05 (2015).
5. Paranawithana, Namini N.; Martins, Andre F.; Zhao, Piyu; Kiefer, Garry; Sherry, A. D. 67th Southeast/71st Southwest Joint Regional Meeting of the American Chemical Society, Memphis, TN, USA, November 4-7 (2015), SERMACS-SWRM-885.
6. Paranawithana, Namini N.; Martins, Andre F.; Zhao, Piyu; Sherry, A. Dean. Metal in Medicine, Gordon Research Conference, United State, June 26- July 01 (2016).

7. Paranawithana, Namini N.; Martins, Andre F.; Meloni, Gabriele; Chirayil, Sara; Zhao, Piyu; Sherry, A. Dean. 253rd ACS National Meeting & Exposition, San Francisco, CA, United States, April 2-6 (2017), MEDI-87.
8. Paranawithana, Namini N.; Martins, Andre F.; Meloni, Gabriele; Chirayil, Sara; Zhao, Piyu; Sherry, A. Dean. World Molecular Imaging Congress, Philadelphia, New York, United State, September 13-16 (2017)
9. Jordan V.C.; Chirayil, S.; Martins, A.F.; Paranawithana, N.; Sherry, A.D., Imaging Glucose-stimulated Zinc secretion from prostrate and pancreas using a Mn(II) based Zn Sensor, Joint Annual Meeting ISMRM-ESMRMB, Paris, France, June 16-12 (2018), 3076
10. Martins, A.F.; Jordan V.C.; Chirayil, S.; Paranawithana, N.; Sherry, A.D., Low affinity zinc sensors for improved MRI detection of glucose-stimulated zinc(II) secretion from pancreatic beta-cells in vivo, Joint Annual Meeting ISMRM-ESMRMB, Paris, France, June 16-12 (2018), 4054

PUBLICATIONS

1. Martins, A.F.; Jordan, V.C.; Bochner, F.; Chirayil, S.; Paranawithana, N.; Zhang, S.; Zhao, P.; Neeman, M.; Sherry, A.D., Imaging beta-cell function in the mouse pancreases by use of a zinc ion-responsive MRI contrast agent enabled by a MR-compatible window, JACS, 2018 (November), In Press.
2. Wanigasekara W.A.A.P, Munasinghe M.N.D, Paranawithana N.N, Amarasekara M.P.N, Weihena S.J, Silva S.S.P, Jayasooriya L.J.P.A.P, Hiraga K.; Effect of feeding coconut oil at different dietary levels on the protein profile of goat milk, Proceedings- Peradeniya University Research Sessions, 2009, 14, 10-30.
3. Paranawithana, N.N.; Martins, A.F.; Jordan, V.C.; Chirayil, S.; Meloni, G.; Sherry, A.D., A responsive MRI contrast agent for detection of excess copper (II) in liver *in vivo*, JACS, 2018(November) (Submitted)
4. Paranawithana, N.N.; Martins, A.F.; Jurek, P.; Lopez, K.; Kiefer, G.; Sherry, A.D., A novel pH-sensitive MRI contrast agent based upon GdDOTA-monoamide methylene phosphonate, 2018 (October) (In preparation)

Awards and Affiliations

- * Robert A. Welch Research Fellowship – 2012 and 2013.
- * Special Graduate Scholarship Award, College of Arts and Sciences, Sam Houston State University, Texas – 2013.
- * Betty and Gifford Johnson Scholarship Award, Natural Science and Mathematics, University of Texas at Dallas, Texas -2016.
- * Member of American Chemical Society-2014-Present.
- * Sri Lankan Student Association at UTD - Assistant Treasurer, 2014 - 2016.